THE UNIVERSITY OF CHICAGO

A MEASUREMENT OF THE RATIO

$$R \equiv \sigma \cdot B(p\overline{p} \rightarrow W \rightarrow e\nu) \ / \ \sigma \cdot B(p\overline{p} \rightarrow Z^0 \rightarrow e^+e^-)$$

IN $p\overline{p}$ COLLISIONS AT $\sqrt{s} = 1800 \ GeV$

A DISSERTATION SUBMITTED TO

THE FACULTY OF THE DIVISION OF THE PHYSICAL SCIENCES

IN CANDIDACY FOR THE DEGREE OF

DOCTOR OF PHILOSOPHY

DEPARTMENT OF PHYSICS

BY

SACHA E. KOPP

CHICAGO, ILLINOIS

AUGUST 1994

Acknowledgments

One cannot imagine how true such a statement as "...this research would not have been possible without the valuable collaboration of many others...", *etc.*, is until one actually endeavors to finish one's own project. The physics result presented in this thesis is not so much a testament to the many lessons that I have learned in graduate school at the University of Chicago, but rather to the diligent, complex, and careful work of my many collaborators at the Collider Detector Facility at the Fermi National Accelerator Laboratory. Their planning and years of work have made CDF a premiere experiment in high energy physics research. I owe to them my eternal gratitude.

While the task is a daunting one, I would like to acknowledge a few people who made my graduate experience as rewarding as it has been. First, I would like to thank the committee members, Professors Jonathon Rosner, S. Courtenay Wright, Eugene Parker, and Leo P. Kadanoff, who oversaw my Ph.D. Qualifying Examination(s!) in 1991 and 1992. Taking that exam again forced me to finally understand that there is no electric field outside a grounded, conducting sphere. I would also like to thank Professor James Pilcher, who conducted the graduate experimental physics course at the University of Chicago in 1992, the best class I ever took. I would similarly like to thank Professor James Cronin, who showed me that one can extract a lot of physics from a ruler and a calculator. The many helpful comments and discussions with the members of my thesis committee, Professor Cronin, my advisor

Professor Henry Frisch, Professor Jeff Harvey, and Professor David Grier, have improved the quality of this work.

I am indebted to Harold Sanders and the EFI Electronics Development Group. Their expertise made the analog test equipment I was assigned to build a reality. Harold was also great for ideas on building a better amplifier for my stereo at home. I am deeply indebted to Dr. Greg Sullivan, my co-collaborator on this thesis project. Greg did many of the initial Monte Carlo studies and spent many hours checking the results. I am grateful to Professors Mel Shochet and Sarah Eno, and to Dr. Carla Grosso-Pilcher, who were always willing to think about difficulties I was having and spent a good deal of time thinking through technicalities of this project along with Greg and me.

Drs. Paul Derwent and Barry Wicklund patiently explained many of the things I did incorrectly in this work. Paul spent many hours describing tracking at CDF, and it was his thesis that provided the spring-board for this thesis. Barry, furthermore, is the guru of electron identification at CDF; many of the ideas employed in this thesis are really his.

I would not be complete in my acknowledgments without thanking my fellow graduate students at the University of Chicago. They, along with the faculty and post-docs, always provided stimulating discussion and a sense of community at the University. In particular, I would like to express my gratitude to Jim Romano, David Saltzberg, and Jinsong Wang. While I was off flunking the Candidacy Exam and crimping connectors on ribbon cables, these guys kept CDF running.

I leave mention of my thesis advisor, Professor Henry Frisch, last -- but only to emphasize my gratitude to him most. Henry's office door is always open, and this fact symbolizes his dedication to his students. From his desk chair, Henry could see through all the technicalities of work I was doing to ask the physics questions that always seemed to matter. I could not name all of the instances where he pulled my nose away from the grindstone far enough to show me I was polishing it off of my face. Anyway, to name them all would muddle the point. I only hope that I will take away the same sense to ask the

reasonable questions that he has. I am grateful for the many hours of attention he has given to this work and for his many creative ideas.

Henry created a real sense of cohesiveness and collaboration within our group at the University of Chicago. This is the best kind of atmosphere to work in, and made the vast empire of the CDF collaboration seem not so unruly to a new kid like me. Physics is only fun if you have great group of people with whom to bounce ideas back and forth; this kind of environment is what Henry developed for all of us. I will always be grateful for his good nature and his friendship.

Finally, I would like to express my love and gratitude to my family and friends who saw that I finished graduate school in good health and happiness. I would never have finished out these last four years without their constant devotion and support. To my father and mother, my mainstays in life. To my friend Simon, *mon frère cretenois*; and to Gretchen, *grosses bises et milles fois merci.*

Table of Contents

Acknowledgments ii
List of Tables viii
List of Illustrations x
Abstract xiii

Chapter

1. Introduction 1
- 1.1 Measurement of $\Gamma(W)$ from W and Z^0 Cross Sections 6
- 1.2 Measurement of $\Gamma(W)$ from the W Transverse Mass 7
- 1.3 Other Measurements of $\Gamma(W)$ 8
- 1.4 1992-1993 Run of CDF 9
- 1.5 Strategy of this Measurement 10
- 1.6 Outline of Thesis 12

2. Electron and Neutrino Identification 13
- 2.1 The CDF Detector 13
- 2.2 Electron Cluster Candidates 19
- 2.3 Fiducial Volume for Electrons 19
- 2.4 Central Electron Identification 21
- 2.5 Plug Electron Identification 32
- 2.6 Forward Electron Identification 32
- 2.7 Central Electron Trigger 36
- 2.8 Neutrino Identification 39

3. Inclusive Electron Sample 43

3.1 Central Electron Selection 44

3.2 Z^0 Sample Selection 46

3.3 W Sample Selection 49

3.4 Non-W/Z^0 Electron Sample Selection 49

4. Non-W/Z^0 Electron Sample 55

4.1 Number of Inclusive Electrons from QCD Jets 56

4.2 Conversion Electrons 60

4.3 b Electrons 67

4.4 Fake Electrons 72

5. W Candidate Sample 74

5.1 W Candidate Selection 74

5.2 Background from Hadron Jets 75

5.3 Cross-Check of Hadron Jet Background 81

5.4 Background from $Z^0 \rightarrow e^+e^-$ 87

5.5 Cross-Check of Background from $Z^0 \rightarrow e^+e^-$ 88

5.6 Background from $Z^0 \rightarrow \tau^+\tau^-$ 92

5.7 Background from $W \rightarrow \tau\nu$ 92

5.8 Background from Heavy Top Quark 93

5.9 Summary of W Signal, Backgrounds 93

6. Z^0 Candidate Sample 97

6.1 Z^0 Candidate Selection 97

6.2 Background from Hadron Jets 98

6.3 Background from $Z^0 \rightarrow \tau^+\tau^-$ 100

6.4 Background from Drell-Yan 100

6.5 Background from W + Jet Production 101

6.6 Summary of Z^0 Signal, Backgrounds 101

7. Acceptances 103

7.1 Description of the Monte Carlo 103

7.2 Systematic Uncertainties in A_W, A_Z 104

7.3 Effects of Radiative Corrections 108

7.4 Comparison with an $O(\alpha_s)$ Monte Carlo 108
7.5 Summary of Acceptance Results 110

8. Efficiencies 111
8.1 Tight Central Identification Efficiency c_1 112
8.2 Loose Central Identification Efficiency c_2 113
8.3 Loose Plug Identification Efficiency p 114
8.4 Loose Forward Identification Efficiency f 114
8.5 Central Electron Trigger Efficiency ε_T 115
8.6 Final Selection Efficiencies ε_W and ε_Z 116

9. Conclusions 117
9.1 Summary of Results for R 117
9.2 Future Prospects for $BR(W\rightarrow e\nu)$ and $\Gamma(W)$ 119

Appendix

A. A Direct Measurement of $\Gamma(W)$ 125
A.1 Selection of Dataset for Width Measurement 125
A.2 Backgrounds 133
A.3 Kinematic Cuts to Reduce W Width Uncertainties 137
A.4 Determination of the W Width 143

B. A Note on Calculating the b Electron Fraction 154

References 156

List of Tables

1.1: Decay Modes and Relative Decay Rates of W^+ 2
1.2: Corrections to $\Gamma(W)$ from $\delta_W(0)$ 5
1.1: Corrections to $\Gamma(W)$ from δ_μ 5
1.4: Previous Measurements of $\Gamma(W)$ obtained from R 8
2.1: Description of the CDF Calorimetry Subsystems 16
2.2: Description of Shower Max and Pre-Shower Detectors 16
2.3: Description of Charged Particle Tracking Chambers 18
3.1: Inclusive Central Electron Cuts 44
3.2: Z^0 Selection Cuts 46
3.3: Z^0 Yield in Different Detector Regions 48
4.1: Conversion Pair Control Samples 63
7.1: Systematics from Parton Distribution Functions 105
7.2: Systematics from M_W, $sin^2\theta_W$ 105
7.3: Systematics from Boson P_T Distribution 106
7.4: Systematics from Underlying Event Model 107
7.5: Systematics from Energy Scale 108
7.6: Systematics from Higher Order Diagrams 109
8.1: The Efficiency c_1 for Central Electrons 113
8.2: The Efficiency c_2 for Central Electrons 113
8.3: The Efficiency p for Plug Electrons 114
8.4: The Efficiency f for Forward Electrons 115
8.5: The Efficiency ε_T of the Central Electron Trigger 115
9.1: R with 20 GeV cuts on $\not{E}_T$ and Electron E_T 120

9.2: R with 25 GeV cuts on $\not{E}_T$ and Electron E_T 121
9.3: Present and Future Uncertainties in $BR(W \rightarrow \quad e\nu)$ 123
A.1: Selection Criteria for W Dataset 126
A.2: Selection Criteria to Remove Z^0 Decays 129
A.3: Cross-Check with W Cross Section 143
A.4: Present and Future Uncertainties in $\Gamma(W)$ 152

List of Illustrations

1.1: Feynman Graphs of Processes that lead to $\Gamma(W)$ Correction 4

1.2: Side View of CDF Detector and Z^0 Candidate Event 11

1.3: Distribution in η of Electrons from $Z^0 \rightarrow e^+e^-$ Decays 11

2.1: View of One Half of the CDF Detector 14

2.2: View of One Wedge of the Central Calorimeter 17

2.3: Map in η-ϕ Space of Fiducial Volume for Electrons 20

2.4: Central Identification Variables for Inclusive Central Electrons and Electrons from W Decays 22

2.5: Strip Chamber Pulse Height for Electrons and Hadrons 23

2.6: CPR Pulse Height for Electrons and Hadrons 23

2.7: Impact parameter for Electrons from $Z^0 \rightarrow e^+e^-$ Decays 27

2.8: Size of Beam Spot in x and y Views 27

2.9: (a): D/σ for Electrons from $Z^0 \rightarrow e^+e^-$ Decays (b): Invariant Mass for Z^0's with $D/\sigma > 2$ 28

2.10: Z_0 of event vertex 30

2.11: Δz between Electron Tracks from $Z^0 \rightarrow e^+e^-$ Decays 30

2.12: Z^0 Invariant Mass in the Central, Plug, and Forward Regions 33

2.13: Plug Electron Identification Variables 34

2.14: Forward Electron Identification Variables 35

2.15: Trigger Efficiency in Levels 1, 2, and 3 *vs.* E_T 37

2.16: Efficiency of the Trigger *vs.* η 38

2.17: $\not{E}_x$ and $\not{E}_y$ for Minimum Bias Trigger Events 40

2.18: Fitted $\sigma(\not{E}_x)$ *vs* $\Sigma(E_T)$ in Minimum Bias Trigger Events 41

2.19: $\not{E}_T / [\Sigma(E_T)]^{1/2}$ in Minimum Bias Trigger Events and $W \rightarrow e\nu$ Events 42

3.1: E_T of Inclusive Electrons, Isolated Inclusive Electrons, and Electrons from $W \rightarrow e\nu$ Decays 45

3.2: Invariant Mass Spectrum of e^+e^- with No Cuts on the Second Electron 47

3.3: Invariant Mass Spectrum of e^+e^- with All Cuts on the Second Electron 47

3.4: Distribution in η of 2nd Electrons from $Z^0 \rightarrow e^+e^-$ Decays 48

3.5: Isolation of the Electron *vs.* $\not{E}_T$ 51

3.6: $\not{E}_T$ Spectrum of Isolated Inclusive Electrons 52

3.7: Transverse Mass of Inclusive Electrons with $\not{E}_T > 20$ *GeV* 53

3.8: Distribution in η of Electrons from $W \rightarrow e\nu$ Decays 54

4.1 (a): $\Delta\phi$ between $\not{E}_T$ and Largest Jet 57
(b): $\cos(\Delta\phi)$ between Electron and Largest Jet

4.2: $\not{E}_T$ Spectrum of Non-isolated Inclusive Electrons 58

4.3: E_T Spectrum of Inclusive Electrons after W/Z^0 Removal 59

4.4: $\delta(r\text{-}\phi)$ and $\delta(\cot\theta)$ for Track Pairs 61

4.5: Radius of Origin Point of Photon Conversions 62

4.6: CES Pulse Height for Partner Tracks from Conversions 64

4.7: P_T of Partner Track in Conversion Electron Pairs 64

4.8: $\delta(r\text{-}\phi)$ and $\delta(\cot\theta)$ for Conversions 66

4.9: Jet Probability for Jets in Electron Events with $\not{E}_T < 10$ *GeV* 69

4.10: D/σ for b Electrons 70

4.11: D/σ for Conversion Electrons 70

4.12: D/σ for all Electrons in the Non-W/Z^0 Sample 71

4.13: CPR Charge for all Electrons with $\not{E}_T < 10$ *GeV* 73

5.1: Mean Electron *Iso vs.* Jet E_T in $\not{E}_T < 10$ *GeV* Region 77

5.2: *Iso* of Control Samples and $\not{E}_T > 20$ *GeV* Sample 78

5.3: Mean Electron *Iso vs.* $\not{E}_T$ 80

5.4: $\not{E}_T$ of Electrons with *Iso* > 0.3, $\not{E}_T > 20$ *GeV* 80

5.5: $\not{E}_T$ of Tagged Conversions with $\not{E}_T > 20$ *GeV* 83

5.6 (a): D/σ of $\not{E}_T > 20$ *GeV* Sample 85
(b): $\not{E}_T$ of $D/\sigma > 2, \not{E}_T > 20$ *GeV* Sample

5.7: CPR Shape of $\not{E}_T > 20$ *GeV* Electrons 86

5.8: $M_{(e+trk)}$, with and without Cuts on 2nd Track 89

5.9: Z^0 Selection Variables for Electron + Stiff Track Selection 89

5.10 Variables for $Z^0 \rightarrow e^+e^-$ Decays when Second Electron is Unobserved in the Calorimeters (a): Local Calorimeter Position of Stiff Track (b): $\Delta\phi$ between 2nd Track and the $\not{E}_T$ in the Event 90
5.11: $M_{(e+trk)}$ Comparison between Data and ISAJET Monte Carlo 91
5.12: E_T of $W \rightarrow e\nu$ Decays 94
5.13: $\not{E}_T$ of $W \rightarrow e\nu$ Decays 95
5.14: Transverse Mass of $W \rightarrow e\nu$ Decays 96
6.1: $M_{(ee)}$ *vs. Iso* of 2nd leg 99
6.2: Invariant Mass of $Z^0 \rightarrow e^+e^-$ Decays 102
9.1: $BR(W \rightarrow e\nu)^{-1}$ *vs.* M_{top} 122
A.1: Biases of Electron Selection Cuts *vs.* E_T 127
A.2: Transverse Mass of W Candidates 128
A.3: Tracking Variables Used to Remove Z^0 Decays 130
A.4: Calorimetry Variables Used to Remove Z^0 Decays 131
A.5: Variables Used to Remove Dijets 132
A.6: Transverse Mass of Background from Weak Boson Decays 134
A.7: Transverse Mass of Expected *QCD* Dijet Background 136
A.8: Expected Variation of Transverse Mass Distribution with no $P_T(W)$ Applied 138
A.9: Transverse Mass Distribution Before $P_T(W)$ Cut 139
A.10: Expected Variation of Transverse Mass Distribution with a $P_T(W) < 20$ *GeV/c* Cut Applied 140
A.11: W Transverse Momentum Distribution 141
A.12: Transverse Mass Distribution After $P_T(W) < 20$ *GeV/c* Cut 142
A.13: $\ln\mathcal{L}$ of Data Fit to Monte Carlo *vs.* $\Gamma(W)$ 145
A.14: $\Gamma(W)$ Results of Many Monte Carlo "Experiments" 146
A.15: σ_{perp} and σ_{par} in Z^0 Data and Monte Carlo 147
A.16: The $\not{E}_T$ Component in the x Direction from Minimum Bias Data 149
A.17: Transverse Mass Distribution After $P_T(W) < 10$ *GeV/c* Cut 151

Abstract

We present an analysis of data from $p\overline{p}$ collisions at a center of mass energy of $\sqrt{s} = 1800\ GeV$. A measurement is made of the ratio $R \equiv \sigma \cdot B(p\overline{p} \rightarrow W \rightarrow e\nu) \ / \ \sigma \cdot B(p\overline{p} \rightarrow Z^0 \rightarrow ee)$. The data represent 22.8 pb^{-1} collected by the Collider Detector at Fermilab (CDF) during the 1992-1993 collider run of the Fermilab Tevatron. We find $R = 10.90 \pm 0.32\,(stat.) \pm 0.29\,(sys.)$, and from this value we extract the ratio of W and Z^0 branching ratios, $B(W \rightarrow e\nu)/B(Z^0 \rightarrow e^+e^-)$. Using the LEP measurements of $\Gamma(Z^0)$ and $\Gamma(Z^0 \rightarrow e^+e^-)$, we obtain a measurement of the $W \rightarrow e\nu$ branching ratio $\Gamma(W \rightarrow e\nu)/\Gamma(W) = 0.1094 \pm 0.0033(stat.) \pm 0.0031(sys.)$. From this branching ratio we set a limit on the top quark mass of $m_{top} > 62\ GeV/c^2$ at the 95% confidence level. In contrast to direct searches for the top quark, this limit makes no assumptions about the allowed decay modes of the top quark. In addition, we use a calculation of the leptonic width $\Gamma(W \rightarrow e\nu)$ to obtain a value for the W total decay width: $\Gamma(W) = 2.064 \pm 0.0060(stat.) \pm 0.0059(sys.)\ GeV$. Finally, we present a direct measurement of the W width from the tail of the W transverse mass spectrum: $\Gamma(W) = 2.04 \pm 0.28(stat.) \pm 0.16(sys.)\ GeV$.

Chapter 1

Introduction

It was a series of experiments on X-ray radiation by Arthur Holly Compton[1] which demonstrated that the scattering of radiant energy, which was formerly described by waves or fields, could also be viewed as the scattering of pointlike particles. These observations confirmed the corpuscle theory of light proposed by Einstein to explain the photoelectric effect.[2] Today the corpuscle, or quantum, interpretation has expanded to our understanding of not just radiant energy but all the known forces. In 1933 Fermi[3] proposed a new ("weak") force to explain nuclear β-decay, and in 1938 Klein[4] proposed the existence of a massive force carrier, the W, to explain the weak force's short range. The massive $W^{\pm}$ and Z^0 particles are the intermediate vector bosons which carry this weak force. Together with the massless photon (γ), they compose the bosonic fields of the unified Electroweak Theory proposed by Weinberg,[5] Salam,[6] and Glashow.[7]

Present experimental measurements of Electroweak parameters such as the masses and decay widths of the vector bosons are precise enough to provide tests of QCD and of the Standard Model beyond just the leading order. Studies of the Z^0 resonance in e^+e^- collisions at the LEP[8] and SLD[9] experiments have determined the mass and width of the Z^0, as well as the weak mixing angle, to a few parts in ten thousand. These precise measurements not only test the Electroweak theory, but also provide possible windows to sectors of the theory at mass scales higher than those directly observable at current

accelerator energies. These sectors enter into the Electroweak observables through radiative corrections.

While the parameters of the Z^0 boson have been well-studied, similarly precise studies at high Q^2 of the charged current carrier, the W, have been limited. Because of the limited energies available at e^+e^- colliders, measurements pertaining to the W have been the purview of $p\overline{p}$ colliders. The W and Z^0 are predominantly produced in hadron-hadron collisions via the Drell-Yan[10] mechanism: that is, a quark in one hadron annihilates with an antiquark in the other hadron to produce a vector boson. Measurements of the W boson mass, for example, by the CDF[11] and UA2[12] collaborations have yielded $M_W = 80.14 \pm 0.27\ GeV/c^2$.

This thesis presents two measurements of the decay width, $\Gamma(W)$, of the W boson. The expected decay modes of the W^+ are listed in Table 1.1 (the W^- decays to charged conjugate pairs), along with the expected decay rates to lowest order in the Electroweak theory and to order $O(\alpha_s)$ in QCD.[13] The partial width into fermion pairs is calculated as in muon decay: $\Gamma_0(W \to f\overline{f}') = |V_{ff'}|^2 N_c (G_F/\sqrt{2})(M_W^3/6\pi)$, where $V_{ff'}$ is the Kobayashi-Maskawa matrix element for two quarks and is 1.0 for leptons, and $N_c = 3$ for quarks and $N_c = 1$ for leptons. Partial widths into quark pairs receive an additional *QCD K*-factor correction at $O(\alpha_s)$.

Table 1.1: Known Decay Modes of the W^+, and Relative Decay Rate Relative to $e\nu$ to lowest order in the SM and $O(\alpha_s)$ in QCD.[13]

Decay mode of W^+	Partial Decay Width in Units of $\Gamma(W \to e\nu)$
$e^+\nu$	1.0
$\mu^+\nu$	1.0
$\tau^+\nu$	1.0
$u\overline{d}$	$3\,(1+\alpha_s/\pi)\cos^2\theta_c$
$u\overline{s}$	$3\,(1+\alpha_s/\pi)\sin^2\theta_c$
$c\overline{s}$	$3\,(1+\alpha_s/\pi)\cos^2\theta_c$
$c\overline{d}$	$3\,(1+\alpha_s/\pi)\sin^2\theta_c$

If the top quark is lighter than the W, specifically if $m_t < M_W - m_b$, then the decay $W \to tb$ is allowed, while for $m_t > M_W - m_b$ the decay $W \to tb$ is forbidden by energy conservation. A light top quark would add one more partial width $\approx$ 3 times greater than the leptonic width $\Gamma(W \to \ell\nu)$ because of the color factor of 3 for quarks. The value for the width would then be $\Gamma_0(W) \approx 2.767$ GeV and the leptonic branching ratio would be $\Gamma_0(W \to e\nu)/\Gamma_0(W) \approx 1/12$ instead of the value $\Gamma_0(W \to e\nu)/\Gamma_0(W) \approx 1/9$ when the top is heavy. Ignoring vertex corrections and assuming a heavy top, Rosner *et. al.*[14] have calculated (to next-to-leading order in QCD) values of:

$$\Gamma_0(W) = \left[3 + 6(1 + \alpha_s(M_W)/\pi\right] \cdot \Gamma_0(W \to \ell\nu) = 2.075 \pm 0.021 \ GeV,$$

$$\Gamma_0(W \to \ell\nu)/\Gamma_0(W) = \left[3 + 6(1 + \alpha_s(M_W)/\pi\right]^{-1} = 0.1084 \pm 0.0002.$$

Within the Standard Model the W width receives vertex and Bremsstrahlung corrections that total approximately[15] to -0.4%, or 10 MeV (for $m_{top} = 140$ GeV/c^2 and $m_{Higgs} = 100$ GeV/c^2), as summarized in Tables 1.2 and 1.3. The corrections can be summarized in the equation:

$$\Gamma(W \to f\bar{f}')_{SM} = \Gamma_0(W \to f\bar{f}') \cdot \left[1 + \delta_V + \delta_W(0) + \delta_\mu\right].$$

where $\delta_W(0)$ is the correction to the width from loops involving Z^0's, top quarks, or Standard Model Higgs at the W-fermion vertex, δ_V describes boson self-energies, and δ_μ corrects for vertex and box corrections specific to muon decay. The latter correction is made necessary when the measured values for M_W and G_F (the latter from muon decay) are used to parameterize the W width.[16] Examples of the loops to which the W is sensitive are shown in Figure 1.1. Note that, because the corrections are nearly identical for leptons and quarks, these corrections affect only the width and not the branching ratio:

$$\Gamma(W)_{SM} = 0.996 \times \Gamma_0(W) = 2.067 \pm 0.021 \ GeV,$$

$$\Gamma_{SM}(W \to \ell\nu)/\Gamma_{SM}(W) = \Gamma_0(W \to \ell\nu)/\Gamma_0(W) = 0.1084 \pm 0.0002.$$

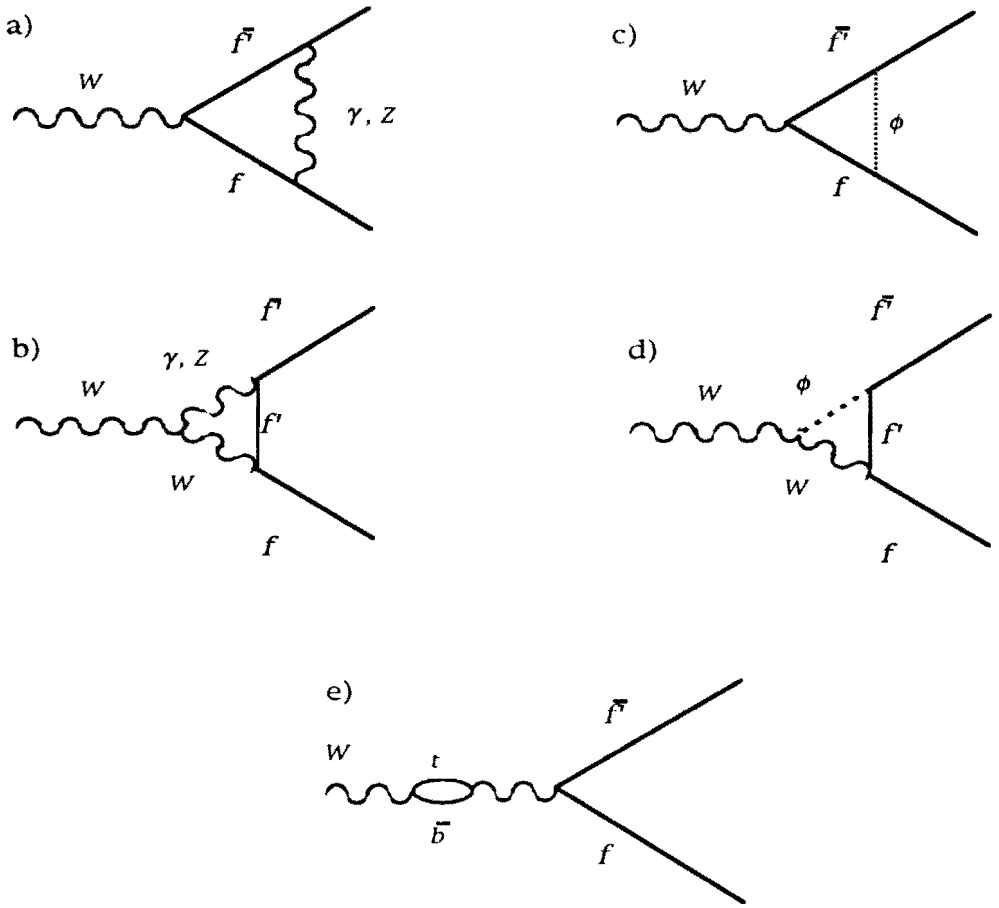

Fig. 1.1: Five Feynman diagrams contributing vertex corrections to the lowest order partial width $\Gamma(W \to f\bar{f}')$: a) and b) exchange of a virtual neutral vector boson, γ or Z^0; c) and d) exchange of a virtual neutral scalar boson, ϕ, such as Standard Model Higgs; e) loops of virtual $t\bar{b}$ pairs. While the effect of e) is partially absorbed into the W mass, these loops affect the propagator of real Ws, an effect not accounted for when using the value of G_F measured from muon decay.

A direct measurement of the W width is sensitive both to the corrections described above and to new decay channels available to the W that are not listed in Table 1.1. The loop corrections from a Standard Model Higgs causes $\Gamma(W)$ to change by approximately 1% as the Higgs mass varies from 50 GeV/c^2 to 1000 GeV/c^2, while the correction from $t\bar{b}$ loops changes $\Gamma(W)$ by approximately 4% as the top quark mass varies from 80 GeV/c^2 to 200 GeV/c^2.[15] Thus, in addition to testing the Standard Model at the next level in perturbation theory, a measurement of the W width with a precision of 1% or better would begin to constrain the allowed values of these particles' masses through the radiative corrections.

Table 1.2: Finite Parts of Contributions[14] to $\delta_w(0)$

Contribution	Value (%)
Light Fermions	0.80
$t\bar{b}$ loops	-0.04[a)]
Photon - W	-0.27
Z^0 loops	0.14
Standard Model Higgs	-0.006[b)]
Total	0.62

a) For $m_t = 140\ GeV/c^2$. b) For $M_H = 100\ GeV/c^2$.

Table 1.3: Finite Parts of Contributions[14] to δ_v and δ_μ

Contribution	Value (%)	
	Leptons	Quarks
Wave Function	-0.03	0.07
Vertices	-0.24	-0.61
Bremsstrahlung	-0.02	0.19
δ_μ	-0.68	-0.68
Subtotal	-0.97	-1.03
Total[c)]	-0.35	-0.41

c) Including the contributions of Table 1.2.

The W width could also be altered if additional decay modes other than those listed in Table 1.1 were available to the W. In particular, if the W could decay to a light ($m_t < M_W - m_b$) top quark, this decay would be signaled by a component to the W width in addition to that accounted for in the Standard

Model calculation. While direct searches[17] have set limits of $m_t > 131$ GeV/c^2 at the 95% confidence level, these limits assume that the top always decays via the reaction $t \rightarrow Wb$. If a charged Higgs exists, then these assumptions may no longer be valid and the decay $W \rightarrow tb \rightarrow Hbb$ could be missed by direct searches for $t \rightarrow Wb$.[18] The measurement of the W total decay width, then, is a sensitive search for a light top quark that is independent of assumptions regarding its allowed decays.

1.1 Measurement of $\Gamma(W)$ from W and Z^0 Cross Sections

The W width may be extracted from a measurement of the ratio, R, of the cross sections times branching ratios into electrons of the W and Z^0, $\sigma \cdot B(p\overline{p} \rightarrow W \rightarrow e\nu)$ and $\sigma \cdot B(p\overline{p} \rightarrow Z^0 \rightarrow ee)$, in proton-antiproton collisions.[19] Theoretically, R may be expressed as:

$$R \equiv \frac{\sigma \cdot B(p\overline{p} \rightarrow W \rightarrow e\nu)}{\sigma \cdot B(p\overline{p} \rightarrow Z^0 \rightarrow ee)} = \frac{\sigma(\overline{p}p \rightarrow W)}{\sigma(p\overline{p} \rightarrow Z^0)} \frac{\Gamma(W \rightarrow e\nu)}{\Gamma(Z^0 \rightarrow ee)} \frac{\Gamma(Z^0)}{\Gamma(W)}$$

On the right hand side, the ratio $\sigma(\overline{p}p \rightarrow W) / \sigma(p\overline{p} \rightarrow Z^0)$ of the production cross sections may be calculated from the boson couplings and knowledge of the proton structure. The Z^0 total width, $\Gamma(Z^0)$, and the leptonic partial width, $\Gamma(Z^0 \rightarrow e^+e^-)$, are well-measured by the LEP experiments.[20] Thus, a measurement of R yields a precise measurement of the W leptonic branching ratio $\Gamma(W \rightarrow e\nu)/\Gamma(W)$. If one then uses a calculation for the leptonic width $\Gamma(W \rightarrow e\nu)$ and divides by the measured branching ratio, a value is extracted for the total decay width, $\Gamma(W)$, of the W boson. Note, however, that the W width extracted from this measurement is not sensitive to vertex corrections, since it is normalized to the calculated $\Gamma(W \rightarrow e\nu)$, which does not include these effects. Only a direct measurement of $\Gamma(W)$, such as the one described in Section 1.2, is sensitive to these effects.

1.2 Measurement of $\Gamma(W)$ from the W Transverse Mass

W bosons are produced in $p\overline{p}$ collisions according to a relativistic Breit-Wigner distribution, convoluted with the parton distribution functions, which means that the invariant mass distribution could, in principle, be used to obtain a direct measurement of the Breit-Wigner width, $\Gamma(W)$. However, it is not possible in $p\overline{p}$ collisions to reconstruct the invariant mass of the W, since the neutrino momentum is inferred from momentum conservation and the longitudinal momentum of the initial parton-parton system that produced the W is unknown.

The W transverse mass, M_T, defined as

$$M_T^2 \equiv (|\boldsymbol{p}_{eT}| + |\boldsymbol{p}_{\nu T}|)^2 - (\boldsymbol{p}_{eT} + \boldsymbol{p}_{\nu T})^2,$$

where $\boldsymbol{p}_{eT}$ and $\boldsymbol{p}_{\nu T}$ are the electron and neutrino momenta in the plane transverse to the p and $\overline{p}$ beam directions, is used instead of the invariant mass. This variable is invariant to longitudinal boosts, and it is also invariant to first order in β to boosts in the transverse plane, where β is the W velocity in the transverse plane.[21]

If one had a perfect calorimeter and the W had zero natural width, then the transverse mass distribution would diverge at the W mass, M_W, and the relation $0 < M_T < M_W$ would hold. Calorimeter resolutions and the finite width of the W, however, smear the divergence at the W mass and cause some events to populate the region $M_T > M_W$. In addition, the P_T spectrum of the W enters into the M_T shape at second order. If the resolutions and P_T shape are understood, however, the population of events with $M_T > M_W$ can be used to provide a direct measurement of $\Gamma(W)$. This direct measurement complements the indirect value from the W and Z^0 cross sections because it has entirely different systematic uncertainties and because it is free of the theoretical assumptions regarding the W coupling to fermions, and hence may be used to observe loop effects. This method will eventually provide the best $\Gamma(W)$ measurement.

1.3 Other Measurements of $\Gamma(W)$

To this date, the most precise measurements that have been made of the W width have been extractions from the ratio R. Direct evidence for W production and Z^0 production were first obtained by the UA1 and UA2 experiments[22] in $p\overline{p}$ collisions at $\sqrt{s} = 0.56$ TeV at the CERN Sp$\overline{p}$S collider. Later, at $\sqrt{s} = 0.63$ TeV, these collaborations obtained the first estimate of the production cross sections times branching ratios into electrons, muons, and taus.[23] A summary of the values for the W width obtained from measurements of R is given in Table 1.4. In Table 1.4, mode = "e" or "μ" refers to a measurement of $\sigma \cdot B(p\overline{p} \to W \to e\nu)$ and $\sigma \cdot B(p\overline{p} \to Z^0 \to e^+e^-)$ or of $\sigma \cdot B(p\overline{p} \to W \to \mu\nu)$ and $\sigma \cdot B(p\overline{p} \to Z^0 \to \mu^+\mu^-)$.

Table 1.4: Previous Measurements of $\Gamma(W)$ Obtained from Measurements of R.

Experiment	Mode	$\sqrt{s}$ (TeV)	$\Gamma(W)$ (GeV)
CDF[24]	e	1.8	2.14 ± 0.20
CDF[25]	μ	1.8	2.21 ± 0.27
UA1[26]	μ	0.63	2.19 ± 0.30
UA2[27]	e	0.63	2.10 ± 0.16
DØ[28]	e	1.8	2.05 ± 0.16
DØ[28]	μ	1.8	2.20 ± 0.58

The best previous measurement of the W width has an error of 7.6%. The combination of all published measurements yields a value for the W total decay width, $\Gamma(W) = 2.12 \pm 0.11$ GeV, an accuracy of 5.2%.

The W width will also be determined by the LEP-200 experiments at center of mass energy near $\sqrt{s} = 2M_W$ from an endpoint analysis of the W daughter lepton energy spectrum. This measurement of $\Gamma(W)$ is a direct one, in contrast to the extractions from the R measurements, and the LEP200 experiments anticipate an accuracy on $\Gamma(W)$ of 200 MeV, or 10%.[29]

This thesis presents a value for the W width and branching ratio extracted from R with a precision of 4.1%, or 85 MeV. We present as well a direct measurement of $\Gamma(W)$ from the transverse mass shape which has an accuracy of 16%, or 340 MeV. The measurement of $\Gamma(W)$ from the ratio of cross sections is the most precise method currently available. With 1 fb^{-1} of data (a factor of 50 more than available now), the transverse mass method will yield the most precise method and one that is most free of theoretical assumption.

1.4 1992-1993 Run of CDF

The data presented in this thesis were collected by the Collider Detector at Fermilab observing $p\bar{p}$ collisions at the Fermilab Tevatron at a center of mass energy of $\sqrt{s}$ = 1.8 TeV. During the 1992-1993 collider run, the Fermilab Tevatron delivered a total integrated luminosity of $\int Ldt$ = 30.3 pb^{-1}, with typical instantaneous luminosities of 5.0 x 10^{30} $cm^{-2}sec^{-1}$ and a peak instantaneous luminosity of 9.7 x 10^{30} $cm^{-2}sec^{-1}$. The Collider Detector at Fermilab wrote 22.8 pb^{-1} of data to tape, with the 30% loss dominated by operational problems, but also coming from trigger and data acquisition dead time. This compares to 4.4 pb^{-1} of data collected in CDF's previous 1988-1989 run, which was only 50% efficient for writing data to tape. Approximately 1.1 pb^{-1} of this year's data was discarded after the fact because of hardware difficulties during data taking. In the 21.7 pb^{-1} of data remaining, approximately 20000 $W \rightarrow e\nu$ and 1600 $Z^0 \rightarrow e^+e^-$ decays were observed from all triggers, as were 7000 $W \rightarrow \mu\nu$ and 600 $Z^0 \rightarrow \mu^+\mu^-$ decays.

1.5 Strategy of This Measurement

The signature of high-P_T electrons from W and Z^0 decay is quite distinctive in the environment of hadron collisions. As such, the decay of W and Z^0 bosons into electrons provides a clean experimental measurement of their production. Experimentally, the cross sections times branching ratios are found from:

$$\sigma \cdot B(p\overline{p} \rightarrow W \rightarrow e\nu) = \frac{N_W^{Candidates} - N_W^{Background}}{A_W \varepsilon_W \int L dt}$$

$$\sigma \cdot B(p\overline{p} \rightarrow Z^0 \rightarrow e^+e^-) = \frac{N_Z^{Candidates} - N_Z^{Background}}{A_Z \varepsilon_Z \int L dt}$$

where $N_W^{Candidates}$ and $N_Z^{Candidates}$ are the number of W and Z^0 candidates observed; A_W and A_Z are the "acceptance" for the W and Z^0 decays (which includes the efficiency for the kinematic cuts on the leptons and the geometric acceptance of the detector); ε_W and ε_Z are the efficiency for the W and Z^0 to pass the lepton identification criteria, and $\int \mathcal{L} dt$ is the integrated luminosity of the experiment. Measuring the ratio of the cross sections allows some of the quantities (as well as their errors) on the right hand sides to cancel.

The strategy of this cross section measurement will be as follows: the CDF detector (shown in Figure 1.2) is a cylindrical detector with calorimetry and magnetic tracking analysis in the central barrel region, and only calorimetry in the end-cap regions. Electron identification is more difficult in these regions without the tracking. Because of this limitation, our method will be to select decays of the W and Z^0 where at least one electron falls into the central region.

The number of Z^0's limits the statistical accuracy of the R measurement of $\Gamma(W)$, and this tactic of requiring a common central electron to both W and Z^0 decays decreases the available Z^0 statistics even further. From a simple

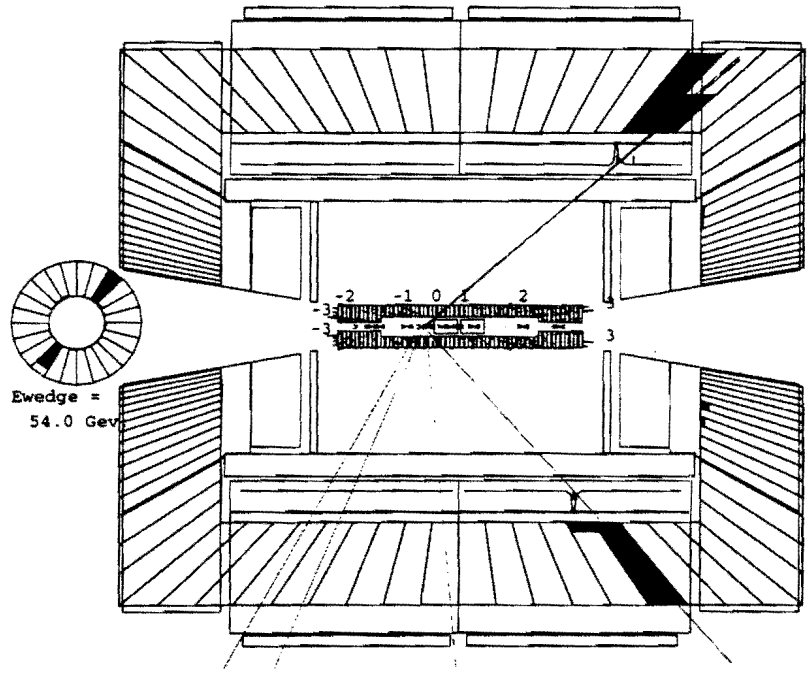

Fig. 1.2: Side view of CDF Detector and $Z^0 \rightarrow e^+e^-$ event in which both electrons go into the central detector region.

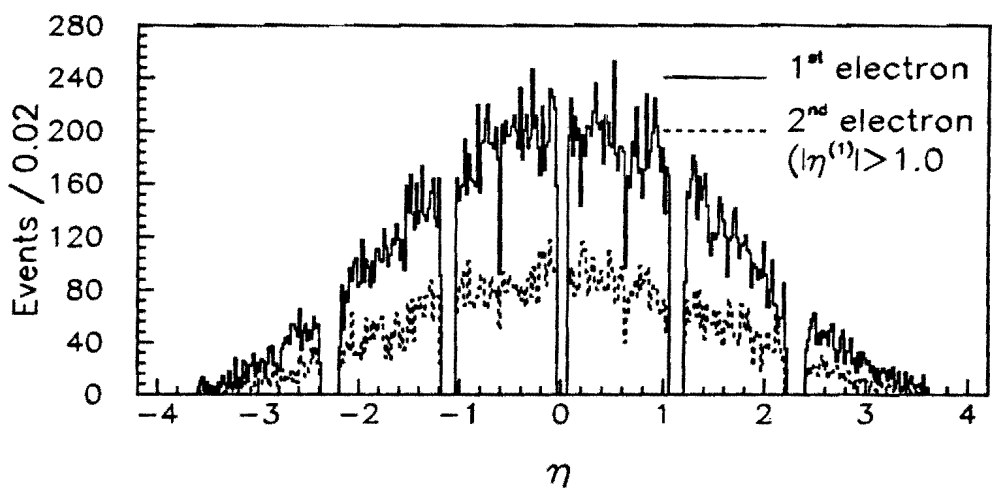

Fig. 1.3: The distribution in η of electrons in $Z^0 \rightarrow e^+e^-$ decays from the Monte Carlo described in Chapter 7. The "first" electron is required to pass a kinematic cut of $P_T > 20$ GeV. The distribution of the "second" electron is shown when the first electron falls in the region $|\eta| > 1.0$.

Monte Carlo (described in Chapter 7), we learn that requiring one electron in the central region is approximately 80% efficient for Z^0's (see Figure 1.3). This requirement is only $\approx$ 60% efficient for W's, but the W's do not statistically limit the overall measurement. Requiring a common central electron for both W's and Z^0's will increase the statistical error on the measurement by approximately 0.3%.

This method of requiring one common central electron, however, decreases the systematic error in the measurement. The selection criteria in requiring a central electron (which appear in the factors ε_W and ε_Z) will almost completely cancel in the ratio of cross sections because they are common to W's and Z^0's. The systematic error in the ratio of acceptances is smaller than for the individual acceptances when a common central electron is required. Furthermore, with the magnetic analysis in the barrel region of the detector, systematic errors from W and Z^0 backgrounds are much smaller in the barrel than in the end-cap regions. The smaller uncertainties in the backgrounds offset the expected 0.3% increase in statistical error from requiring the common central electron.

1.6 Outline of Thesis

The thesis will proceed as follows: Chapter 2 describes electron identification in the CDF detector. Chapter 3 describes the selection of the inclusive electron sample and the separation of this sample into W and Z^0 samples and a non-W/Z^0 sample of electrons from hadron jets. Chapter 4 describes the physics sources of high-P_T electrons in the non-W/Z^0 sample. This description is used in Chapter 5, where we discuss the make-up of the W sample and estimate the non-W backgrounds. Chapter 6 discusses the Z^0 candidate sample, and the estimation of its non-Z^0 backgrounds. Chapter 7 describes the Monte Carlo used to determine the acceptances A_W and A_Z. Chapter 8 describes the the efficiencies ε_W and ε_Z. Chapter 9 summarizes the R measurement of $\Gamma(W)$. Appendix A describes the alternative method of measuring $\Gamma(W)$ directly from the transverse mass distribution of W's.

Chapter 2

Electron and Neutrino Identification

The 1992-1993 data set collected by the Collider Detector at Fermilab (CDF) represents its third major physics run. Many previous publications[30] give detailed descriptions of the various components of the detector. In this Chapter, we summarize briefly the physical characteristics of those detector components relevant for electron and neutrino identification and describe their performance during the 1992-1993 run.

2.1 The CDF Detector

CDF is a cylindrical detector with a central, barrel region, two end-cap (plug) regions closing the barrel, and two far-forward detector regions. Figure 2.1 shows one half of the CDF detector. It features electromagnetic (EM) and hadronic (Had) shower counters arranged in projective tower geometry, as well as charged particle tracking chambers. The tracking chambers are immersed in a 1.4 T magnetic field oriented along the proton beam direction provided by a 3 m diameter, 5 m long superconducting solenoidal magnet coil. Although not used in this analysis, drift chambers outside the hadron calorimeters for muon detection cover the region $|\eta| < 1.0$.[31]

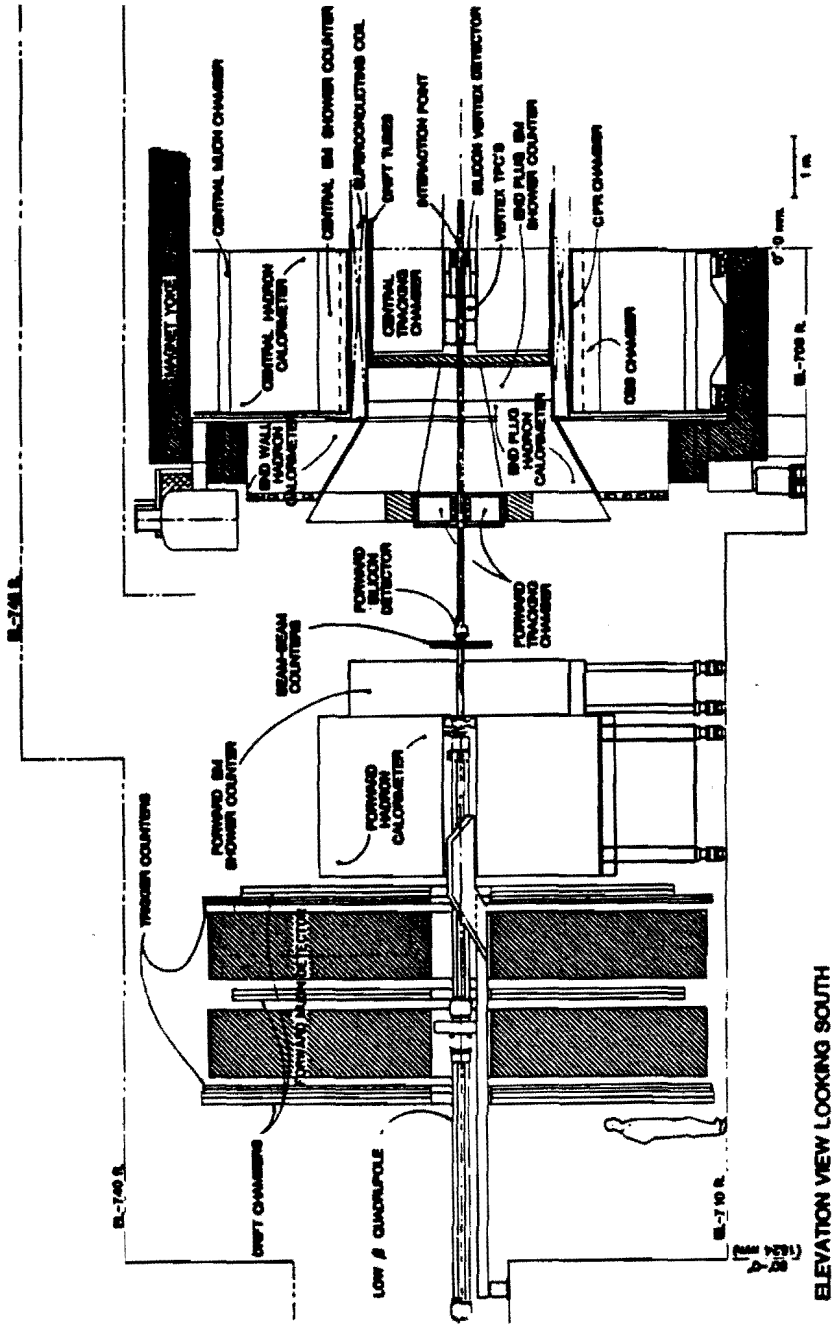

Fig. 2.1: View of one half of the CDF Detector. The calorimeters are divided into central, plug, and forward regions. Proportional chambers in the central region are placed at shower max (CES Chambers) and outside the solenoidal coil (CPR Chambers). Charged particle tracking is performed by the SVX, the VTX, and the CTC.

2.1.2 Calorimetry

Table 2.1 summarizes the calorimeter systems at CDF. In the central barrel region covering the angular region $40° < \theta < 140°$, or $-1.1 < \eta < 1.1$, the electromagnetic (CEM) and hadron (CHA, WHA) calorimeters are made of absorber sheets interspersed with scintillator with plastic light guides to bring the scintillator light up to two phototubes per EM tower. The towers are constructed in 48 wedges, each consisting of 10 towers in η by one tower in ϕ (see Figure 2.2). Proportional chambers are embedded near shower maximum, 6 radiation lengths (X_0) within the EM calorimeters. These chambers have wires in the r-ϕ view and cathode strips in the z view. Each calorimeter wedge contains two of these chambers (placed end-to-end in the η direction), called Central Electron Strip (CES) chambers. The CES is summarized in Table 2.2. A second set of proportional chambers, the Central Pre-Radiator (CPR), is placed in between the front face of the EM calorimeters and the magnet coil. This second set of proportional chambers acts as a shower pre-sampler.

In the plug end-cap and forward detector regions, requirements of fine tower segmentation and smaller physical size of the towers dictate the use of absorber sheets sandwiched with conductive plastic proportional tube arrays. Cathode strips outside the plastic tubes are read out and provide tower segmentation. Near shower maximum in the plug EM (PEM) calorimeter, a proportional tube layer with strips of four-times finer spacing provides shower profile information and precise shower position determination.

Arrays of scintillator planes are mounted on the front face of each of the far-forward EM shower counters. These planes, called the Beam-Beam Counters (BBC's) are shown in Figure 2.1 and are used to signal an inelastic collision. A coincidence of hits in each of the BBC's is required to initiate the trigger system. Each BBC consists of an array of 16 scintillator planes and 16 photomultiplier tubes that encircle the 360° around beam pipe and cover the polar angle region $3.24 < |\eta| < 5.90$.

Table 2.1 Description of the CDF Calorimetry Subsystems

	CEM	CHA,WHA	PEM	PHA	FEM	FHA
Energy Resolution ($\% / \sqrt{E}$)	13.5	80	28	130	25	141
Angular Coverage (in $\lvert\eta\rvert$)	< 1.1	< 1.3	1.1 - 2.4	1.3 - 2.4	2.2 - 4.2	2.3 - 4.2
Segmentation ($\Delta\eta \times \Delta\phi$)	0.1 × 15°	0.1 × 15°	0.1 × 5°	0.1 × 5°	0.1 × 5°	0.1 × 5°
Active Medium	lead, scintil-lator	iron, scintil-lator	lead, propor-tional tube	iron, propor-tional tube	lead, propor-tional tube	iron, propor-tional tube
Position Resolution (r-ϕ × z)[a]	0.2 cm × 0.2 cm[b]	10 cm × 5 cm	0.2 cm × 0.2 cm	2 cm × 2 cm	0.2 cm × 0.2 cm	3 cm × 3 cm
Longitudinal Depth	18 X_0, 0.3 Λ_{abs}	4.7 Λ_{abs}	19 X_0, 1.0 Λ_{abs}	5.7 Λ_{abs}	25 X_0, 0.8 Λ_{abs}	7.7 Λ_{abs}

[a] At 50 *GeV* incident energy [b] Using the CES chambers

Table 2.2 Description of the Shower Max Detector (CES) and Pre-Shower Detector (CPR).

	CES Chamber (2 per 15° wedge)		CPR Chamber (2 per 15° wedge)
	Wires (r-ϕ view)	Strips (z view)	Wires (r-ϕ view)
Number of Channels	64	64	32
Spacing (cm)	0.63	1.8	1.0
Spatial Resolution (cm)	0.2	0.2	0.5
Saturation Energy (*GeV*)	150	150	>150
Chamber length in z (cm)	115		103
Chamber Width in ϕ (°)	12.4		10.2

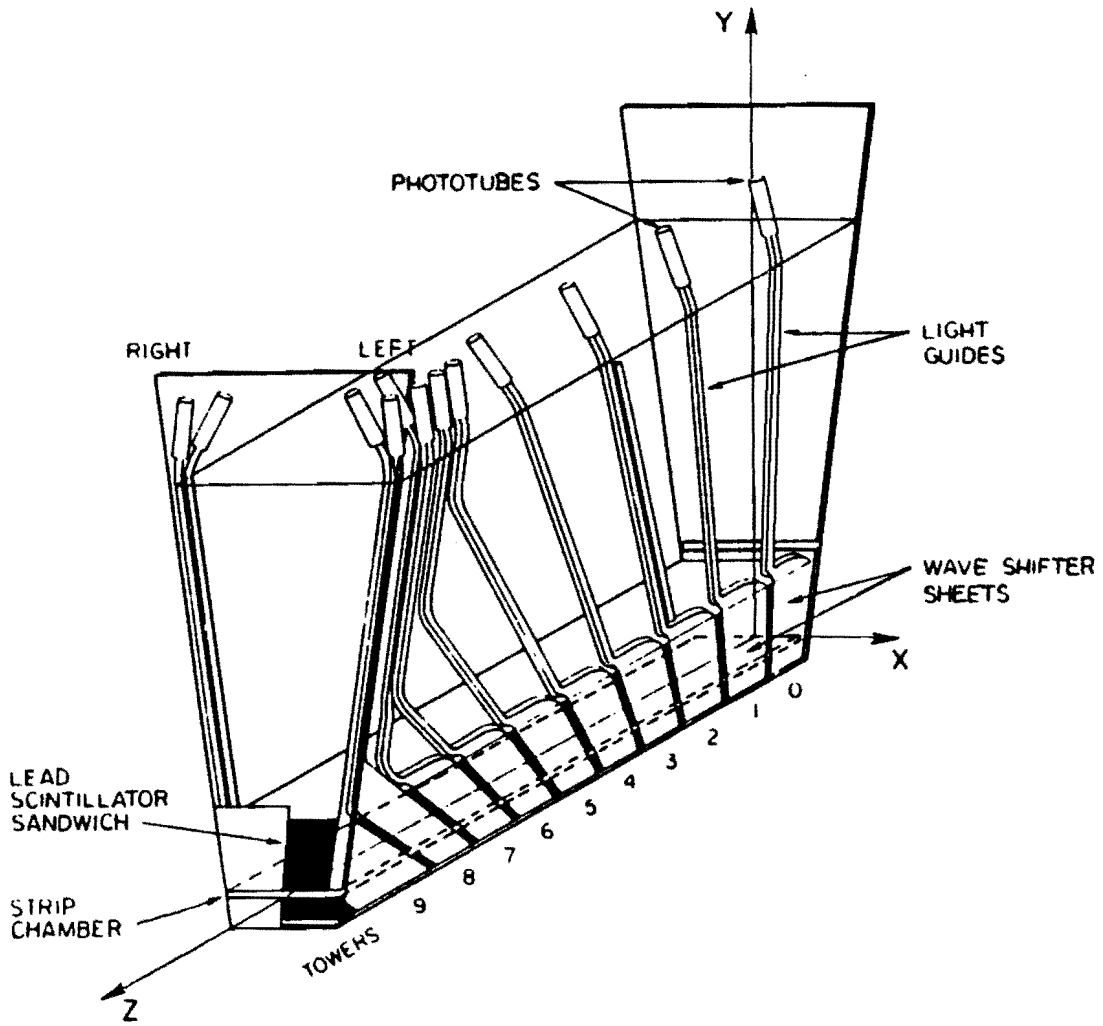

Fig. 2.2: View of one wedge of the central calorimeters. Each wedge covers 1 tower in the azimuthal direction ($\Delta\phi$ = 15°) and 10 towers in the η direction ($0 < |\eta| < 1.1$). One proportional chamber (CES chamber) is embedded at shower maximum in the range $0 < |\eta| < 0.613$ and another in the range $0.623 < |\eta| < 1.1$. Both edges (1° on either side of the 15° wedge) are uninstrumented in order to leave space for light guides that connect the scintillator to the PM tubes.

2.1.2 Charged Particle Tracking

Within the 14 kG axial magnetic field of the solenoidal magnet are three detectors for charged particle tracking. The Silicon Vertex Detector (SVX) is a four-layer silicon microvertex detector with single-sided readout to provide precise r-ϕ information for the reconstruction of track impacts. The Vertex Tracking Chamber (VTX) is a time projection chamber in 8 modules with a maximum drift distance of 10 *cm*. It provides reconstruction of the primary event vertex in the z direction with σ_z = 1 *mm* accuracy. The Central Tracking Chamber (CTC) is a large drift chamber with 84 layers of sense wires organized into 9 superlayers. Four of the superlayers are tilted ± 3° with respect to the z axis so as to provide stereo position measurement of charged particle tracks. The charge collected on its wires allow particle identification to be performed through dE/dx measurements with 1.5σ e-π separation at 5 *GeV/c*. The three tracking chambers are summarized in Table 2.3.

Table 2.3: Description of the Charged Particle Tracking Chambers

	Silicon Vertex Detector (SVX)	Vertex Tracking Chamber (VTX)	Central Tracking Chamber (CTC)
Polar Angle Coverage	$\lvert\eta\rvert < 1.0$	$\lvert\eta\rvert < 3.25$	$\lvert\eta\rvert < 1.5$
Inner, Outer Tracking Radii (cm)	2.7, 7.9	8, [a] 22	30.9, 132.0
Length (cm)	51	280	320
Layers	4	24	50 axial, 24 stereo
Strip or Wire Spacing	60 μm (inner 3 lay.) 55 μm (outer layer)	6.3 mm	10 mm
Spatial Resolution	15 μm (r-ϕ)	200-500 μm (r-z)	200 μm (r-ϕ) 6 mm (r-z)
Momentum Resolution	$\delta P_T/P_T = 0.001 \times P_T$ [b]	-	$\delta P_T/P_T = 0.002 \times P_T$
Thickness (θ = 90°)	≈ 0.035 X_0	≈ 0.045 X_0	≈ 0.015 X_0

[a] For inner 2 modules. Outer 6 modules are 3 cm inner radius.
[b] With both CTC and SVX hits incorporated into track fit.

2.2 Electron Cluster Candidates

Electron showers in the calorimeter are distinguished from hadron showers using a clustering algorithm. An electron cluster consists of a seed tower (the tower in the cluster with the largest energy) and shoulder towers (adjacent towers incorporated into the cluster). Towers with electromagnetic (EM) transverse energy $E_T > 3\ GeV$ are eligible to be seed towers. Towers with EM $E_T > 0.1\ GeV$ are eligible to be shoulder towers. Beginning with each seed tower, a cluster is formed by incorporating neighboring shoulder towers until either no further adjacent towers may be incorporated or until the maximum cluster size is reached. The maximum cluster size is restricted to three towers in pseudorapidity ($\Delta\eta \approx 0.3$) by one tower in azimuth ($\Delta\phi \approx 15°$) in the central region, five towers in pseudorapidity ($\Delta\eta \approx 0.5$) by five towers in azimuth ($\Delta\phi \approx 25°$) in the plug region, and seven towers in pseudorapidity ($\Delta\eta \approx 0.6$) by seven towers in azimuth ($\Delta\phi \approx 35°$) in the forward region. Finally, it is required that the EM E_T of the cluster be greater than $5\ GeV$ and that the ratio of hadronic E_T to electromagnetic E_T be less than 0.125.[32]

2.3 Fiducial Volume for Electrons

The fiducial volume of the detector is determined from the regions of the calorimeters which show relatively flat energy response for electrons. Figure 2.3 shows schematically the fiducial volume used in this analysis.

In the central region, the electron position, determined using the CES shower position, is required to lie within $21\ cm$ of the tower center in the r-ϕ view so that the shower is fully contained in the active region. The region $|\eta| < 0.05$, where the two halves of the detector meet, is excluded. The region $0.77 < \eta < 1.0, 75° < \phi < 90°$ is uninstrumented because it is the penetration for the cryogenic connections to the solenoidal magnet. In addition, the region $1.05 < |\eta| < 1.10$ is excluded because of the smaller depth of the electromagnetic calorimeter in this region.

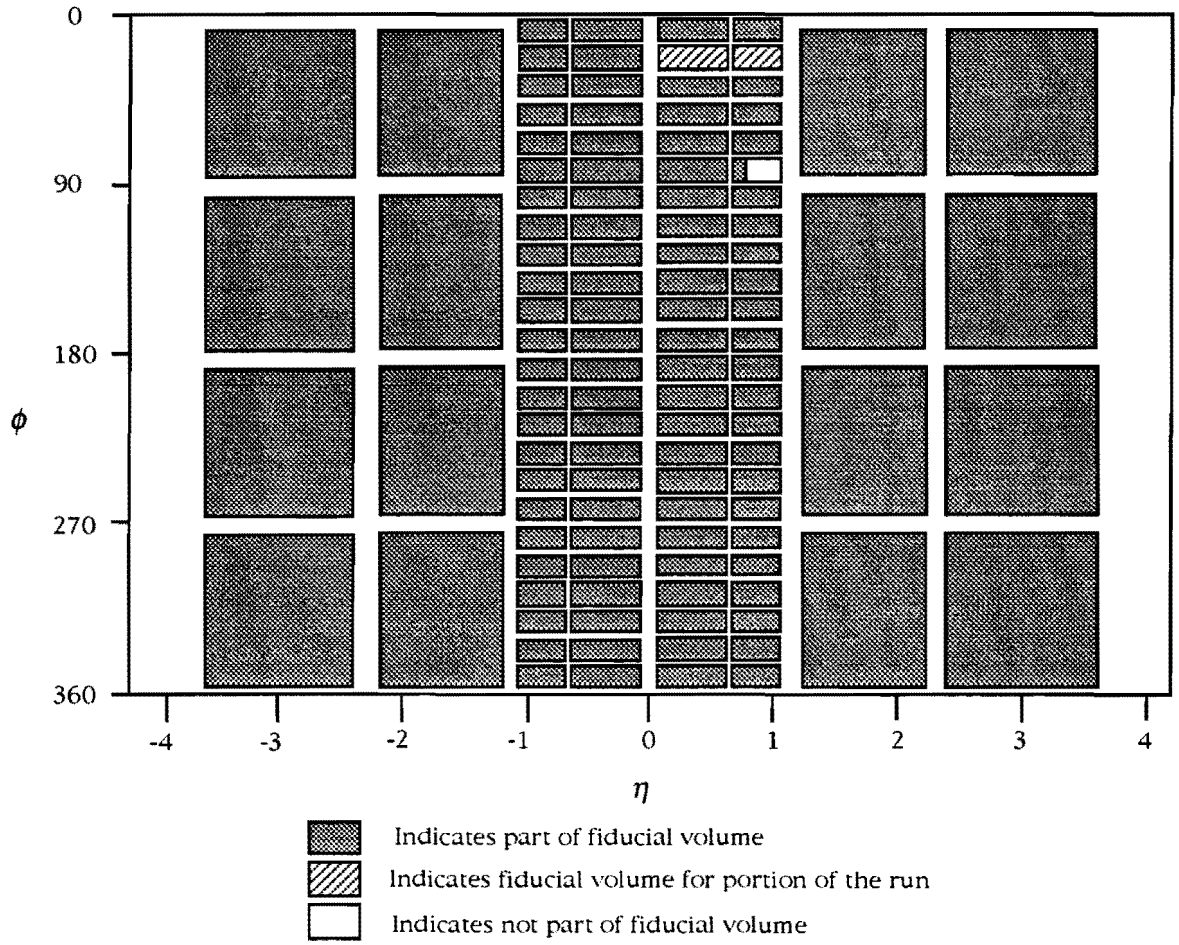

Fig. 2.3: Map in η-ϕ space of fiducial volume for electrons. The excluded regions are discussed in the text. Of the central region defined by $|\eta| < 1.1$, 78.9% of the volume is in the fiducial region for electrons; 78.5% of the volume $|\eta| < 3.6$ is in the fiducial volume for electrons. One calorimeter wedge is excluded for 39% of the luminosity of the physics runs because of a problem with the read-out electronics for this wedge.

In the plug and forward regions, the electron position is determined from the seed tower (see Section 2.1). The boundaries between detector regions, $1.1 < |\eta| < 1.2$ and $2.2 < |\eta| < 2.4$ are excluded because of the overlap between detectors. Finally, the region $3.6 < |\eta| < 4.2$ in the forward region is excluded. In both the plug and forward calorimeter, the electron seed tower is required not to be adjacent to the quadrant boundaries. This is $\pm$ 5° around each quadrant boundary.

2.4 Central Electron Identification

Electron identification in the central region is made more powerful by the presence of the Central Tracking Chamber, the Central Strip Chambers, and the Central Pre-Radiator. These additional detectors allow for much more stringent particle identification. Using the electron identification variables described here and the cut values in Table 3.1 for tight central electron candidates, the fraction of hadron jets falsely identified as electrons is estimated to be 2×10^{-5} for jets with $E_T > 20$ GeV (note at CDF it is more appropriate to speak of hadron jet misidentification rates than electron-pion rejection, since the dominant background to electron candidates is not isolated pions, but jets of hadrons). The CPR may be used to further reduce the misidentification rate by one order of magnitude. The purity of electron candidates with $E_T > 20$ GeV with the cuts of Table 3.1 is approximately 84%.

2.4.1 Calorimeter Transverse Profile

The transverse profile, or "*Lshr*," of a central electron is a measure of the lateral sharing of energy in the calorimeter towers of an electron cluster and is used to estimate the degree to which a calorimeter cluster resembles that of an electron. The lateral sharing of energy in a cluster is compared to

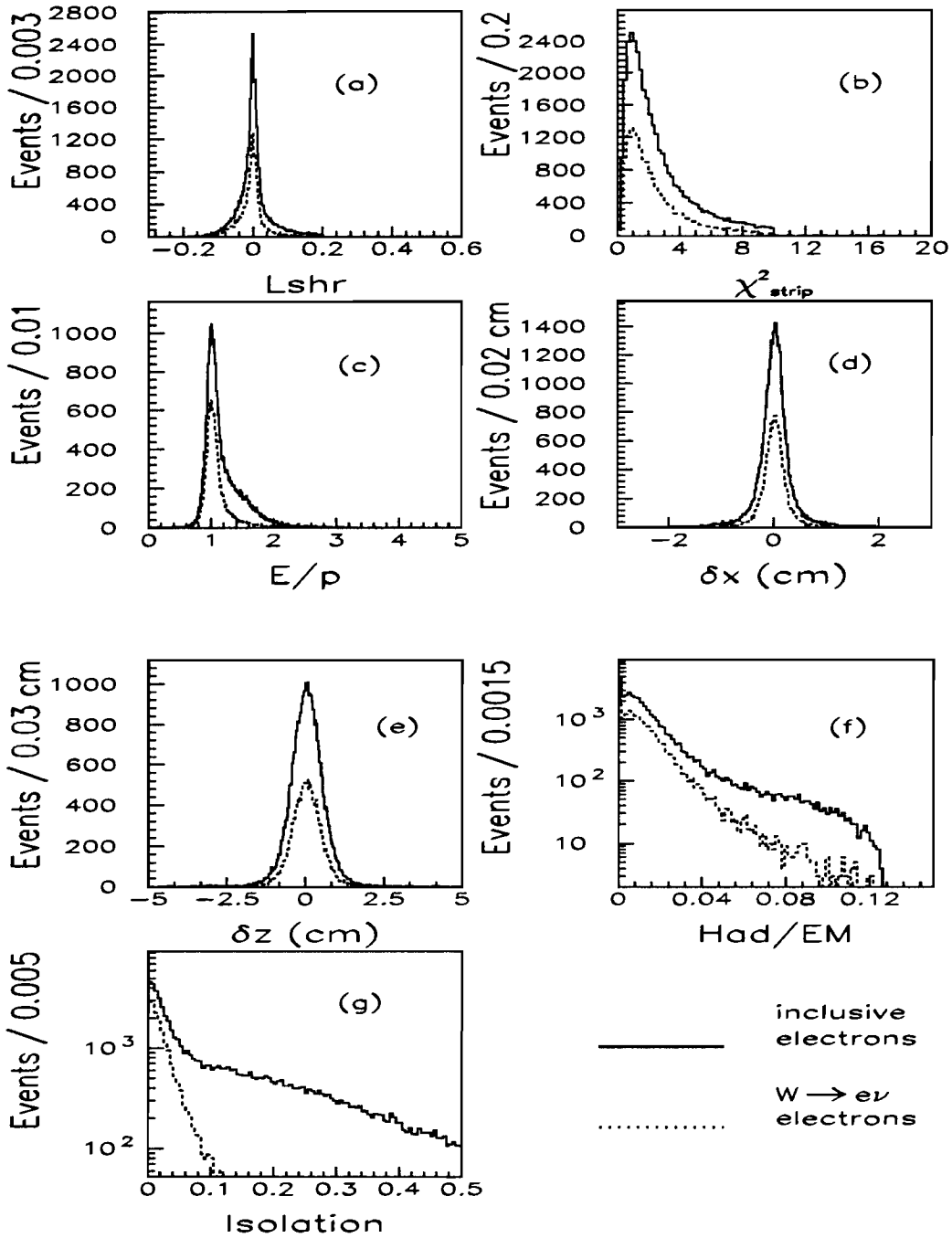

Fig. 2.4: Central identification variables for inclusive electrons and electrons from $W \to e\nu$ decays, as described in text. The relative area for the inclusive and W histograms corresponds to the relative yield in the data.

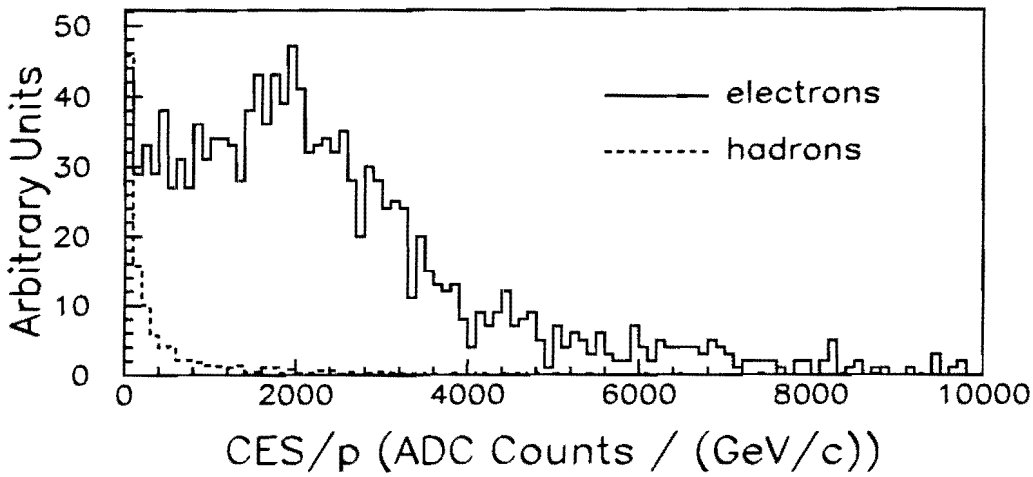

Fig. 2.5: Strip chamber (CES) pulse height for electrons and hadrons. The relative normalizations between the two shapes is arbitrary.

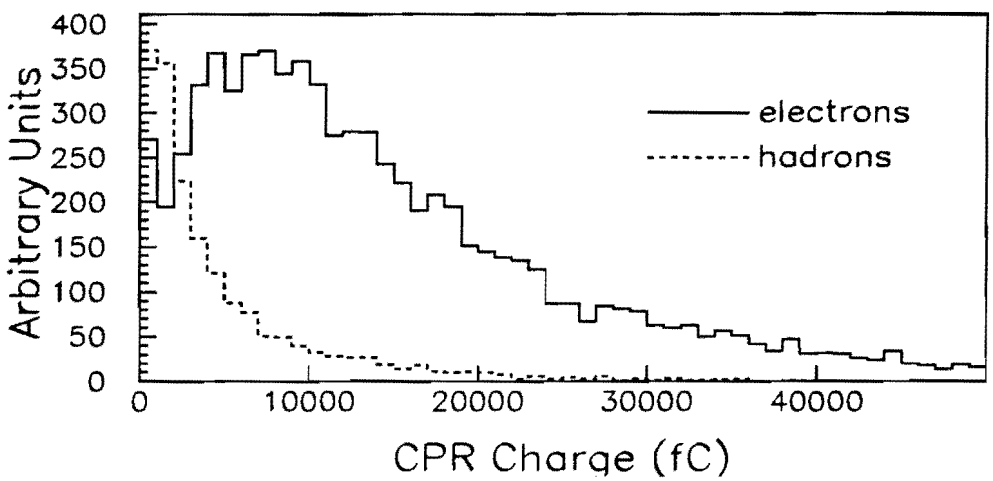

Fig. 2.6: CPR pulse height for electrons and hadrons. The relative normalizations between the two shapes is arbitrary.

electron shower shapes from test beam data and a χ^2 test is performed. The transverse profile variable, *Lshr*, is defined as:

$$Lshr = 0.14 \cdot \sum_i \frac{E_i^{Adj} - E_i^{Prob}}{\sqrt{0.14^2 \cdot E + (\Delta E_i^{Prob})^2}}$$

where E_i^{Adj} is the energy in a tower adjacent to the cluster seed tower, E_i^{Prob} is the expected energy in the adjacent tower, $0.14\sqrt{E}$ is the error on the energy measurement, and ΔE_i^{Prob} is the error on the energy estimate. E_i^{Prob} is calculated using a shower profile parameterization from test beam data. The distribution of *Lshr* for inclusive and *W* electrons is shown in Figure 2.4(a).

2.4.2 Strip Chamber Pulse Height

As mentioned above, a gas proportional chamber (CES chamber) is embedded 6 radiation lengths into the central electromagnetic calorimeter. This chamber is used to observe the longitudinal development of a shower. An electromagnetic shower in the calorimeters is generally initiated much earlier for an electron than for a hadron. Shown in Figure 2.5 is the variable $CES/p \equiv (\sum Q_i)/p$ for electrons and hadrons, where Q_i is the charge on a strip (in ADC counts), p is the track's momentum (in GeV/c), and the sum is over the 5 strips (z view) around the track's position extrapolated to the strip chambers.

2.4.3 Strip Chamber Pulse Height Shape

The pulse height shape in the CES is also used for electron identification. The pulse height shape is compared to test beam data using a χ^2 test. The variable χ^2_{strip} is the χ^2 of the fit of the energy deposited on the each of the 11 strips in the z in the CES shower compared to the test beam shape. A similar variable χ^2_{wire} tests the observed energy deposition shape on

the wires in the r-ϕ view.[32] The variable χ^2_{strip} for inclusive electron candidates and for electrons from W decays is shown in Figure 2.4(b).

2.4.4 Charged Track Requirement

Electromagnetic clusters in the calorimeters can arise from neutral particles, such as $\pi^0 \rightarrow \gamma\gamma$ decay. We require the presence of a charged track in the CTC for electron identification. We require the ratio of the electromagnetic energy, E, of the electron cluster measured in the calorimeter to the electron's momentum, p, measured in the central tracking chamber to lie in the range $0.5 < E/p < 2.0$. The variable E/p for inclusive electron candidates and for electrons from W decays is shown in Figure 2.4(c). The tail above $E/p > 1$ in W electrons is due to the radiation of photons by the electron as it passes through the material inside the CTC. The radiated photons generally land in the same calorimeter cell as the electron, so E has the same value as the initial electron energy, but p is smaller as it is measured in the CTC after the Bremsstrahlung radiation. This tail is larger in the inclusive electrons because of the presence of electrons from $\pi^0 \rightarrow \gamma\gamma \rightarrow \gamma e^+ e^-$, for which p is the momentum of one electron, but E is close to the energy of the π^0.

2.4.5 Track-Shower Matching Variables

The highest-momentum CTC track pointing to the electron cluster is extrapolated to the CES, and the extrapolated position is compared to the shower position as measured in the CES. The variable δx is the separation in the r-ϕ view between the extrapolated track position and the CES strip cluster position. The variable δz is the corresponding separation in the z view. Requiring the extrapolated position of the track to be close to the position of the electromagnetic shower reduces the background from overlaps of charged and neutral hadrons. The variables δx and δz for inclusive electron candidates and for electrons from W decays are shown in Figure 2.4(d,e).

2.4.6 CPR Pulse Height

The CPR pulse height on the two wires around a track is used to measure how early a shower occurs in the calorimeters. An electron may shower in the solenoid, while a hadron will leave only a minimum-ionizing pulse. The solenoidal coil thickness is 0.85 X_0 of material at normal incidence. Figure 2.6 shows the pulse height shapes for electrons and hadrons.

2.4.7 Electron Track Impact Parameter

The impact parameter of the electron's track is used to discriminate electrons of long-lived parent particles from those originating from short-lived parents. The lifetime of heavy quarks is long compared to the impact parameter resolution, while the lifetime of the W and Z^0 are infinitesimally short on this scale. The impact parameter, d_0, of charged tracks is determined with $\sigma_d \equiv 40\ \mu m$ resolution. For charged tracks with $P_T > 1\ GeV/c$, the dominant contribution to the resolution is the uncertainty in the primary vertex position.

The "signed impact parameter," D_{sign}, is defined for a track in the CTC pointing to a jet in the calorimeters. It is defined as:

$$D_{sign} = d_0 \cdot \frac{\mathbf{d_0} \cdot \mathbf{n}_{jet}}{|\mathbf{d_0} \cdot \mathbf{n}_{jet}|}$$

where $\mathbf{d_0}$ is the vector whose magnitude is the distance of closest approach of the charged track to the primary vertex and which points from the primary vertex to the point of closest approach of the track to the primary vertex. The unit vector $\mathbf{n}_{jet}$ points from the primary vertex to the energy centroid of the jet in the calorimeter. A track emanating from a long-lived parent will have positive D_{sign}, whereas a track from a short-lived particlewill have, on average, zero D_{sign}.

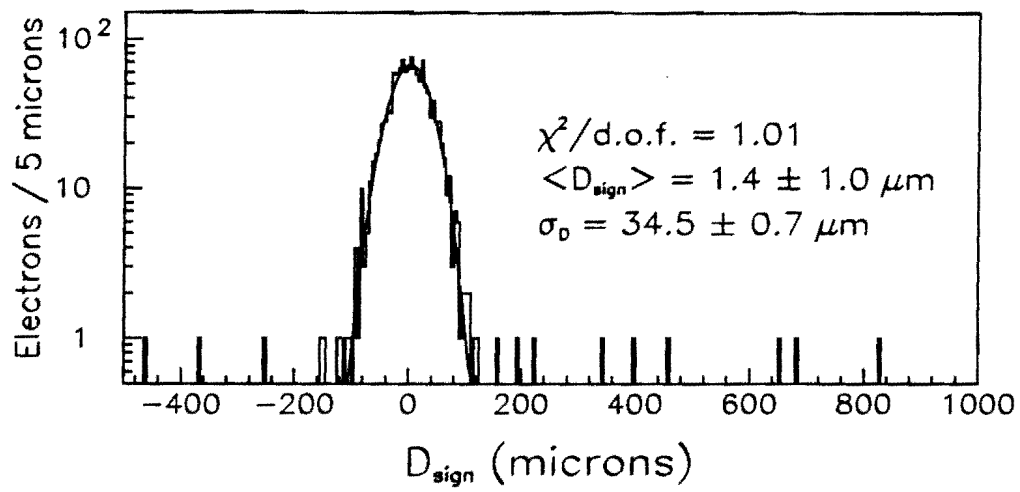

Fig. 2.7: Signed impact parameter for electrons from $Z^0 \rightarrow e^+e^-$ decays observed in the SVX detector.

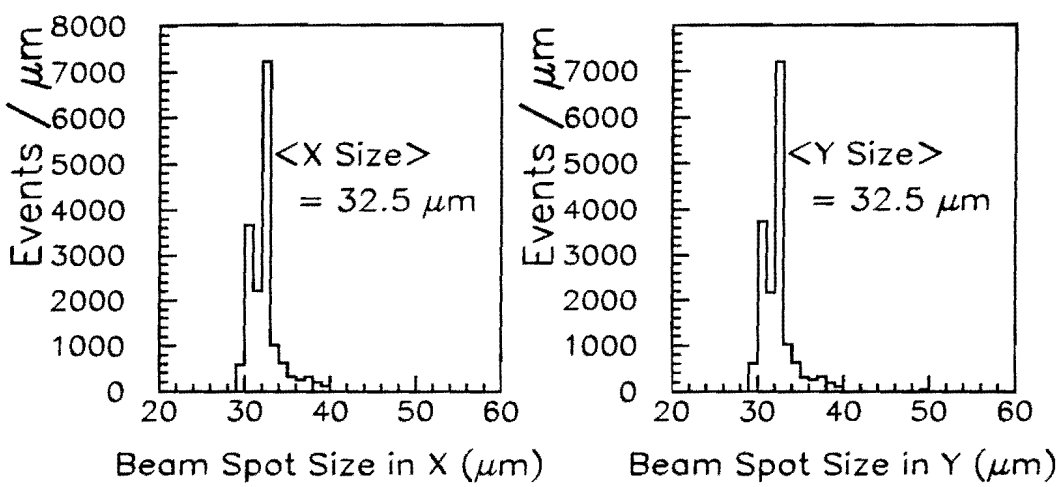

Fig. 2.8: Size in (a) the x and (b) the y view of the overlapping region of proton and antiproton beams for several physics runs (proton stores).

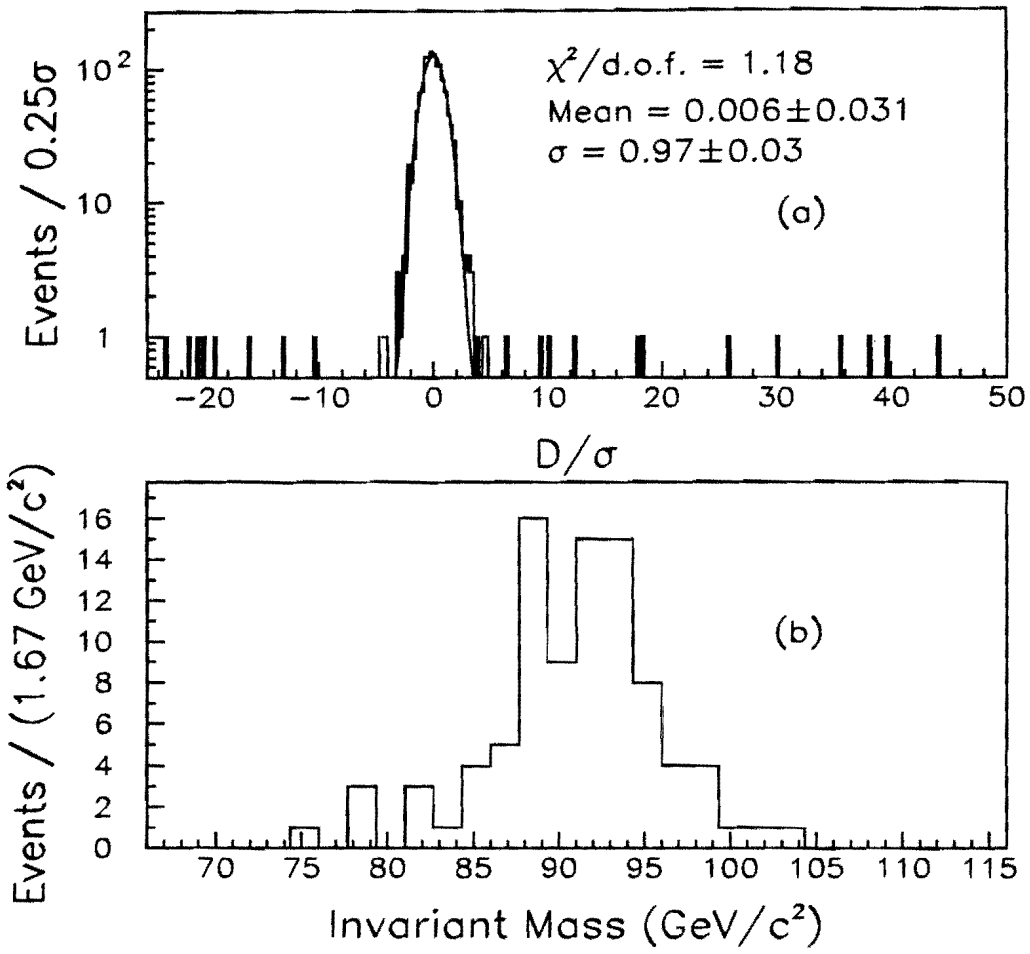

Fig. 2.9 (a): D/σ for electrons from $Z^0 \rightarrow e^+e^-$ decays. The σ agrees well with the sum of the estimated effects of beam spot size and multiple scattering.
(b): Invariant Mass for Z^0's with $D/\sigma > 2$.

Resolution effects smear the observed D_{sign} spectrum. Effects contributing to the resolution are: scattering in the beampipe before reaching the SVX; radiation of photons by the electron as it passes through the material in the tracking volume; and the location uncertainty of the primary vertex. The D_{sign} distribution for electrons from $Z^0 \rightarrow e^+e^-$ decays is shown in Figure 2.7. The observed σ corresponds well to our estimation of the primary vertex spread (see Figure 2.8), and the $\sigma = 10.7\ \mu m$ effect of Bremsstrahlung radiation on 20 - 40 GeV electron tracks (estimated from a Monte Carlo). The impact parameter significance, D/σ, is shown for electrons from $Z^0 \rightarrow e^+e^-$ decays in Figure 2.9 (a). Figure 2.9 (b) shows that the events in the tails are, in fact, Z^0's and not background. The non-gaussian tails in D/σ come from accidental hits in the SVX incorporated into the track fit.

2.4.8 Event Vertex Measurement

The position in z of the primary event vertex is measured by the Vertex Tracking Chamber (VTX). The z position of the event is distributed about the nominal interaction point by $\sigma = 26\ cm$ over the course of the run (see Figure 2.10). This spread is an average of many different σ's from different physics runs. Figure 2.11 demonstrates the stereo resolution of the tracking. It shows the difference in z between the origins of the two tracks from $Z^0 \rightarrow e^+e^-$ decays. The spread of the interaction point in z has implications for use of the SVX in physics analyses. The spread of the vertex position is larger than the length of the SVX. From studying the tracks from Z^0 decays, 61.9 $\pm$ 1.3 % of primary vertices are contained within the SVX.

2.4.9 Leakage into the Hadronic Calorimeters

The ratio ($\equiv$ Had/EM) of the energy in the hadronic towers of the electron cluster (Had) to the energy in the electromagnetic towers in the electron cluster (EM) is used to further select good electrons. The

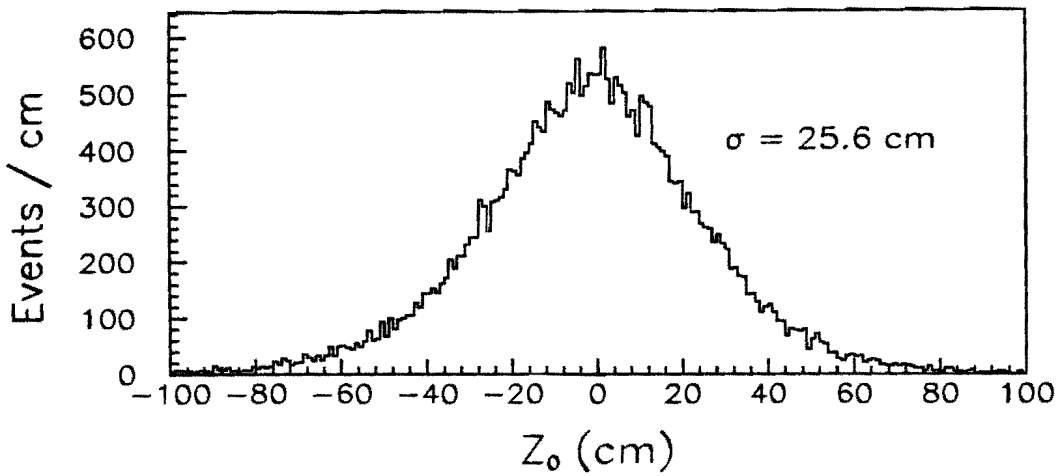

Fig. 2.10: Z_0 of event vertex for inclusive electron events.

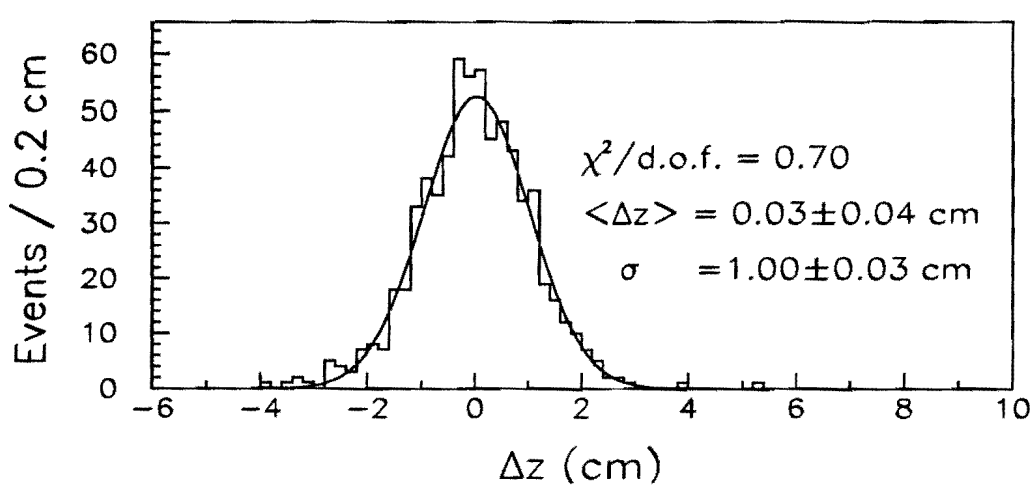

Fig. 2.11: Δz between electron tracks from $Z^0 \rightarrow e^+e^-$ decays when both electrons fall in the Central detector region.

electromagnetic calorimeters in the central consist of 18 radiation lengths of material, and so should nearly contain electromagnetic showers. Hadron showers will in general deposit energy in both the hadronic and electromagnetic compartments, and hence will have a larger value of Had/EM than do electrons. This quantity is physics-dependent, however, since isolated electrons should have less hadronic energy near by them than would electrons produced in association with hadrons (such as electrons from semileptonic b decay, which in general are associated with a jet of hadrons from the decay of the charmed meson). The variable Had/EM for inclusive electron candidates and for electrons from W decays is shown in Figure 2.4(f). As expected, the W electrons and the inclusive electrons have a different Had/EM shape.

2.4.10 Calorimeter Isolation

This cut, too, is not an electron identification cut but a topology cut. Electrons from W and Z^0 decay are expected to be "isolated." That is, they are not expected to be produced in association with other particles. As mentioned above, electrons from other physics processes are produced associated with jets of other particles nearby in η-ϕ space. This variable does not so much identify "good" electrons as it does select a particular type of physics process. We use the "isolation" variable, *Iso*, in order to select electrons not associated with other hadronic activity. The *Iso* variable is defined as:

$$Iso = \frac{E_T^{Cone} - E_T^{Cluster}}{E_T^{Cluster}}$$

where E_T^{Cone} is the sum of the electromagnetic and hadronic transverse energies in all of the towers (including the electron cluster) in a radius of $R = \sqrt{(\Delta\eta)^2 + (\Delta\phi)^2} = 0.4$ centered around the electron cluster, and $E_T^{Cluster}$ is the electromagnetic transverse energy in the electron cluster. The variable *Iso* for inclusive electron candidates and for electrons from W decays is shown in Figure 2.4(g). Again, the shapes are different.

2.5 Plug Electron Identification

The energy scale in the east and west halves of the PEM and FEM detectors is set using $Z^0 \rightarrow e^+e^-$ decays, where one electron falls in the CEM and the other lands in either the PEM or FEM. The scales are such that in the PEM, electron energies must be multiplied by a factor of 1.03 on the west half and 1.06 on the east half in order to achieve a Z^0 mass of 91.18 GeV/c^2. In the FEM, these factors are 1.05 and 1.006, respectively. Figure 2.12 shows the Z^0 mass in the central, plug and forward regions after these scale corrections have been applied.

The track-finding efficiency for tracks in the Central Tracking Chamber falls rapidly in the range of η covered by the plug calorimeters. Consequently, information from the CTC in the region covered by the plug calorimeters is not used in this analysis. To identify the presence of charged tracks pointing toward the cluster, the occupancy in the vertexing chamber (VTX) octant pointing towards the electron cluster is used. The ratio Had/EM is used, as is the isolation variable, *Iso*. The variable $\chi^2_{3\times3}$ is used. This variable is a fit of the lateral sharing of energy in the 3 towers in η by the 3 towers in ϕ around the electron cluster's center to the shape expected from test beam data. The distributions of these variables for events with a central electron and a plug electron are shown in Figure 2.13.

2.6 Forward Electron Identification

Electrons in the regions covered by the forward calorimeters are identified solely by the Had/EM, *Iso*, and VTX Occupancy variables. No tracking or lateral sharing variables are used. The distributions of these variables for events with a central electron and a forward electron are shown in Figure 2.14.

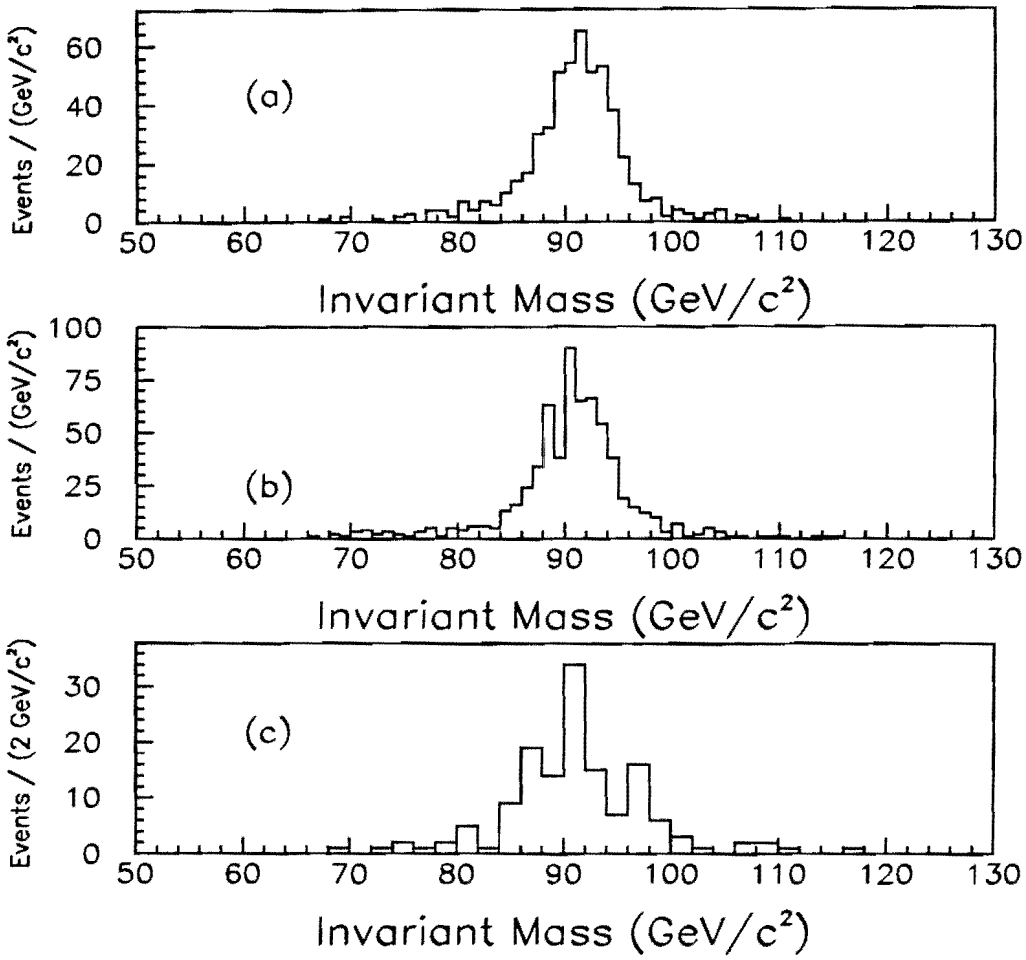

Fig. 2.12: Invariant mass of $Z^0 \rightarrow e^+e^-$ candidates where one electron falls in the Central region, and the second falls in the (a) Central, (b) Plug, and (c) Forward Regions.

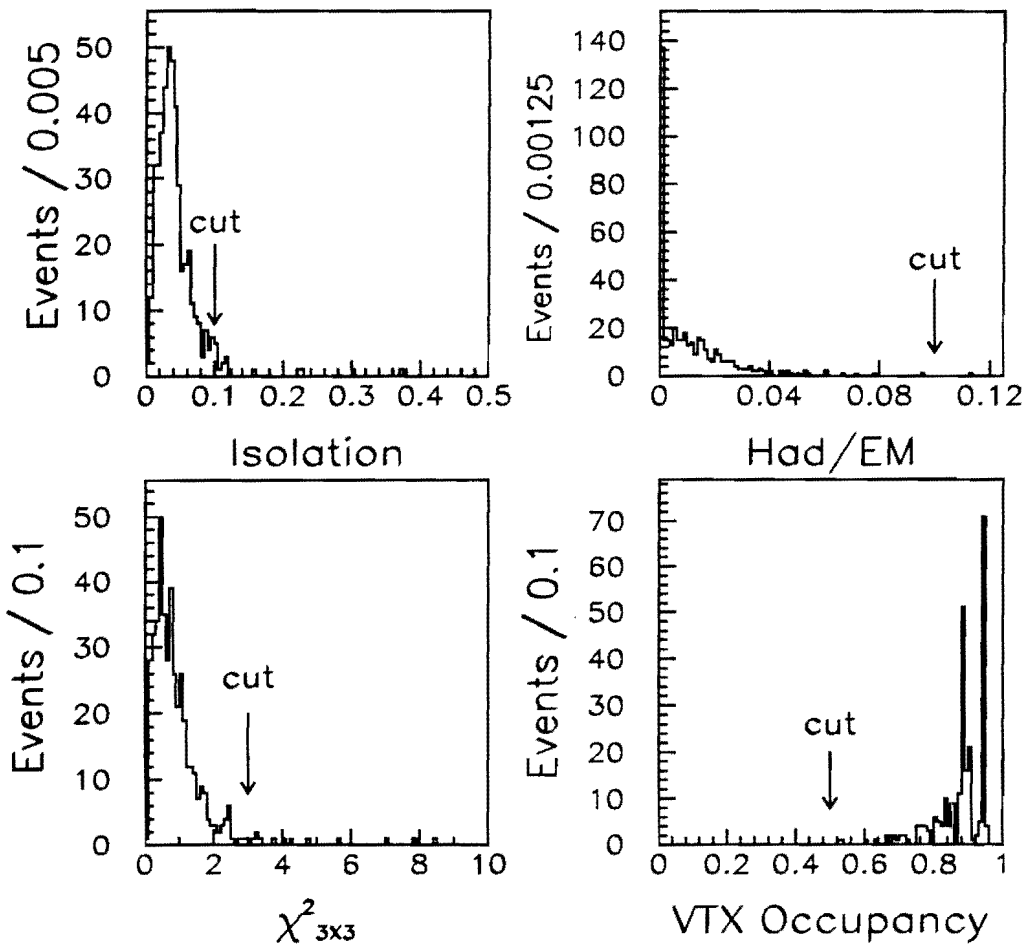

Fig. 2.13: Plug electron identification variables (see text) for events with one electron in the Central region and a second cluster in the Plug for which the pair forms an invariant mass with the first within the 81 - 101 GeV/c^2 mass range.

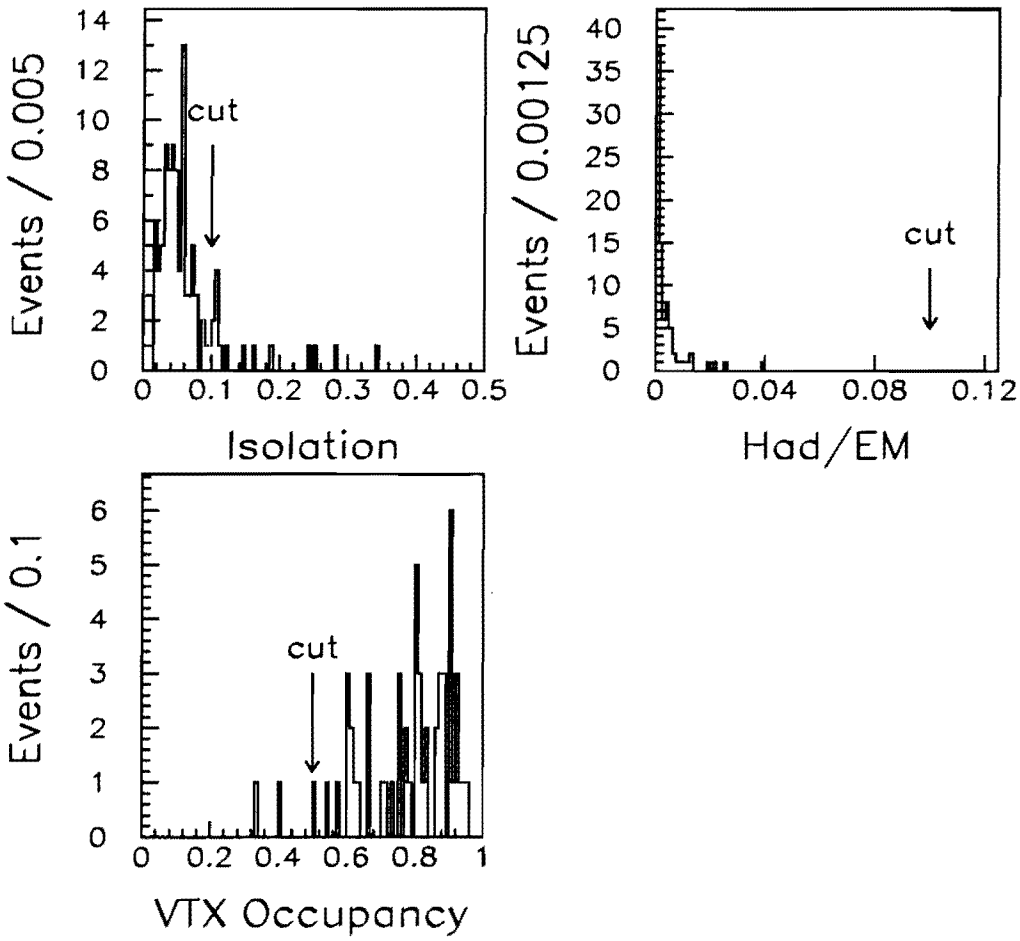

Fig. 2.14: Forward electron identification (see text) variables for events in which one electron in the Central region and a second cluster in the Forward for which the pair forms an invariant mass with the first within the 81 - 101 GeV/c^2 mass range.

2.7 Central Electron Trigger

The $p\bar{p}$ total cross section[34] is on the order of 70 mb at $\sqrt{s}$ = 1800 GeV. During the 1992 - 1993 run of CDF typical instantaneous luminosities of 5 x 10^{31} $cm^{-2}sec^{-1}$ delivered by the Fermilab Tevatron gave an event rate of 250 kHz. The CDF data acquisition system could write approximately 5 events per second to tape. We have constructed a three-level trigger[35] designed to obtain the necessary rejection factor. The first two levels are programmable FASTBUS-based hardware triggers, while Level 3 is a software trigger.

In the Level 1 trigger energies in physical calorimeter towers of $0.1 \times 15°$ in η-ϕ space are first summed into $0.2(\eta) \times 15°(\phi)$ trigger towers. The Level 1 electron trigger requires one trigger tower to be above a threshold of $E_T > 7$ GeV. It also requires a coincidence of hits in the two BBC's in order to signal an inelastic event. As shown in Figure 2.15, the efficiency of this trigger for fiducial electrons is 99.2 ± 0.1 % for electrons with $E_T > 10$ GeV.

Level 2 performs a cluster search and matches clusters to CTC tracks. EM trigger towers with transverse energy greater than a threshold of $E_T > 9$ GeV are cluster seeds. Adjacent EM towers to the seed towers are then added to the cluster as shoulder towers if they have $E_T > 7$ GeV. A cut of (EM+Had)/EM < 1.125 is imposed on electron candidate clusters. A hardware track processor[36] ("Central Fast Tracker", or CFT) searches for tracks in the r-ϕ plane in the CTC. For the electron trigger, a track of $P_T > 9.2$ GeV/c, as reconstructed by the CFT, is required to point to the electromagnetic cluster.

As shown in Figure 2.15, the Level 2 efficiency appears flat vs. E_T in the region of our concern (the threshold is at 9 GeV). The inefficiency of this trigger for W and Z^0 electrons is dominated by the CTC.[37] The overall efficiency of this trigger for W and Z^0 electrons in the fiducial volume was 91.5 ± 0.3 % for this run. This efficiency is not flat in η, however, as shown in Figure 2.16.

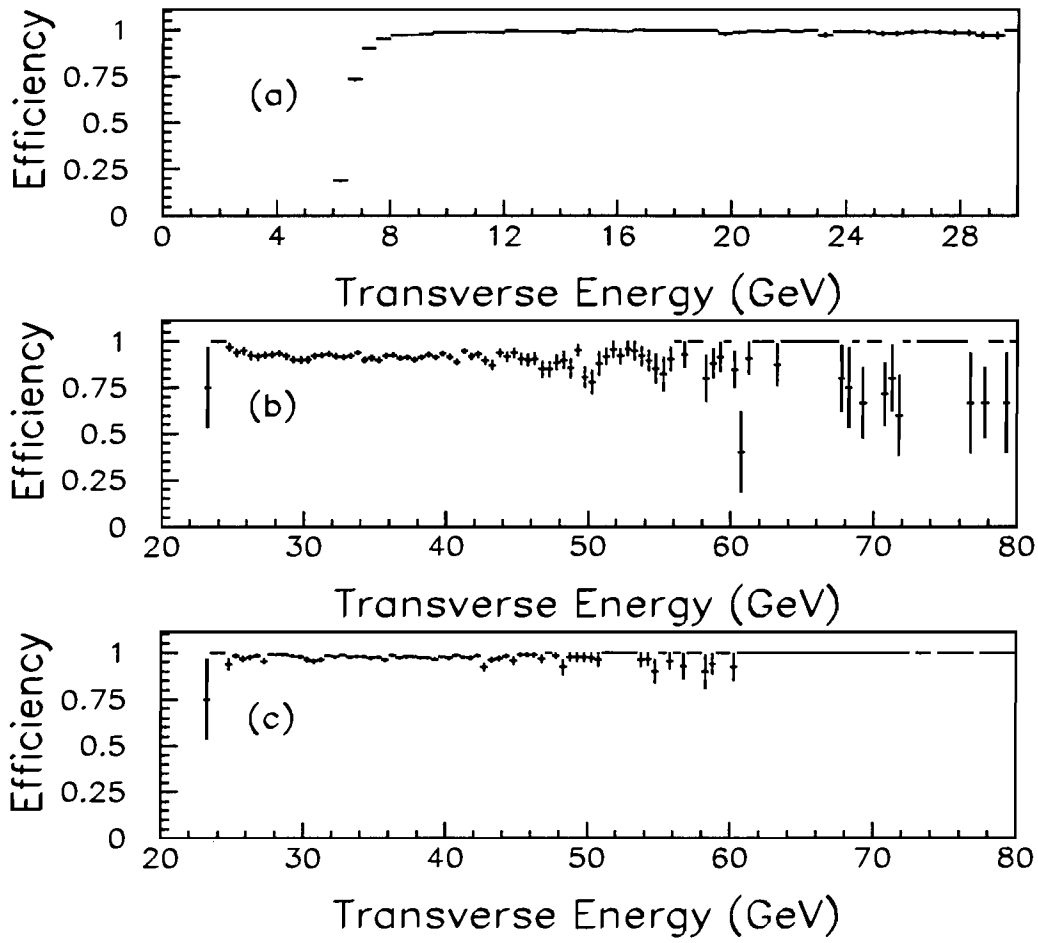

Fig. 2.15: Electron trigger efficiency in (a) Level 1, (b) Level 2, and (c) Level 3 *vs.* the electron E_T. The measurement of the electron trigger efficiency is described in Section 4.5.

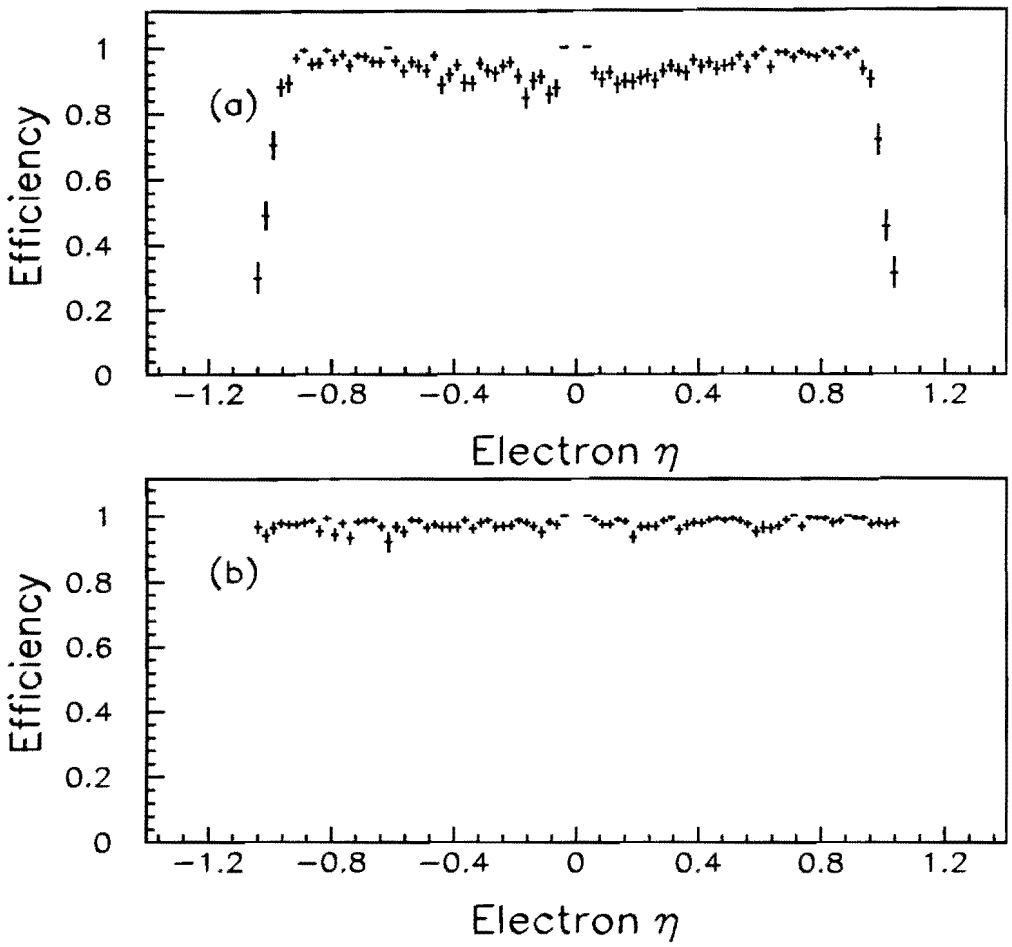

Fig. 2.16: Efficiency of the electron trigger *vs.* η (a) in Level 2 and (b) in Level 3. The Level 2 and Level 3 electron trigger efficiencies are determined from W decays that come in on a trigger that selects on $\not{E}_T$, as described in Section 4.5.

Level 3 is a software trigger which runs CDF's reconstruction code on an event. In the Level 3 electron trigger, an electron cluster is required with $E_T > 18\ GeV$. A three-dimensional track with $P_T > 13\ GeV/c$ is required to point to the electron cluster. The cuts $Lshr < 0.2$, $|\delta x| < 3\ cm$, and $|\delta z| < 5\ cm$ are imposed. For this run, the average Level 3 trigger efficiency for electrons in the fiducial volume is 98.2 ± 0.1 %.

2.8 Neutrino Identification

The calorimeter response to ΣP_T determines the resolution on the measurement of neutrino P_T, which is inferred by invoking momentum conservation. A non-interacting neutrino in our detector is signaled by the presence of a large momentum imbalance ("missing E_T," or $\not{E}_T$). The missing E_T is calculated from

$$\not{E}_T \equiv \sum_{|\eta|<3.6} \vec{E}_T^{\,i}$$

where $\vec{E}_T^{\,i}$ is a vector whose magnitude is the transverse energy in any calorimeter tower within the region $|\eta| < 3.6$ and whose direction points from the event vertex to the center of the calorimeter tower.

Events with perfect momentum balance and no resolution effects would have $\not{E}_T = 0$. The distributions of $\not{E}_T$ projected in the x and y directions are shown in Figure 2.17 for minimum bias triggers.[38] The smearing about 0 on each component (x and y) of $\not{E}_T$ is gaussian and the grows with the $\Sigma\ E_T$ in the calorimeter, as shown in Figure 2.18. At the $\Sigma\ E_T$ typical of W events, the resolution on $\not{E}_T$ is on the order of 3 GeV, while the neutrino P_T is of order 20 - 40 GeV. A figure of merit for the momentum imbalance is the "$\not{E}_T$ significance", S, defined as $S \equiv \not{E}_T / \sqrt{\sum E_T}$, which is a measure of how many standard deviations away from zero is the $\not{E}_T$ in a particular event. Figure 2.19 shows S for minimum bias events and for the W candidate events in our sample.

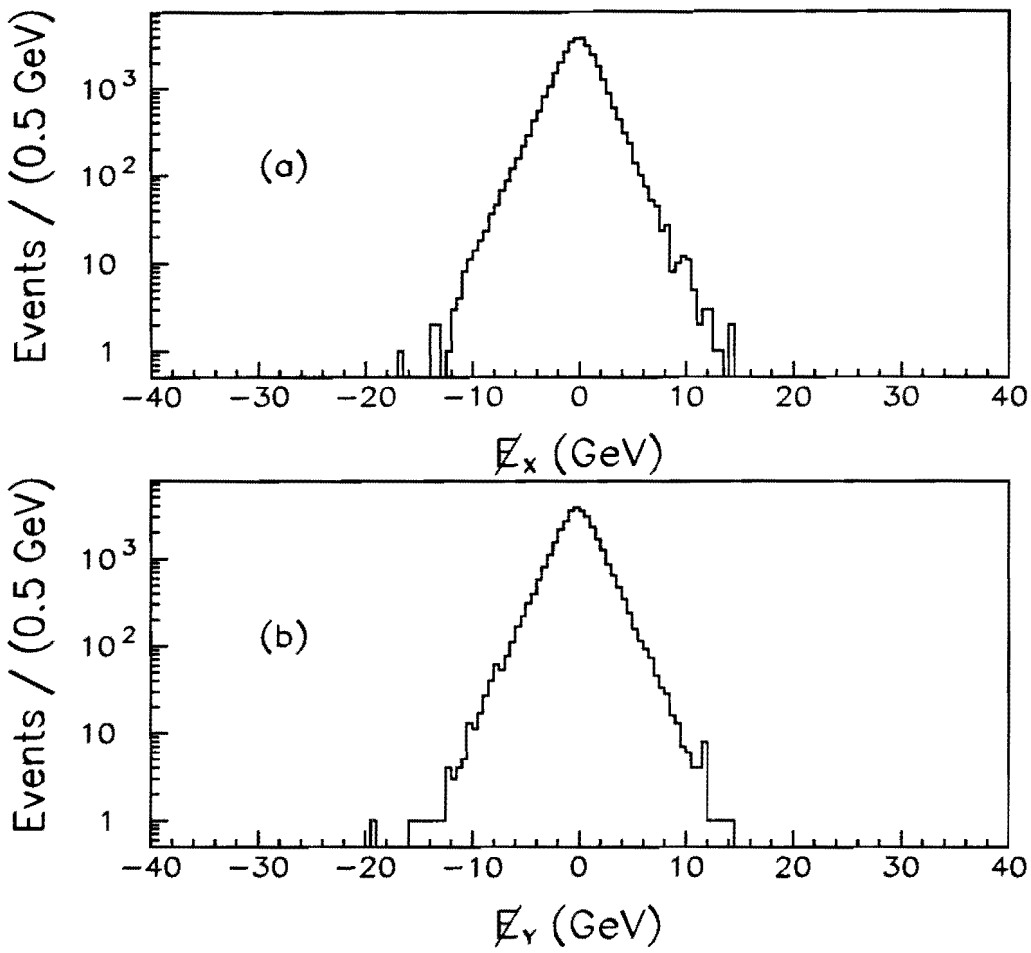

Fig. 2.17: E_X and E_Y for minimum bias trigger events. Minimum bias triggers require only a coincidence of hits in the forward and backward BBC's to signal an inelastic event. No calorimeter information is used in these triggers.

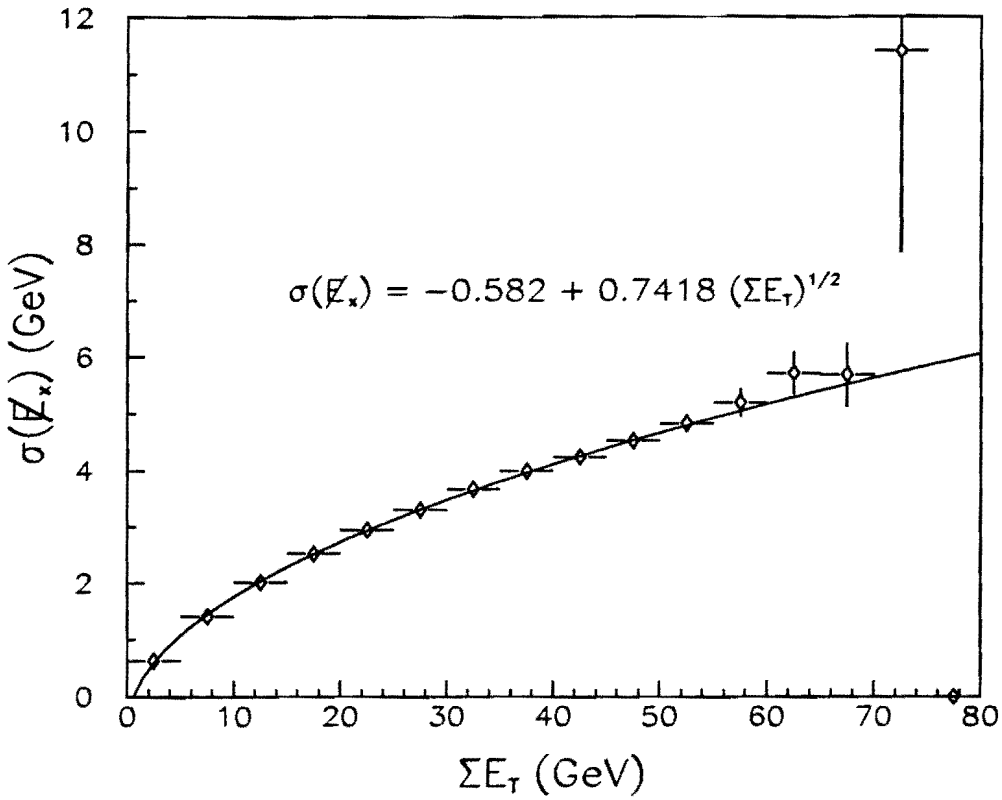

Fig. 2.18: Fitted $\sigma(E_x)$ *vs* $\Sigma(E_T)$ in minimum bias trigger events. The minimum bias data are placed in bins of $\Sigma(E_T)$; the quantity E_x is histogrammed and then fitted to gaussians with widths $\sigma(E_x)$. The curve is a best fit of a square root function to the data. The curve does not pass through the origin because run-by-run offsets and out-of-time accidental energy were not corrected for.

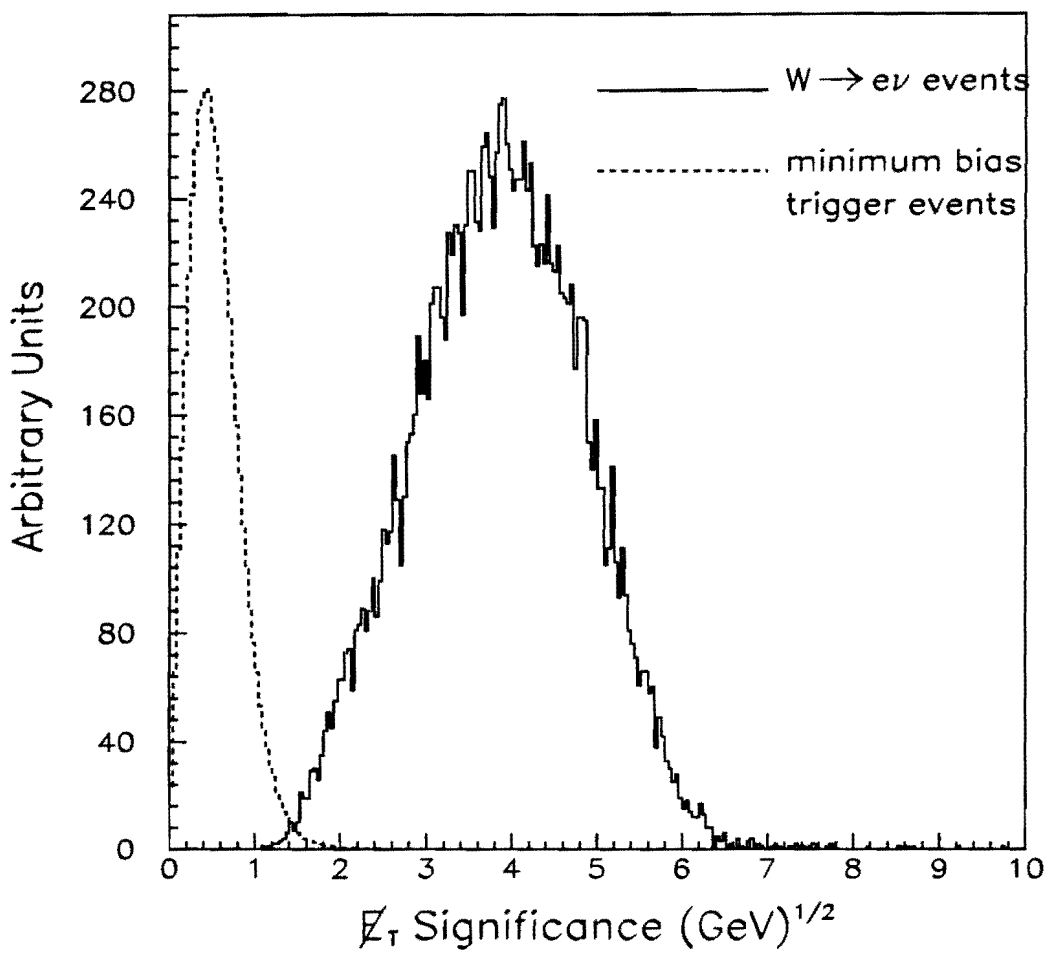

Fig. 2.19: The missing E_T significance, defined as $\not{E}_T / \sqrt{\sum E_T}$, for the W candidate events and for a sample of minimum-bias-triggered events. The relative normalizations between the two samples is arbitrary. We note, however, that the $W \to e\nu$ cross section is approximately 2 nb, while the minimum bias cross section is approximately 40 mb.

Chapter 3

Inclusive Electron Sample

Inclusive high-P_T electrons are produced in hadron collisions in decays of the electroweak bosons, such as $W \rightarrow e\nu$, $Z^0 \rightarrow e^+e^-$, or $Z^0 \rightarrow \tau^+\tau^-$ and $W \rightarrow \tau\nu$, where one of the τ's decays to an electron. High-P_T electron clusters are also produced in *QCD* processes, where the electron is embedded in a high P_T jet of hadrons. The processes in hadronic jets that can produce an electron cluster are (1) electrons which come in e^+e^- pairs, either from photon conversions or Dalitz decays; (2) semileptonic decays of heavy quarks, $b \rightarrow ce\nu$ or $c \rightarrow se\nu$, and (3) fake electron clusters which are really hadron showers that pass our electron identification cuts. The types of hadrons which would pass our electron identification cuts are overlaps of $\pi^{\pm}$ and π^0 showers, which thus produce a charged track and an electromagnetic cluster, and pion "charge exchange," $\pi^{\pm} + N \rightarrow \pi^0 + N$, which can occur in the calorimeters. This chapter describes the separation of a sample of inclusive electrons into three sub-samples: a sample of electrons from W decays, a sample from Z^0 decays, and a sample of non-W/Z^0 electrons. Chapters 4, 5, and 6 will describe these samples further and discuss the cross-contamination between the samples.

Candidate events for $W \rightarrow e\nu$ and $Z^0 \rightarrow e^+e^-$ decays are selected from the common sample of inclusive high-P_T electrons located in the central detector region which pass tight cuts. Requiring tight cuts on a central electron serves three purposes. First, the well-understood central region has added information from the tracking and the strip chambers that can be used to

suppress backgrounds from other physics processes. Second, the tight cuts on the central electron allow us to place loose, highly efficient cuts on the second lepton (the neutrino in the case of W decays and the second electron in the case of Z^0 decays). Third, and perhaps most importantly, selecting both W and Z^0 candidate events from such a common sample of inclusive electrons cancels several systematic uncertainties in the ratio of the W and Z^0 cross sections.

3.1 Central Electron Selection

The selection criteria for a high-P_T, central, tight electron are listed in Table 3.1 below. Note that the Z_{vertex} cut is not so much an electron identification cut as a fiducial cut: centering the event in the detector preserves the projective nature of the towers.

Table 3.1: Inclusive Central Electron Cuts

E_T	>	20 GeV
0.5	<	E/p < 2.0
$Lshr$	<	0.2
χ^2_{strip}	<	10.0
$\lvert\delta x\rvert$	<	1.5 cm
$\lvert\delta z\rvert$	<	3.0 cm
$\frac{\text{Had}}{\text{EM}}$	<	$0.045 + 0.055 \cdot \frac{E}{100}$
$\lvert Z_{vertex}\rvert$	<	60 cm
Electron triggers the event		

In addition to the above definition for a tight central electron, we define a tight, isolated central electron as one which passes the cuts listed in Table 3.1 and also has $Iso < 0.1$. Iso is not an identification variable, but an event topology cut. W and Z^0 electrons are expected to be isolated, but electrons from other physics processes may not be. A total of 50861 events pass the tight electron event selection criteria in an exposure of 21.7 pb^{-1}. A total of 30349 of these electrons pass our tight, isolated electron event cuts. The E_T spectra of the tight electrons and the isolated tight electrons are shown in Figure 3.1. A peak from the Jacobians of the W and Z^0 is already apparent.

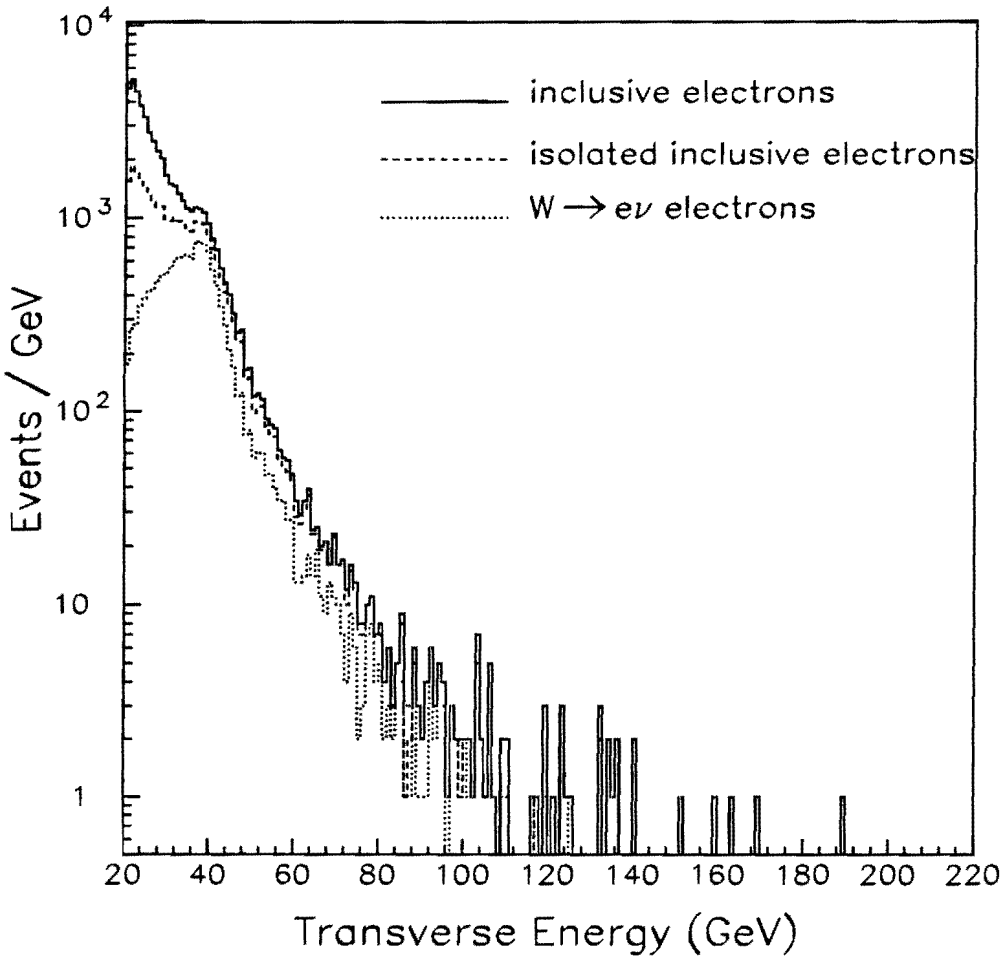

Fig. 3.1: E_T of inclusive electrons, isolated inclusive electrons, and electrons from $W \rightarrow e\nu$ decays.

3.2 Z^0 Sample Selection

Z^0 candidates are selected from the inclusive electron sample by requiring that the tight central electron be isolated and also requiring a second isolated electron which passes loose selection criteria. The cuts on the second electron are listed in Table 3.2 below.

Table 3.2: Z^0 Selection Cuts

-One tight, isolated central Electron		
-Second Electron passing loose cuts:		
central:		
	E_T	> 20 GeV
	-Charged track in CTC (opposite in sign to tight central electron)	
	E/p	< 2.0
	Had/EM	< 0.1
	Iso	< 0.1
plug:		
	E_T	> 15 GeV
	$\chi^2_{3\times3}$	< 3.0
	Had/EM	< 0.1
	Iso	< 0.1
forward:		
	E_T	> 10 GeV
	Had/EM	< 0.1
	Iso	< 0.1
$66\ GeV/c^2 < M_{(ee)} < 116\ GeV/c^2$		

Figure 3.2 shows the invariant mass distribution of electron pair candidates with a tight central electron and a second electron cluster with $E_T > 10$ GeV and Had/EM < 0.125. A Z^0 peak is already prominent. Figure 3.3 shows the invariant mass spectrum of electron pairs passing the loose cuts on the second lepton. We observe 1312 events which fall in the 66 - 116 GeV/c^2 mass range. Figure 3.4 shows the distribution in η of the second lepton of the 1312 Z^0 candidates. Table 3.3 shows that the distribution in η of the second lepton corresponds well to expectations from the Monte Carlo when the different detector efficiencies and backgrounds are taken into account. The Monte Carlo is normalized to the number of Z^0 events.

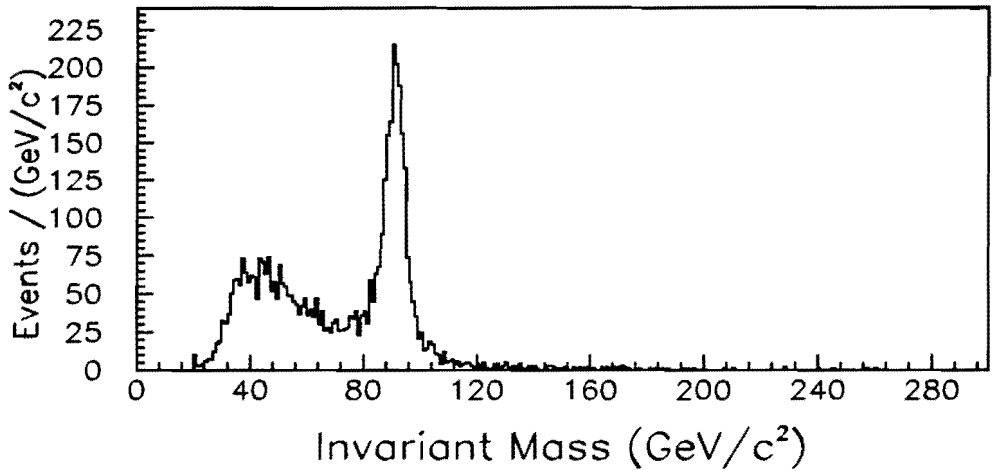

Fig. 3.2: Invariant mass spectrum of e^+e^- pairs with no cuts imposed on the second electron.

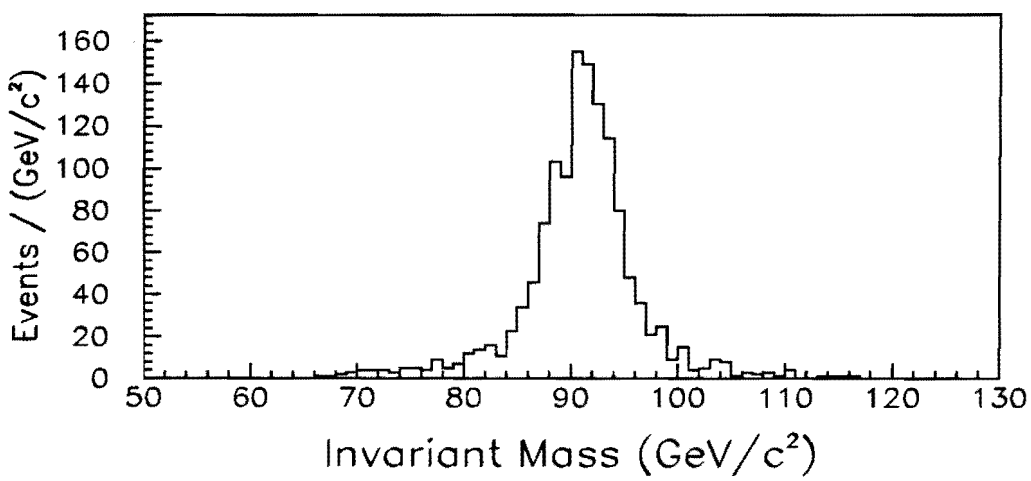

Fig. 3.3: Invariant mass spectrum of e^+e^- pairs with cuts in Table 3.2 imposed on the second electron.

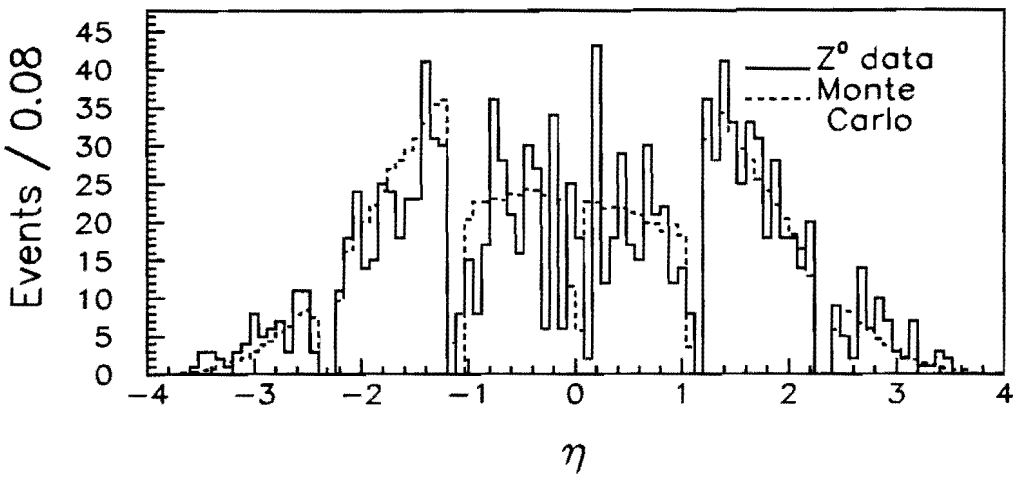

Fig. 3.4: Distribution in η of the second electron in $Z^0 \rightarrow e^+e^-$ decays for the data and the Monte Carlo described in Chapter 7. The Monte Carlo is normalized to the same area as the data.

Table 3.3: Z^0 Yield in Different Detector Regions

Detector in which 2nd Lepton Falls	Z^0 Candidate Yield	Z^0 Background (see Chap. 6)	Z^0 Signal (Yield - Background)	Monte Carlo Expectation
Central	529	1 ± 1	528 ± 1	535 ± 13
Plug	640	14 ± 14	626 ± 14	618 ± 13
Forward	143	6 ± 3	137 ± 3	138 ± 8

3.3 W Sample Selection

To select W's from the inclusive electron sample, we require a tight, isolated central electron in the event, and in addition we require:

- $\not{E}_T > 20\ GeV$
- Event does not posses a second electromagnetic cluster which forms a mass with the first electron in the 66 - 116 GeV/c^2 range

Figure 3.5 shows the *Iso* of the electron in the event *vs.* the $\not{E}_T$ in the event. The W's appear as a cluster at low *Iso*, high $\not{E}_T$. The $\not{E}_T$ spectrum of the isolated, tight inclusive electrons is shown in Figure 3.6. A total of 13796 events have $\not{E}_T > 20\ GeV$ and pass our Z^0 rejection cuts. The transverse mass of the W candidates is shown in Figure 3.7. Figure 3.8 shows the distribution in η of the electrons from the W candidates. The Z^0 removal cut removes 41 events.

3.4 Non-W/Z^0 Electron Sample Selection

The W and Z^0 samples selected above are contaminated by electrons from other physics processes. The backgrounds of electrons from hadron jets are particularly important to understand, so we select a sample of these electrons from hadronic processes for further study. This section describes the selection of a sample of electrons from hadron jets. In Chapter 4 we examine the make-up of this sample and determine the fractions, f_{conv}, f_b, and f_{fake} of conversions, heavy quarks, and fake electron clusters. The techniques used in Chapter 4 are then employed in Chapter 5 as a cross-check to determine the contamination of the $\not{E}_T > 20\ GeV$ sample from these hadronic processes.

The sample of non-W/Z^0 electrons is selected as follows. From the inclusive electron sample of 50861 events, events which have a second cluster which passes cuts of Had/EM < 0.1 and $Iso < 0.1$ are removed in order to reject electrons from $Z^0 \rightarrow e^+e^-$ and Drell-Yan pair production. Approximately 4600 events are removed by this cut. Events which have $E_T > 10$ GeV are rejected in order to remove electrons from $W \rightarrow e\nu$ or $W \rightarrow \tau\nu \rightarrow e\nu\nu$. 21637 events survive this cut. Some residual electrons from $W \rightarrow e\nu$, $Z^0 \rightarrow e^+e^-$, $W \rightarrow \tau\nu$ or $Z^0 \rightarrow \tau^+\tau^-$ may exist in our sample, but the contamination in this sample from all electroweak sources is estimated[39] to be 1.0 ± 0.2 %. Finally, we require a hadronic jet with $E_T > 10$ GeV and electromagnetic fraction less than 0.8, which reduces the electrons from weak boson decays to 0.4 ± 0.1 % of the sample. There are 17805 electrons passing all of these cuts which we use as our control sample of non-W/Z^0 electrons.

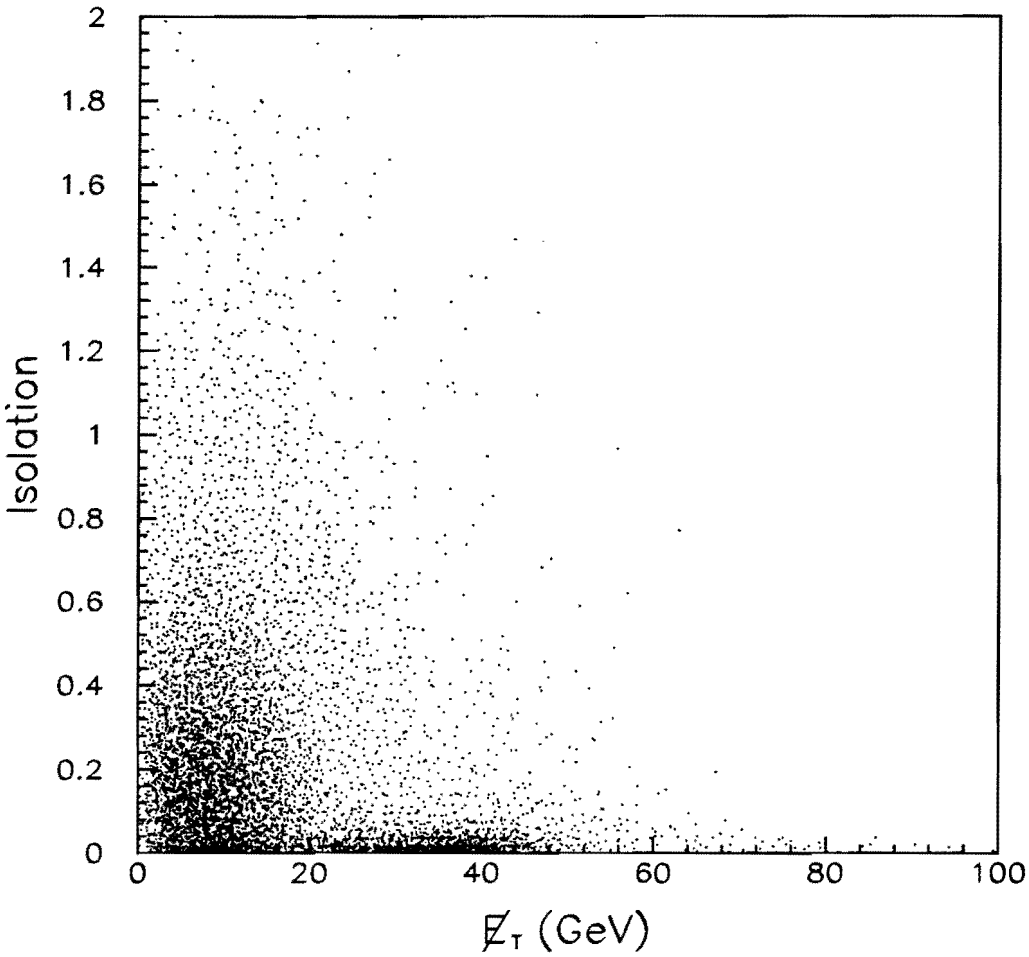

Fig. 3.5: Isolation of the electron *vs.* the $\not{E}_T$ in the event. Events with a second electromagnetic cluster have been explicitly removed from this plot. The electrons from W decays appear at high $\not{E}_T$ and low *Iso*, and the remaining electrons from hadron jets appear at low $\not{E}_T$ and all values of *Iso*.

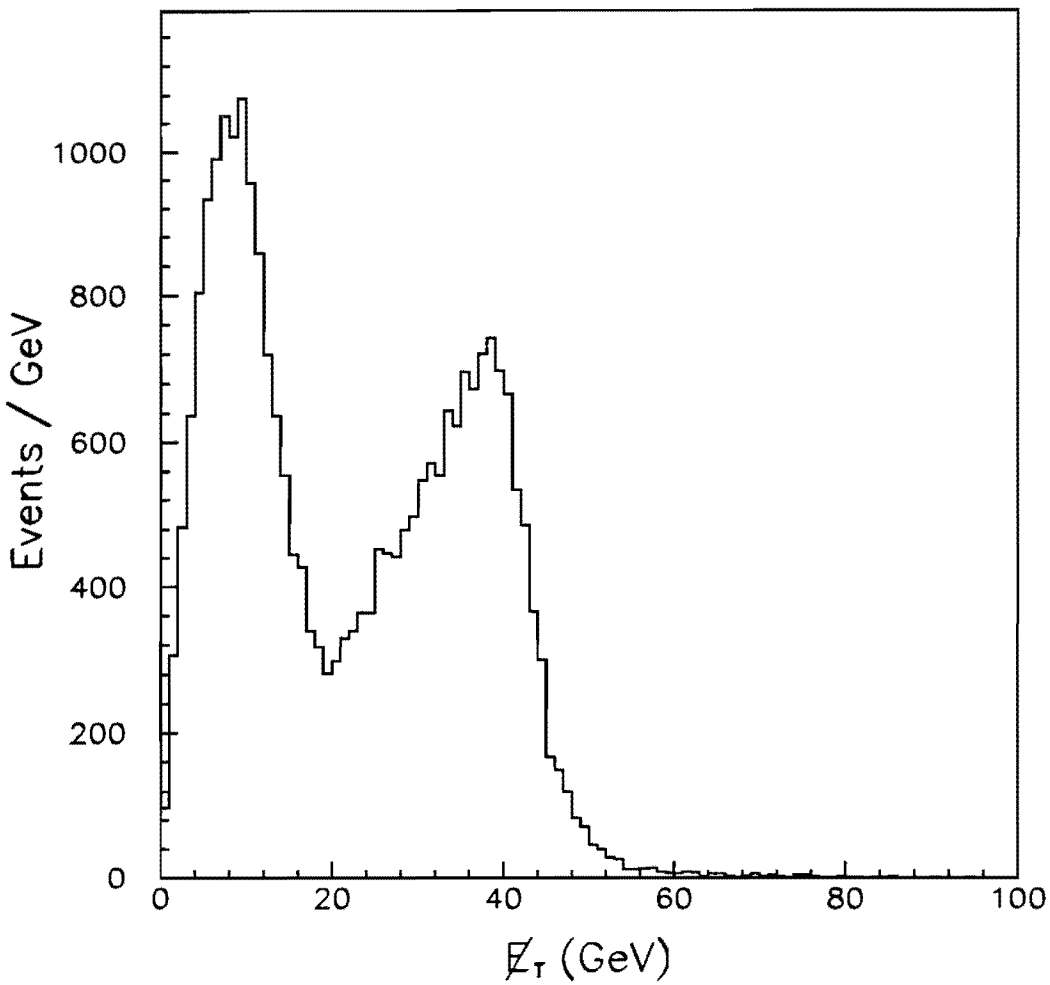

Fig. 3.6: $\not{E}_T$ spectrum of isolated inclusive electrons. The peak at approximately 8 *GeV* is due to resolution effects and the peak at 40 *GeV* is due to neutrinos from *W* decays.

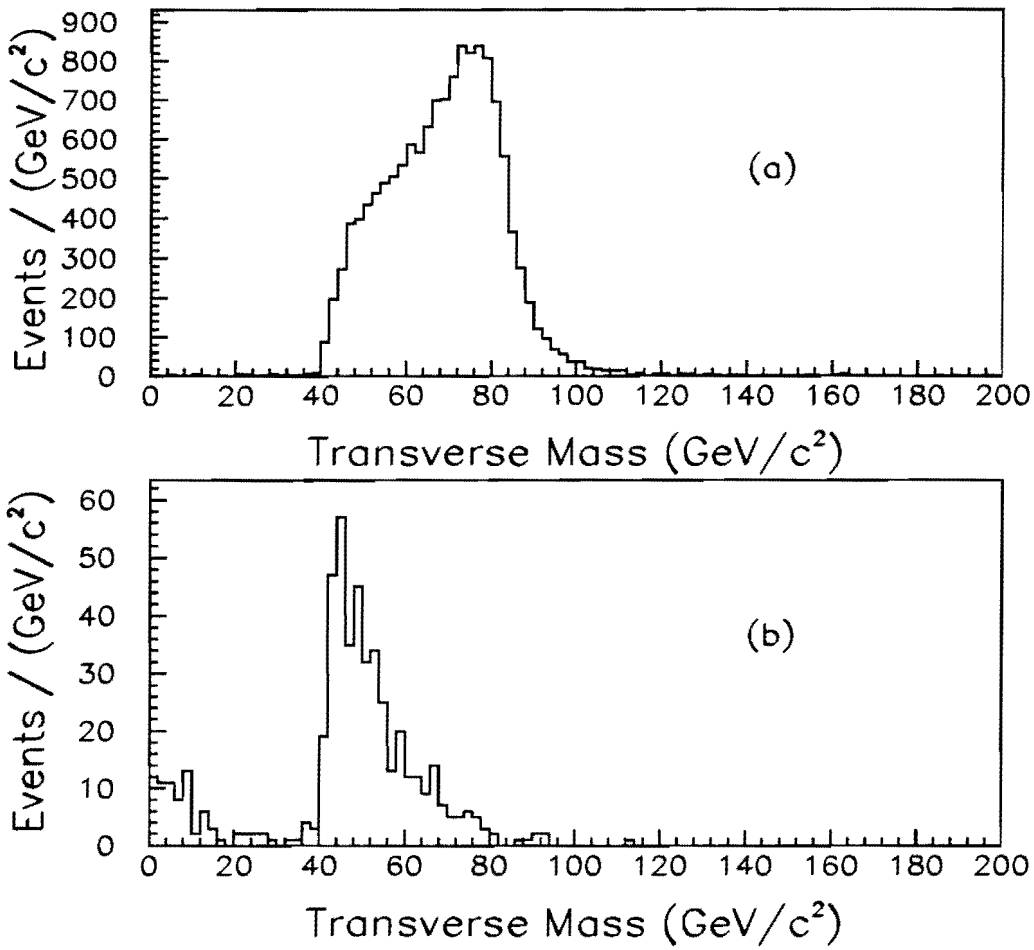

Fig. 3.7: Transverse mass of inclusive electrons with $\not{E}_T > 20$ GeV for (a) isolated electrons ($Iso < 0.1$) and (b) non-isolated ($Iso > 0.3$) electrons. Electrons from $W \rightarrow e\nu$ decays tend to be isolated.

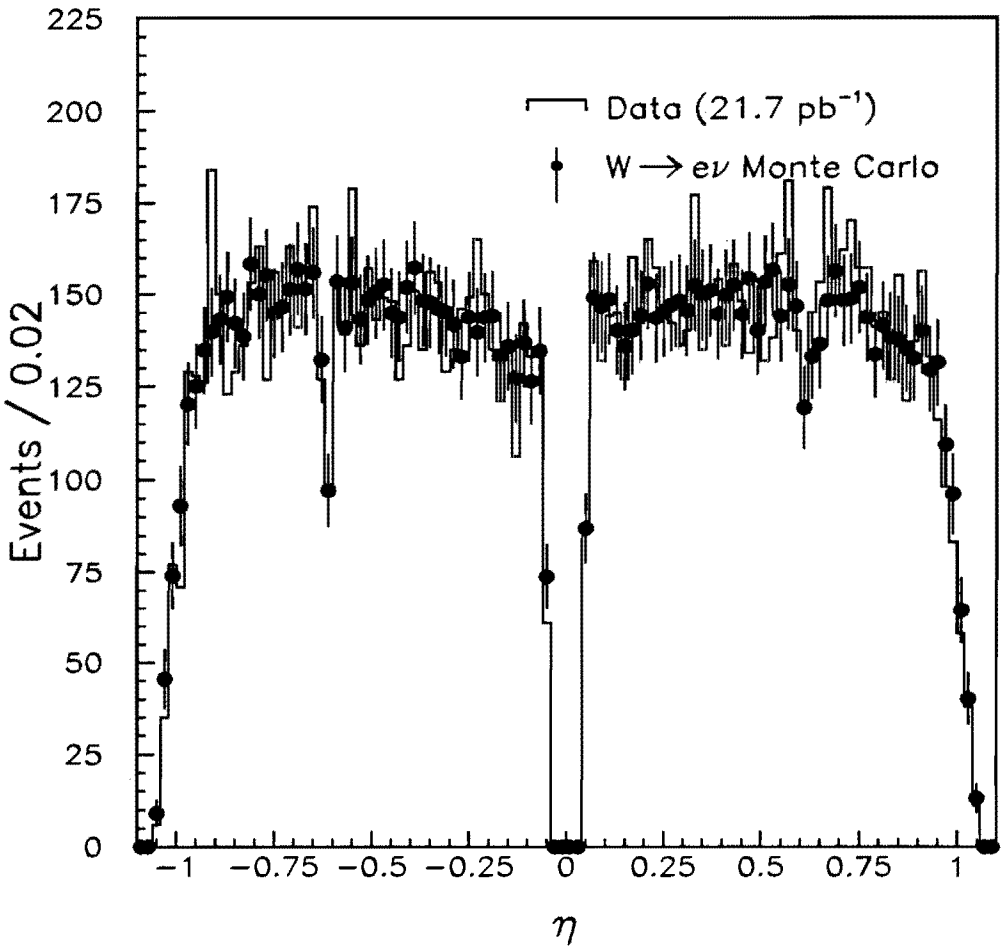

Fig. 3.8: Distribution in η of electrons from $W \rightarrow e\nu$ decays in the data and the Monte Carlo described in Chapter 7. The Monte Carlo has been also folded in with the trigger efficiency from Figure 2.17 and is normalized to the same area as the data.

Chapter 4

Non-W/Z^0 Electron Sample

Electrons from W and Z^0 decay account for only a fraction of the high-P_T inclusive electrons observed in our detector. In this Chapter we investigate the sources of high-P_T electrons from QCD processes that create electrons in embedded in hadron jets. This discussion will be of particular use in the next chapter, in which we discuss the backgrounds to the W candidates. As mentioned in Chapter 3, we anticipate that electrons in hadron jets fall into three categories: 1) electrons which come in e^+e^- pairs, either from photon conversions or Dalitz decays; 2) electrons from heavy quark decay; and 3) hadrons that fake electrons. Hereafter, the electron pairs from photon conversions and Dalitz decays will be referred to collectively as "conversions."

In this chapter we first estimate how many electrons in the inclusive electron sample (see Section 3.1) come from QCD processes like the electrons in the non-W/Z^0 electron sample. We then estimate the fraction, f_b of electrons in hadron jets that originate from heavy quark decay using the 17805 electrons in the non-W/Z^0 electron sample. We also estimate the fraction f_{conv}, of non-W/Z^0 electrons from photon conversions, and the fraction f_{fake}, of non-W/Z^0 electrons that are not electrons but clusters of hadrons.

4.1 Number of Inclusive Electrons from *QCD* Jets

The non-W/Z^0 electron sample is posited to originate from *QCD* processes producing hadron jets. One can ask the simple question of what fraction of events in the overall inclusive electron sample (see Section 3.1) come from such processes. This question is not crucial to what follows, but is interesting. To do so, we manipulate the $\not\!\!E_T$ and electron *Iso* variables. Figure 4.1 characterizes the electrons with $\not\!\!E_T < 10$ *GeV*, the electrons in the non-W/Z^0 control sample. The electrons are opposed by high-P_T hadronic jets. Any $\not\!\!E_T$ in the event, furthermore, appears to arise as a result of mismeasurement of the jets opposite in ϕ to the electron uncorrelated with the electron jet itself.

We assume that the mismeasurement resulting in $\not\!\!E_T$ is uncorrelated with any fluctuations in the electron jet, such as whether or not the electron jet fluctuates to be isolated. Figure 4.2 shows the $\not\!\!E_T$ of inclusive electrons with *Iso* > 0.3, which contains < 0.4% of the electrons from W/Z^0 decays (see Figure 2.4). We use this spectrum to estimate the efficiency of the $\not\!\!E_T < 10$ *GeV* cut used to make the non-W/Z^0 sample for hadron jets. In Figure 4.2, (58 ± 3)% have $\not\!\!E_T < 10$ *GeV*, so that we can scale the 21637 hadron jet events of Section 3.4 up by 1/0.58 to obtain that approximately 37400 ± 1900 of the 50861 inclusive electrons are from hadron jets. The number 21637, it was noted, has a small background from W/Z^0 decay, but this is small for our present purposes and relieves us of having to estimate the efficiency of requiring a 10 *GeV* jet in these *QCD* processes. Larger systematic uncertainties are associated with the *Iso vs.* $\not\!\!E_T$ assumption, as discussed in Chapter 5.

Figure 4.3 shows the E_T spectrum of electrons in the inclusive electron sample, along the spectrum from the non-W/Z^0 electron sample (scaled up to 37400 events), and the Monte Carlo expectation for electrons from W/Z^0 decays (normalized using the number of W and Z^0 events observed). The events at the very highest E_T are mostly dijets, with one Z^0 event. The excess of events above 80 *GeV* is due to the truncation of the sample used to obtain the hadron dijet spectrum: the very highest E_T dijets will have some $\not\!\!E_T$ due to mismeasurement, and the dijet shape used comes from a $\not\!\!E_T < 10$ *GeV* sample.

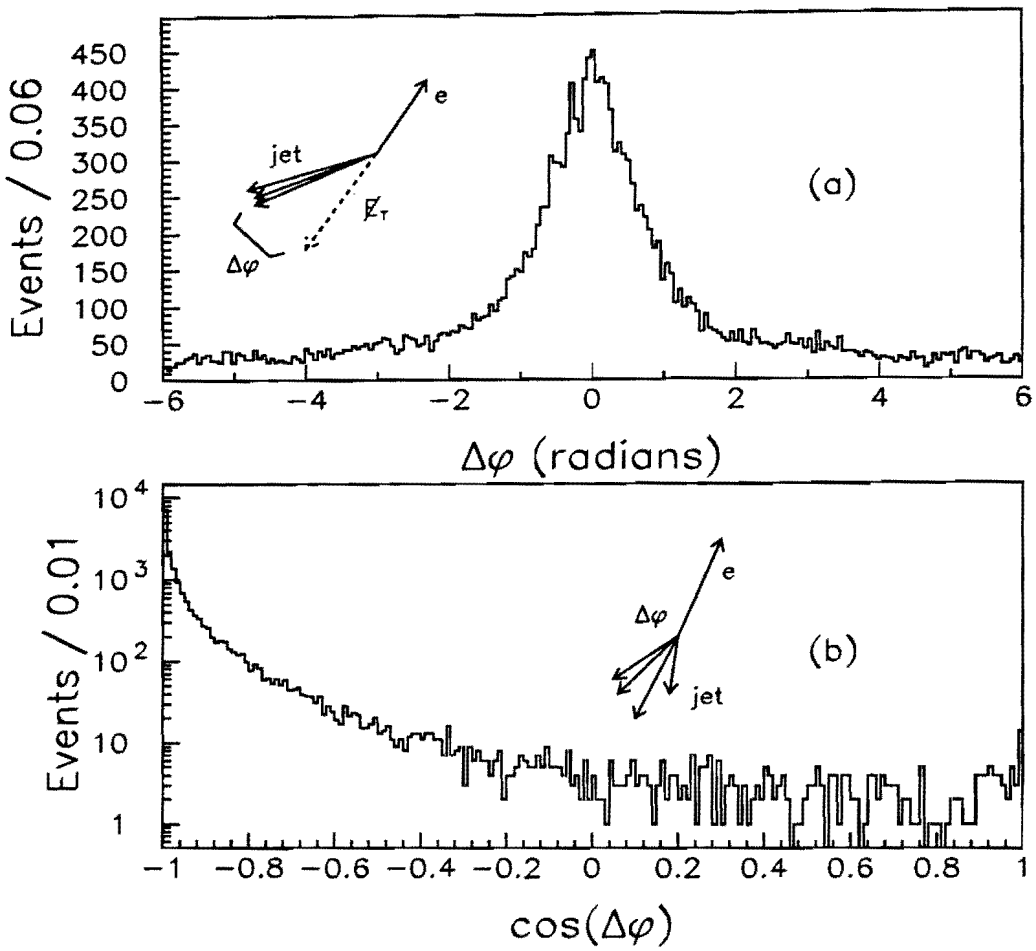

Fig. 4.1 Topology of the events with $E_T < 10$ *GeV*: (a) the $\Delta\phi$ between the $\not{E}_T$ and the largest jet; and (b) the $\cos(\Delta\phi)$ between the electron and largest jet in the event besides the electron.

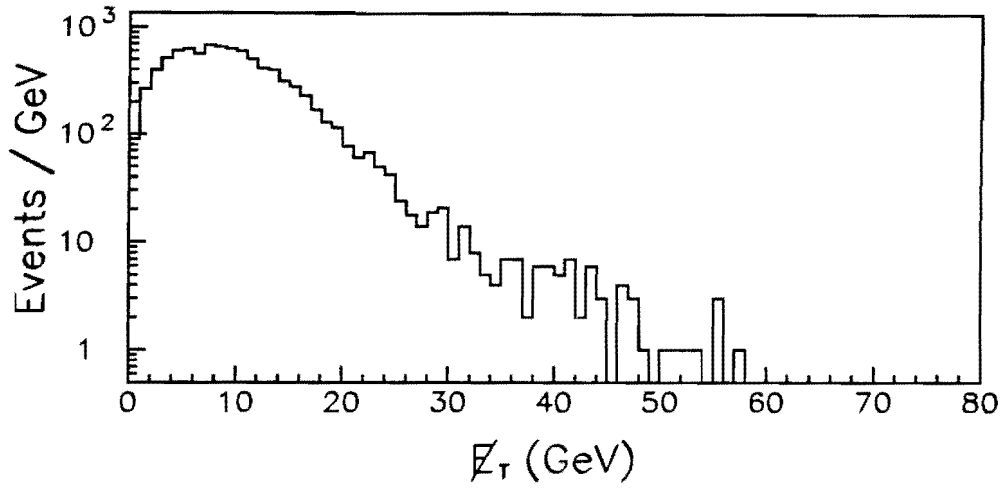

Fig. 4.2: $\not{E}_T$ spectrum of non-isolated ($Iso > 0.3$) inclusive electrons. If Iso and $\not{E}_T$ are uncorrelated (independent fluctuations of opposing jets), this plot indicates that a $\not{E}_T < 10$ GeV cut is 58% efficient for electrons in hadron jets.

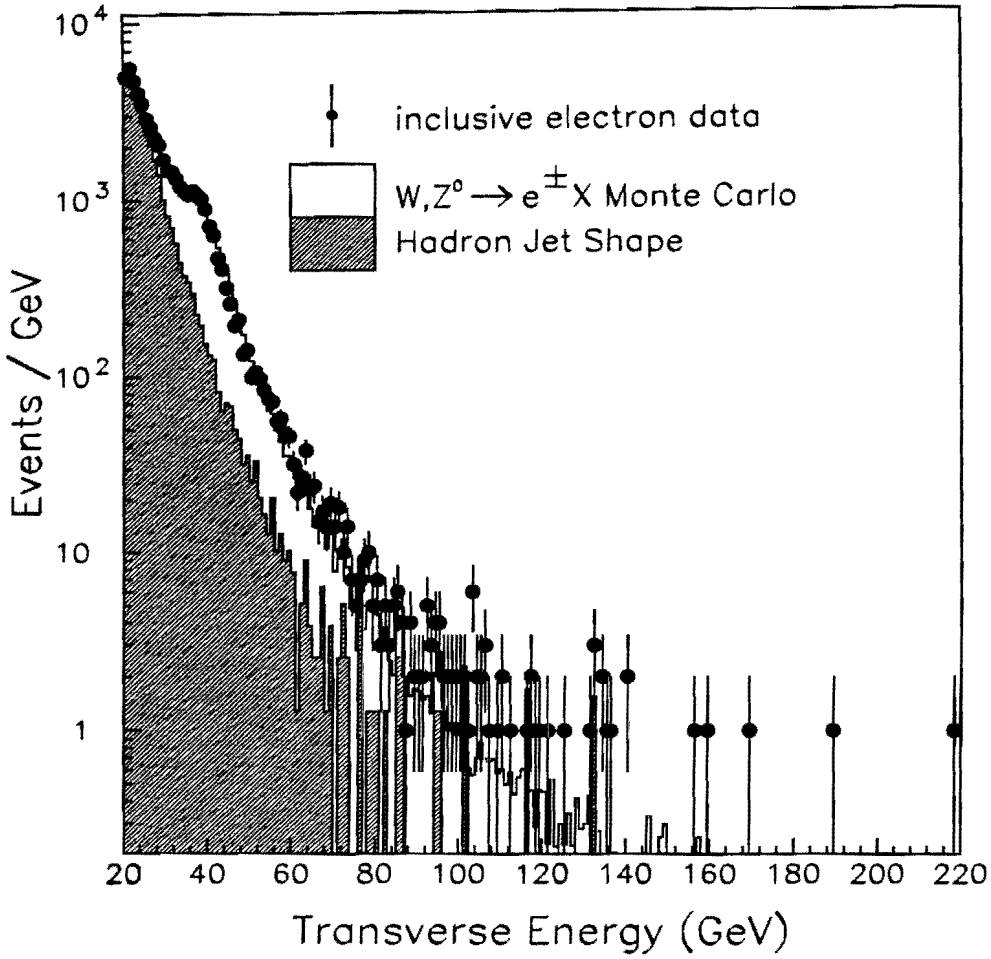

Fig. 4.3: E_T spectrum of inclusive electrons, along with the expected shape for electrons from hadron jets and the expected shape for electrons from W/Z^0 decays. The hadron jet shape comes from the non-W/Z^0 sample, normalized to 37400 events, and the W/Z^0 shape comes from the Monte Carlo described in Chapter 7. The agreement with the expectation is good over the range 20 $GeV < E_T < 80$ GeV. The excess above 80 GeV is discussed in the text.

4.2 Estimate of the Conversion Electron Fraction

4.2.1 Identification of Conversion Electrons

Electrons from photon conversions are identified by searching for a second, oppositely-signed charged track near the electron track which extrapolates to a common tangent point in the CTC. We flag as conversions the electrons which have a second track nearby in the CTC passing the following cuts: $|\delta(r\text{-}\phi)| < 0.2$ *cm*; $|\delta(\cot\theta)| < 0.06$. The first cut is on the separation in the $r\text{-}\phi$ view between the two tracks at their tangent point. This variable is given a positive sign if the two circles of the tracks in the $r\text{-}\phi$ view do not overlap, and a negative sign otherwise. The second cut is on the difference in $\cot\theta$ between the two tracks. With these cuts, 7119 of the 17805 electrons in the non-W/Z^0 sample are flagged as conversions.

4.2.2 Over-efficiency of Conversion Cuts

Some hadron tracks are falsely flagged as a conversion partners by the $\delta(r\text{-}\phi)$ and $\delta(\cot\theta)$ cuts. In this section we estimate the electron purity of the partner tracks selected with the $\delta(r\text{-}\phi)$ and $\delta(\cot\theta)$ cuts by looking at the CES pulse height left by the conversion partner track (see Section 2.4.2).

We select two control samples of conversions. The "Good" conversions are those passing the cuts in Section 4.2.1, and the "Pure" conversions are selected based on the signature of their converting on the outer wall of the VTX (see Figure 4.5). Conversions on the outer VTX wall show no charged track in the VTX. The good and pure conversion sample selection criteria are summarized in Table 4.1.

In Figure 4.6 is shown the quantity CES/p near the partner conversion track for the "Good" conversion sample. Also shown is the expected pulse

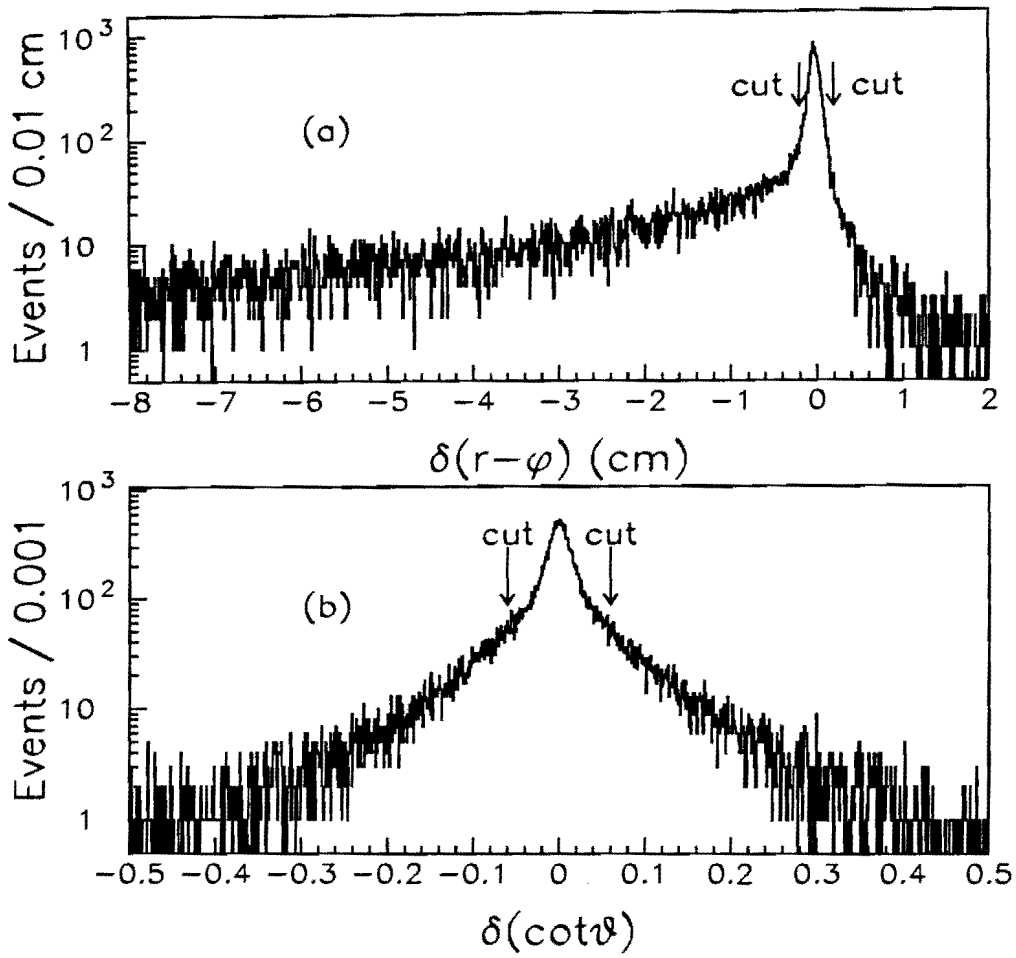

Fig. 4.4: Distributions in the variables for track pairs used to identify photon conversions (see text). One track in the pair is the Central high-P_T electron in events with $E_T < 10$ *GeV*.

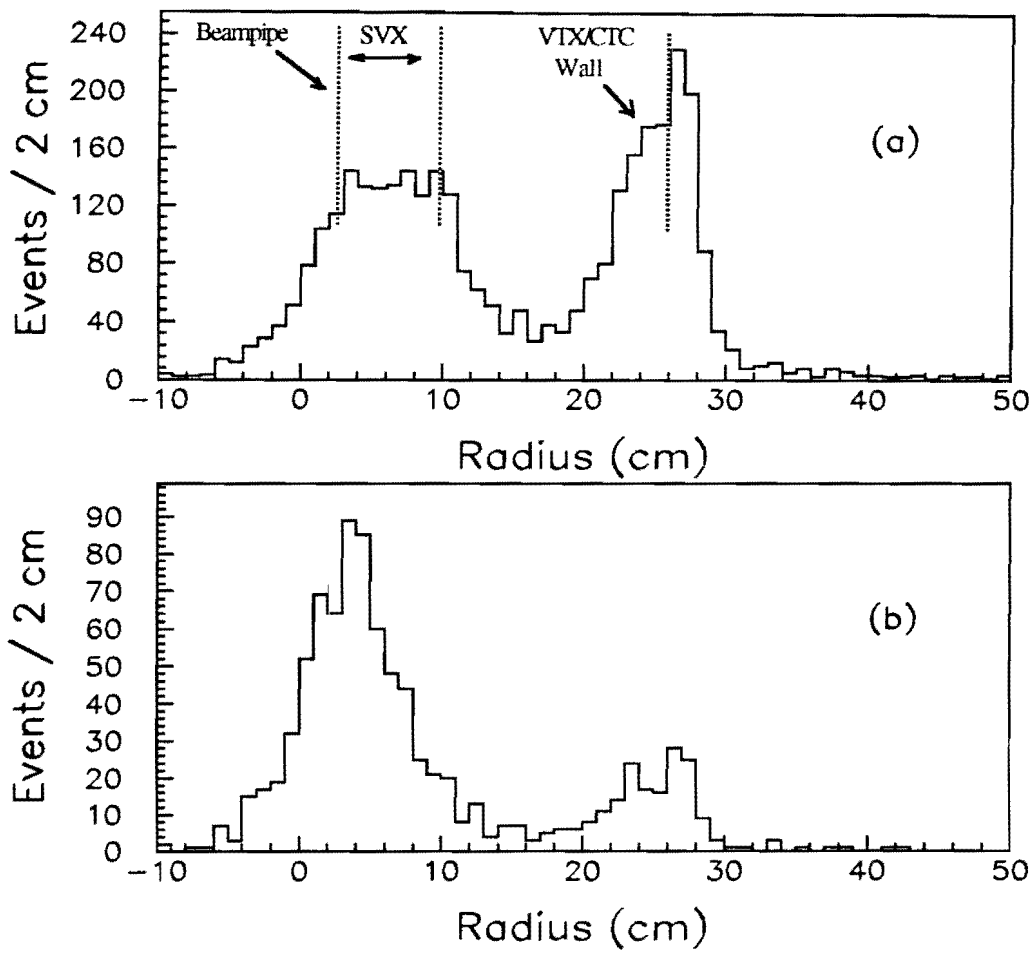

Fig. 4.5: Radius of photon conversions in the "good" conversion sample.. The conversion radius is the r coordinate of the point that the two conversion tracks meet. The peaks correspond to the presence of the beampipe and to cables between the VTX/CTC. The peak near zero is also indicative of the Dalitz decays. Shown is the radius (a) for all conversion pairs, (b) for all conversion pairs that have an SVX track associated with the electron track. The peak at 27 cm in (b) results from accidental hits in the SVX that can create an SVX track even though the charged particle originated outside of the SVX.

Table 4.1: Conversion Pair Control Samples

"Good" Conversions	$\lvert \delta(r\text{-}\phi) \rvert < 0.2$ *cm* $\lvert \delta(\cot\theta) \rvert < 0.06$
"Pure" Conversions	$\lvert \delta(r\text{-}\phi) \rvert < 0.2$ *cm* $\lvert \delta(\cot\theta) \rvert < 0.06$ VTX Occupancy < 0.2 Conversion Radius > 20 *cm*

height shape for real electrons, obtained from the "Pure" conversion sample in Table 4.1. The "Pure sample is normalized to the "Good" conversion sample in the region $CES/p > 4000$ ADC counts/(GeV/c). The non-conversion background, $F_{non\text{-}conv}$, of hadron tracks selected by these cuts is the area in the excess peak near zero pulse height. We find $F_{nonconv} = 11.7 \pm 0.8(stat.) \pm 2.0(sys.)$ %, where the systematic error comes from the possible non-electron background with $CES/p > 4000$ ADC counts/(GeV/c).

4.2.3 Efficiency of Conversion Cuts

We estimate now the efficiency of the conversion cuts. The efficiency has two parts: 1) the efficiency, ε_{trk}, for finding the second CTC track, which is due to the fact that the partner track can be of much lower P_T and may not be reconstructed because it curls up in the magnetic field; 2) the efficiency, ε_{angle}, for the track pair, even if detected, to pass the $\delta\ (r\text{-}\phi)$ and $\delta(\cot\theta)$ cuts.

In order to estimate the first inefficiency, ε_{trk}, we plot in Figure 4.7 the P_T of the partner track in the "Pure" conversion sample from Table 4.1. We fit the distribution to an exponential using bins with $P_T > 1$ GeV/c to determine the number of events absent in the lowest two bins. This functional form is of course not *a priori* correct, but the inefficiency is small enough that we simply take half of itself as the systematic uncertainty. Using the nominal fit parameters tells us that the efficiency of finding the second track is $\varepsilon_{trk} = 91.4 \pm 0.9\ (stat.) \pm 4.0(sys.)$ %.

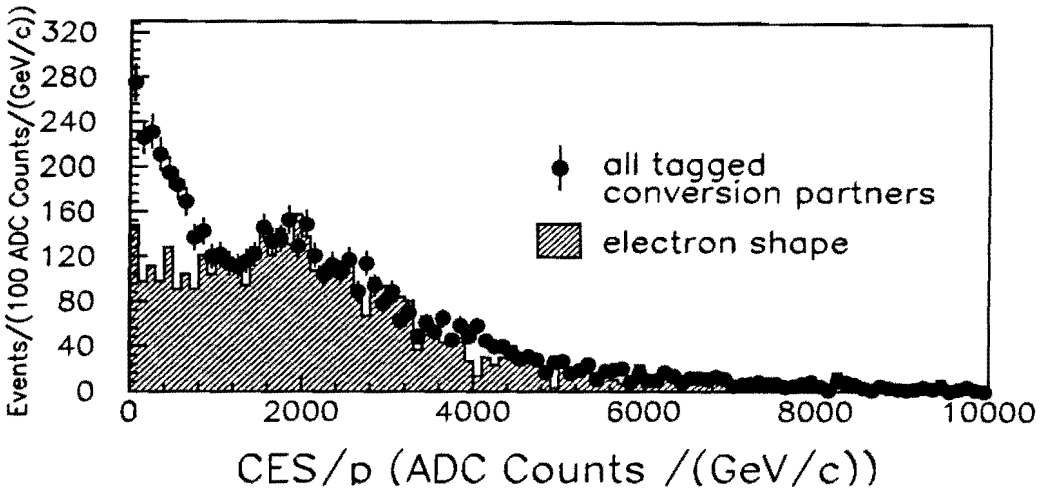

Fig. 4.6: CES pulse height for partner tracks tagged as conversions (the "Good" conversion sample) and the expected shape for real electrons obtained from the "Pure" conversion sample of Table 4.1. The electron shape is normalized to the points in the region greater than 4000 ADC Counts / (*GeV/c*).

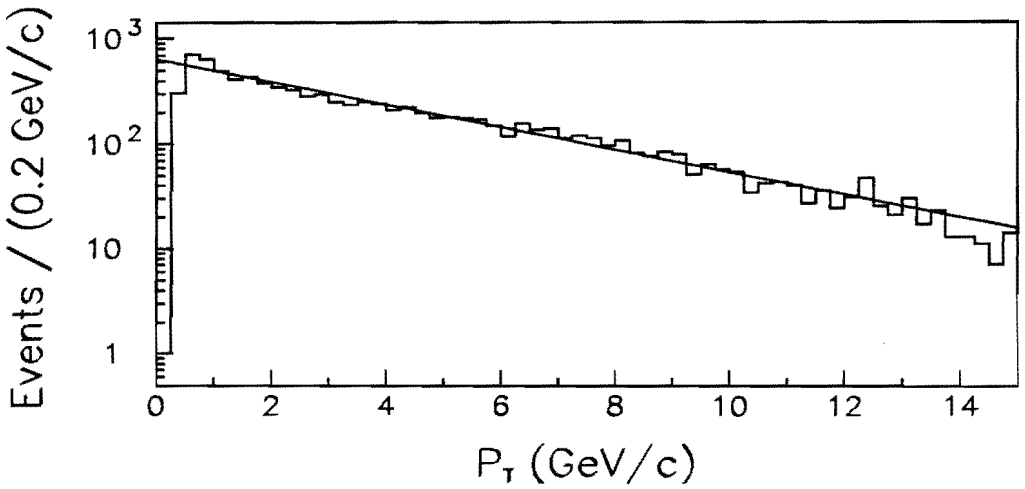

Fig. 4.7: P_T of partner track in conversion electron pairs in the "Pure" conversion sample. The curve is the best fit to an exponential in the region $P_T > 1$ *GeV/c*.

In order to estimate the second efficiency, ε_δ, that of the $\delta(r\text{-}\phi)$ and $\delta(\cot\theta)$ angle cuts, we select conversion partner tracks not using the tracking cuts, but using only the CES pulse height near the partner track. We require greater than 2,000 Strip ADC counts/(GeV/c) near the partner track. From Figure 4.7, we estimate that this sample of electrons should be nearly entirely conversions, with backgrounds less than 1%. In Figure 4.8 we plot $\delta(r\text{-}\phi)$ and $\delta(\cot\theta)$ for these events. No $\delta(r\text{-}\phi)$ and $\delta(\cot\theta)$ cuts have been applied yet. The efficiency of the cuts is $\varepsilon_\delta = 93.1 \pm 0.5$ (*stat.*) $\pm$ 1.2 (*sys.*) %, where the systematic error is due to the possible $\approx$ 1% non-conversion background in the sample of events with > 2,000 Strip ADC counts/(GeV/c) near the partner track.

4.2.4 Estimate of Conversion Electron Fraction

Of the 17805 electrons in our sample of electrons from jets, N_{cand} = 7119 are flagged by the cuts as conversions. We must subtract the background to this estimate and then scale up by the efficiency for the conversion selection criteria. Doing so, we find

$$\begin{aligned}
\text{Number of conversions} &= \frac{1.0 - F_{non\text{-}conv}}{\varepsilon_\delta \times \varepsilon_{trk}} (N_{cand}) \\
&= \frac{1.000 - (0.117 \pm 0.021)}{(0.931 \pm 0.012) \times (0.914 \pm 0.041)} (7119 \text{ events}) \\
&= 7387 \pm 388 \text{ events}
\end{aligned}$$

This comes to a fraction of electrons from hadron jets which are from photon conversions of

$$f_{conv} = \frac{7387 \pm 228 \text{ conversions}}{17805 \text{ events}} = 41.5 \pm 2.2 \ (stat.+sys.)\%.$$

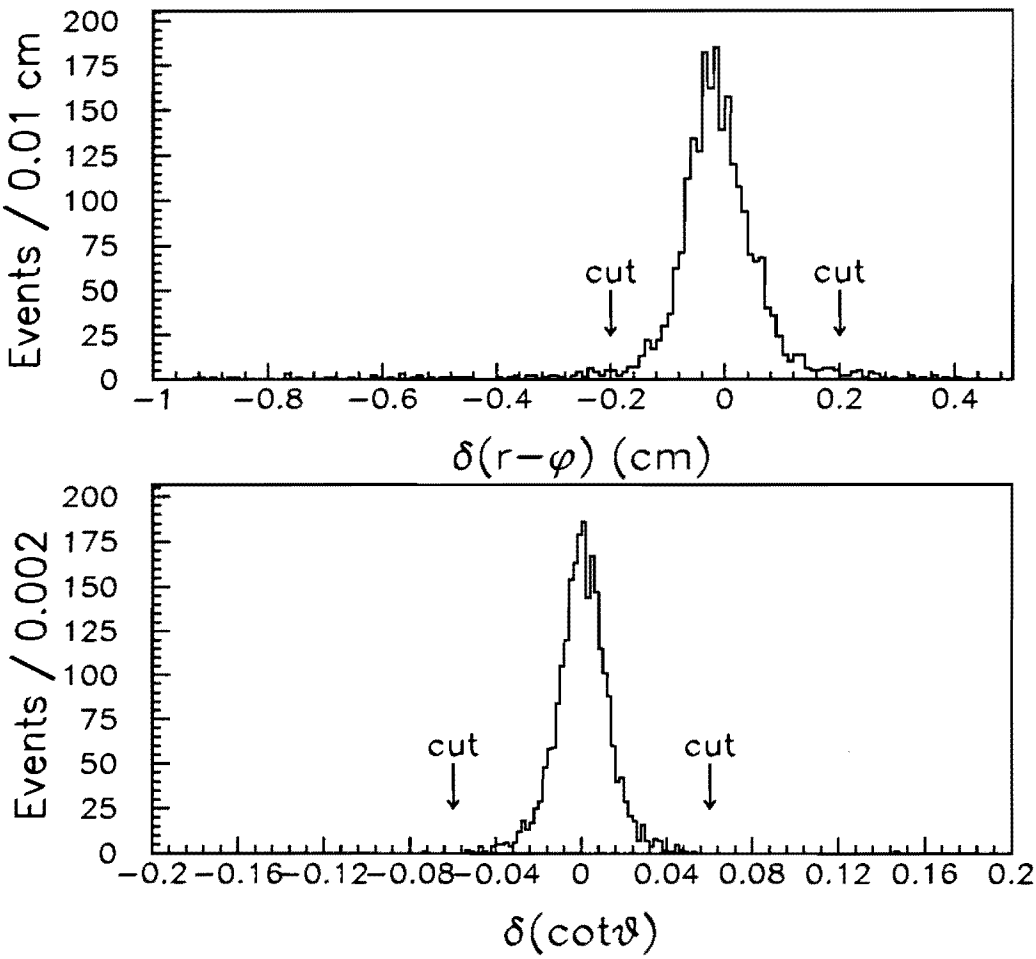

Fig. 4.8: $\delta(r\text{-}\phi)$ and $\delta(\cot\theta)$ for oppositely signed CTC track pairs where the first track is a tight Central electron and the second track has a large pulse height near it in the CES (CES/p > 2000 ADC Counts / GeV/c). The slight offset in $\delta(r\text{-}\phi)$ from zero is due to ≈ 200 μm misalignments in the CTC that are not corrected for in this analysis.

4.3 Estimate of the *b* Electron Fraction

One signature characteristic of a b quark is its long lifetime. Using the impact parameter of electrons in the Silicon Vertex Detector (SVX), an estimate is made of the number of electrons in the non-W/Z^0 sample from b decay. The impact parameter distribution of all electrons in the non-W/Z^0 sample is fit to a sum of shapes from b, conversion, and fake electrons. The impact parameter shape for fake electrons is assumed to the same as that of Z^0 electrons, since they are presumably from light quark jets and have zero lifetime.

The "fit" to the impact parameter distribution uses the number of events in the D/σ tails. We define B_i to be the fraction of events with $|D|/\sigma > 2.0$, where "i" = conversion, b, or hadron fake,. For example, using the Z^0 electrons (a sample of that contain no background) to determine the fake shape gives $B_{fake} = 7.1 \pm 0.7$ % (see Figure 2.10(a)). The D/σ shape for all electrons in the non-W/Z^0 sample is shown in Figure 4.12. For the whole sample we find $B_{all} = 25.9 \pm 0.5$ %. We attribute the excess beyond zero lifetime ($B = 7.1\%$) to be partly due to b's and partly due to conversions. If f_{conv}, f_b, and f_{fake}, are the fractions of conversion, heavy quark, and fake electrons in this sample, The b fraction is determined from the equation:

$$B_{all} = (f_b \cdot B_b) + (f_{conv} \cdot B_{conv}) + (f_{fake} \cdot B_{fake})$$

The fractions B_i will be determined in the following sections and we use the fraction $f_{conv} = 41.5\%$ from Section 4.2.

4.3.1 D/σ Shape of b Electrons

We obtain now the D/σ shape for b electrons. Since b's in $p\overline{p}$ collisions are produced in $b\overline{b}$ pairs, we select a data sample of semileptonically-decaying b quarks by tagging the $\overline{b}$ jet in the event with a b-tagging algorithm.[40]

Selecting b events using only the away jet to identify the b electron applies no bias to the signed impact parameter distribution for b electrons.

In the b-tagging algorithm, a probability is formed per jet that the jet comes from a light quark. Jets with low probability are likely to come from heavy quarks. This probability utilizes the signed impact parameters of the tracks in the jet that go through the SVX, and is the probability that the impact parameters of the tracks are consistent with zero within the resolution of the SVX. The probability distribution for jets in the non-W/Z^0 electron sample is shown in Figure 4.9. Heavy quark jets are identified as those jets with Jet Probability < 0.02. From the flat component under the probability peak in Figure 4.9 backgrounds in this sample from false tags of the away jet are expected to be ≈ 10 %.

In Figure 4.10 we show the distribution of signed impact parameter significance, D/σ, of the electrons with tagged away jets. From this D/σ shape, we obtain $B_b = 39.2 \pm 2.2$ (*stat.*) $\pm$ 0.4 (*sys.*)% after correcting for the non-b jets that are tagged, where the systematic uncertainty comes from correcting the distribution for the non-b background.

4.3.2 D/σ Shape of Conversion Electrons

We take as our control sample of conversion electrons those which pass the $\delta(r\text{-}\phi)$ and $\delta(\cot\theta)$ cuts above and also have $CES/p > 2000$ Strip ADC Counts/(GeV/c) near the partner track. As discussed in Section 4.2, this sample has less than 1% non-conversion background. Figure 4.11 shows the D/σ distribution for conversion electrons with an SVX track. Of these, $B_{conv} = 30.6 \pm 1.6$ (*stat.*) $\pm$ 0.3 (*sys.*)% have $|D|/\sigma > 2$, where the systematic uncertainty comes from the possible 1% non-conversion background.

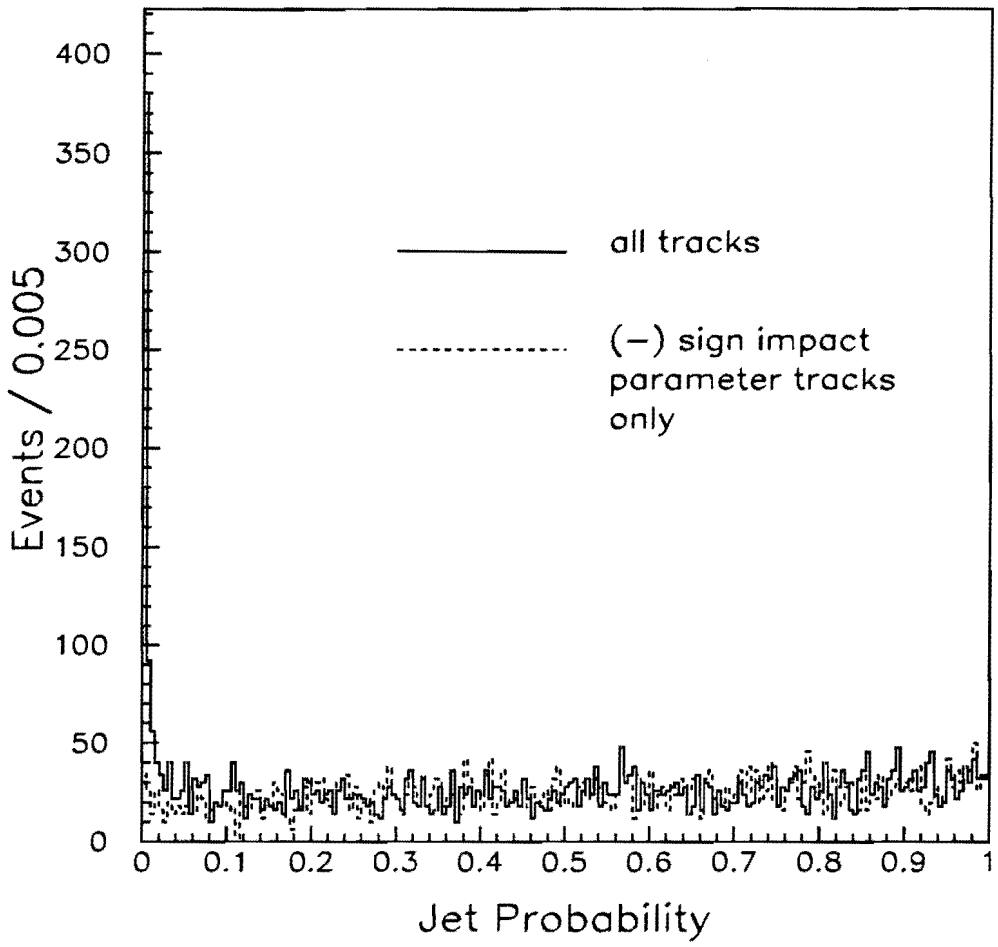

Fig. 4.9: Jet Probability of all jets with at least two SVX tracks in inclusive electron events with $E_T < 10$ *GeV*. The distribution is shown for jets in which all tracks and only negatively-signed impact parameter tracks are incorporated into the jet probability. Since light-quark jets' tracks are equally positively- and negatively- signed, the negatives' jet probability shape is indicative of the shape for light quark jets.

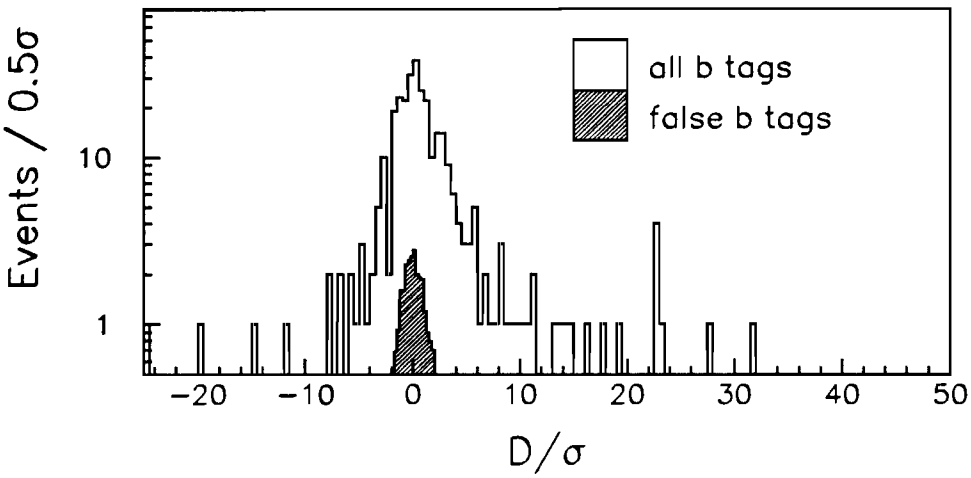

Fig. 4.10: D/σ for electrons in events with a jet tagged as a b jet and $\not{E}_T < 10$ GeV, along with the estimated shape of the false b jet tags (obtained from the Jet Probability > 0.5 region and normalized to 10% of the tagged events).

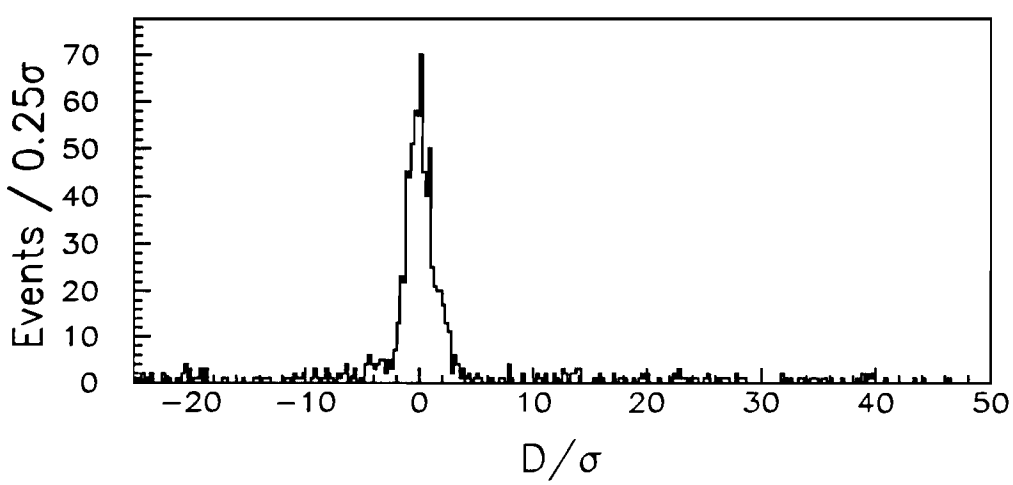

Fig. 4.11: D/σ for conversion electrons. The fact that many electrons from conversion pairs have $D/\sigma \approx 0$ shows that some of the conversion track pairs are probably π^0 Dalitz decays.

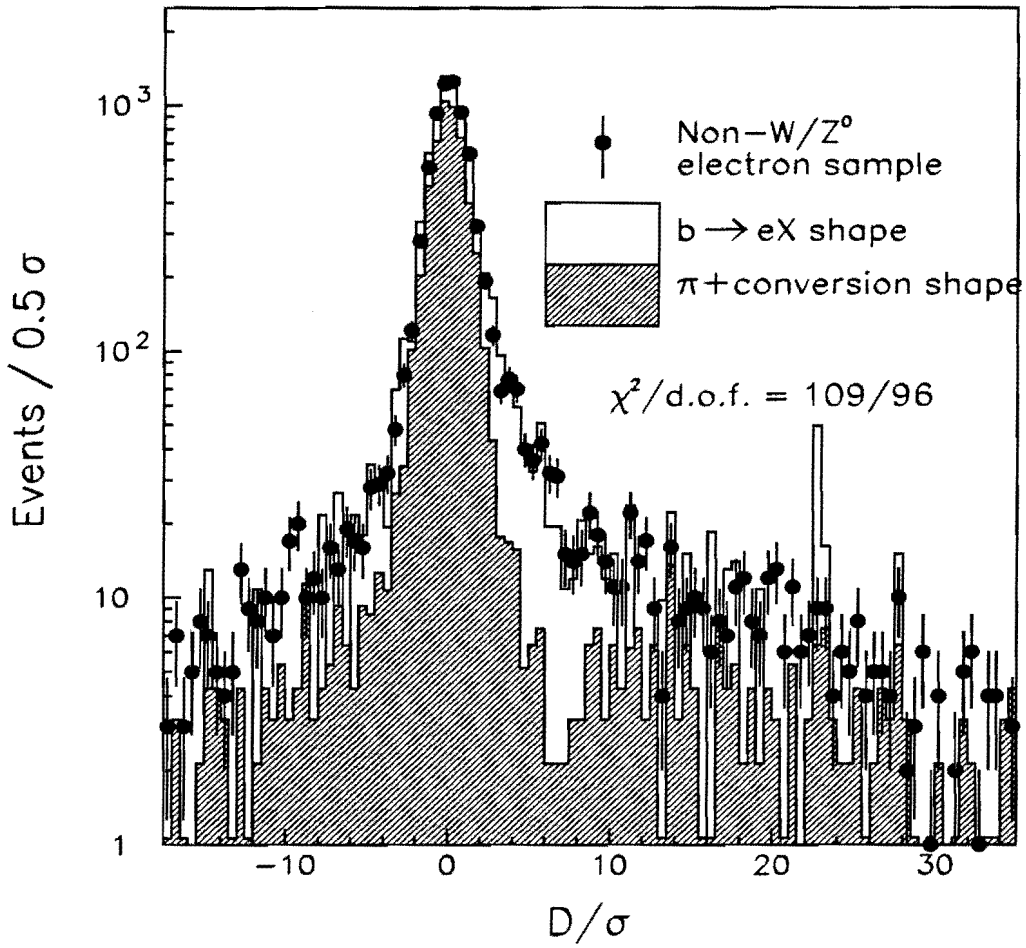

Fig. 4.12: D/σ of all the electrons in the non-W/Z^0 electron sample that have an SVX track, along with the expected shape for bottom electrons and conversions + fake electrons (pions or multihadrons). The shapes are normalized to the expected fractions in the data, as described in the text.

4.3.3 Extraction of b Electron Fraction

Figure 4.12 shows the D/σ distribution for the electrons in the non-W/Z^0 sample that go through the SVX. We fit the amount in the D/σ tails to the sum of b, fake, and conversion shapes, with the conversion fraction fixed. The interested reader is referred to Appendix B for details. We find:

$$f_{conv} = 41.5 \pm 2.2 \ \%$$
$$f_{b's} = 31.5 \pm 3.7 \ \%$$
$$f_{fake} = 27.0 \pm 4.4 \ \%$$

4.4 Estimate of Fake Electron Fraction

This section provides a second, independent estimate of the fraction of the non-W/Z^0 electrons that are fake electrons. The fraction f_{fake} of Section 4.3 is the fraction of the electrons consistent with coming from the primary vertex. Having previously removed prompt electrons from Drell-Yan and W/Z^0 decay, we have interpreted this fraction f_{fake} as representing the fraction of electron clusters which are fakes.

Hadrons should not deposit much charge in the Central Pre-Radiator. Plotted in Figure 4.13 is the CPR charge for all electrons in our non-W/Z^0 sample. Also shown is the CPR shape for electron and hadron tracks. With the conversion electron fraction fixed (see Section 4.2) we find:

$$f_{conv} = 41.5 \pm 2.2 \ \%$$
$$f_b = 31.9 \pm 4.0 \ \%$$
$$f_{fake} = 26.6 \pm 4.1 \ \%$$

The agreement with Section 4.3 is surprisingly good, since the two estimates are independent: in one method the zero lifetime of hadrons is used to differentiate them from heavy quark electrons, and in the other method the longitudinal shower development of electrons and hadrons is used.

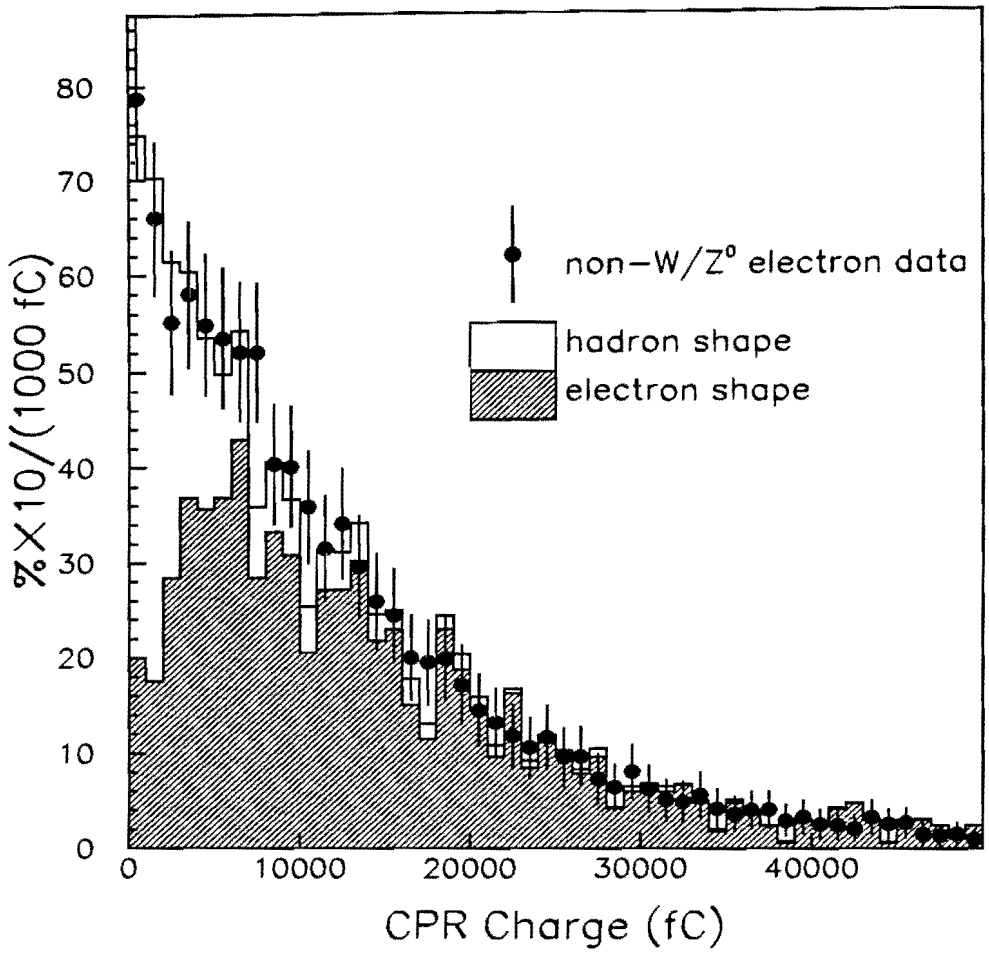

Fig. 4.13: CPR charge for all electron clusters in the non-W/Z^0 sample, along with the expected shape for electrons and for hadrons. The electron shape is obtained from electrons from Z^0 decays and the hadron shape is obtained from high-P_T tracks pointing at jets in W/Z^0 + jet events. The two shapes are normalized to the data using the first 2 bins.

Chapter 5

W Candidate Sample

W candidates are selected with a signature of an isolated electron and $\not\!\!E_T$. This signature, however, can also be mimicked by other physics processes. The signature of $\not\!\!E_T$ is produced by jet mismeasurements and by particles falling into uninstrumented regions of the detector. This Chapter discusses the backgrounds to the W signal from these processes.

5.1 W Candidate Selection

The W candidate selection is described in Section 3.3, but is repeated here. To select W's we require a tight, isolated central electron in the event, where isolation is defined as $Iso \equiv (E_T^{Cone} - E_T^{Cluster})/E_T^{Cluster}$, and in addition we require:

- $\not\!\!E_T > 20\ GeV$
- Event does not posses a second electromagnetic cluster which forms a mass with the first electron in the 66 - 116 GeV/c^2 range

A total of 13796 events have $\not\!\!E_T > 20\ GeV$ and fail our Z^0 cuts. As shown in Figure 3.7, the transverse mass of the isolated electrons shows the characteristic peak, while the non-isolated electrons pile up at threshold.

5.2 Background from Hadron Jets

The physics processes which were described in Chapter 4 can lead to backgrounds to the W signal if the hadron jet containing the electron fluctuates so that the electron is isolated in the calorimeters and if the other jet falls into an uninstrumented region of the detector, creating $\not{E}_T$. The sum of these backgrounds is estimated by extrapolating[41] the Isolation variable for the electron from a region away from the W signal into the W signal region. This method does not identify the individual backgrounds from hadron jets, only the sum of all the hadron jet processes.

5.2.1 Description of the Iso Extrapolation Method

Figure 3.5 shows the manner in which the hadron backgrounds contaminate the signal region. Plotted is the *Iso* of the central electron in a high-P_T electron event *vs.* the $\not{E}_T$ in the event. Within the plot of *Iso vs.* $\not{E}_T$ in Figure 3.5 we identify four regions:

1) Isolation < 0.1 and $\not{E}_T < 10\ GeV$
2) Isolation > 0.3 and $\not{E}_T < 10\ GeV$
3) Isolation > 0.3 and $\not{E}_T > 20\ GeV$
4) Isolation < 0.1 and $\not{E}_T > 20\ GeV$

(Region 4 is the W signal region). We find the W background from the equation:

$$\frac{W \text{ Background}}{\#\text{ Events in Region 3}} = \frac{\#\text{ Events in Region 1}}{\#\text{ Events in Region 2}}$$

The motivation of the method is that electrons from hadron jets ('QCD electrons') generally are produced embedded in a jet of other particles which will cause them to have a higher value of the Isolation variable. If the

fluctuation that caused the electron to be isolated is independent of the fluctuation that caused another jet to be mismeasured, then the variables *Iso* and $\not{E}_T$ are uncorrelated in hadron jet events. These two variables being uncorrelated would imply that the *Iso* shape at low $\not{E}_T$ may be extrapolated upward in $\not{E}_T$ toward the *W* signal region.

5.2.2 Determination of the QCD Iso Shape

In this section we obtain an estimate of the QCD electron *Iso* shape. This shape will later be normalized to the number of events in Region 3 of the *Iso*-$\not{E}_T$ plane to give the *W* background. The QCD electron *Iso* shape will come from the $\not{E}_T < 10$ *GeV* electrons (the non-W/Z^0 sample), for which in Chapter 3 it was noted that the residual contamination from electrons from "electroweak" processes is less than 1%.

Figure 5.2 shows the *Iso* shape of all electrons with $\not{E}_T < 10$ *GeV*. In principle we could use this shape directly to tell us the ratio, *r*, of the number of QCD electrons with *Iso* < 0.1 (in Region 1) to the number with *Iso* > 0.3 (in Region 2). In practice this is not directly possible because the Isolation of the electron on the one side of these events is highly correlated with the magnitude of the jet E_T on the other side of the event, as is shown in Figure 5.1. This effect is a problem, since in the case of the dijet events which fake a *W*, we do not know the E_T of the mismeasured jet opposing the electron. To get around the problem of this correlation, we average the QCD ($\not{E}_T < 10$ *GeV*) sample's *Iso* shape for subsets with different opposing jet E_T's. We select electrons from two control samples to determine the *Iso* shape:

Control Sample 1: Events with a Jet > 10 *GeV* and EM fraction < 0.8
Control Sample 2: Events with a Jet > 20 *GeV* and EM fraction < 0.8
(both have $\not{E}_T < 10$ *GeV*)

The Isolation distributions for the Control Samples and for the $\not{E}_T > 20$ *GeV* sample are shown in Figure 5.2. Control Sample 1 has 17805

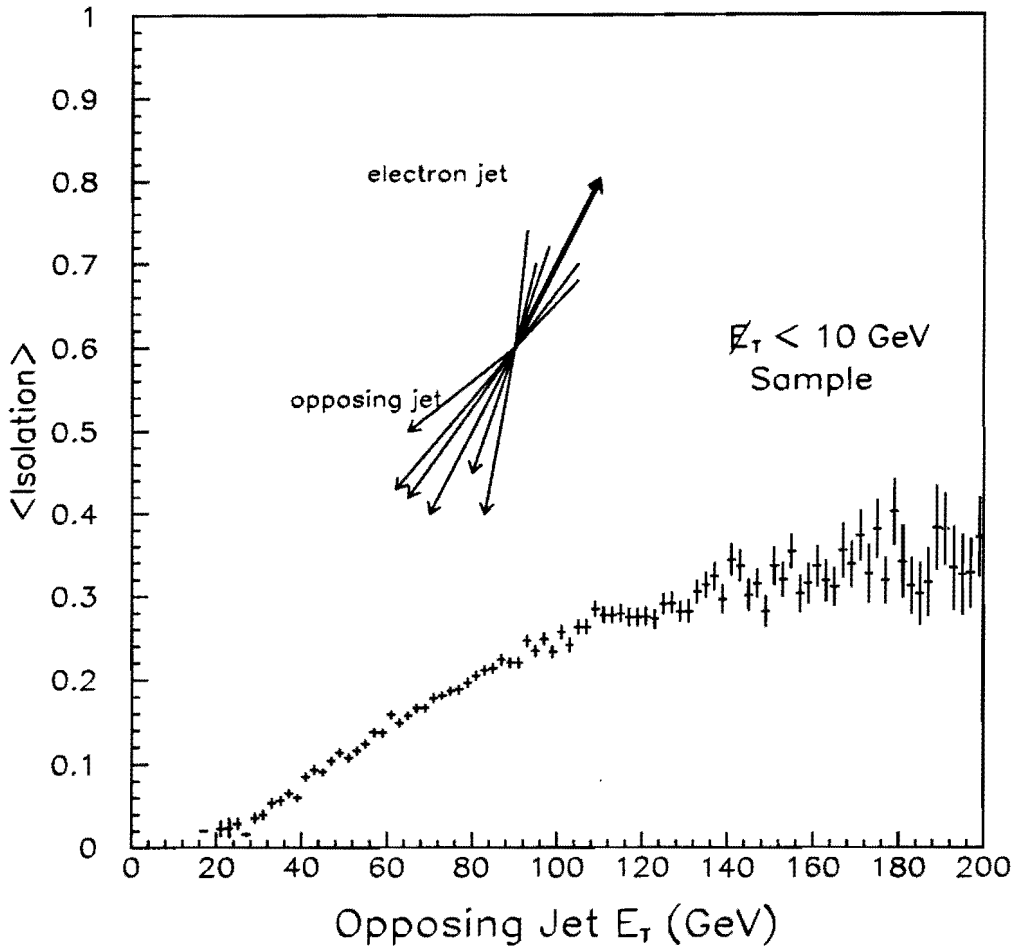

Fig. 5.1: Mean electron *Iso vs.* E_T of the opposing jet in the $\not{E}_T < 10$ *GeV* region. As the jet opposing the electron jet stiffens, momentum balance requires the particles in the electron jet to stiffen, and they are thus less likely to be bent out of the *Iso* cone by the magnetic field.

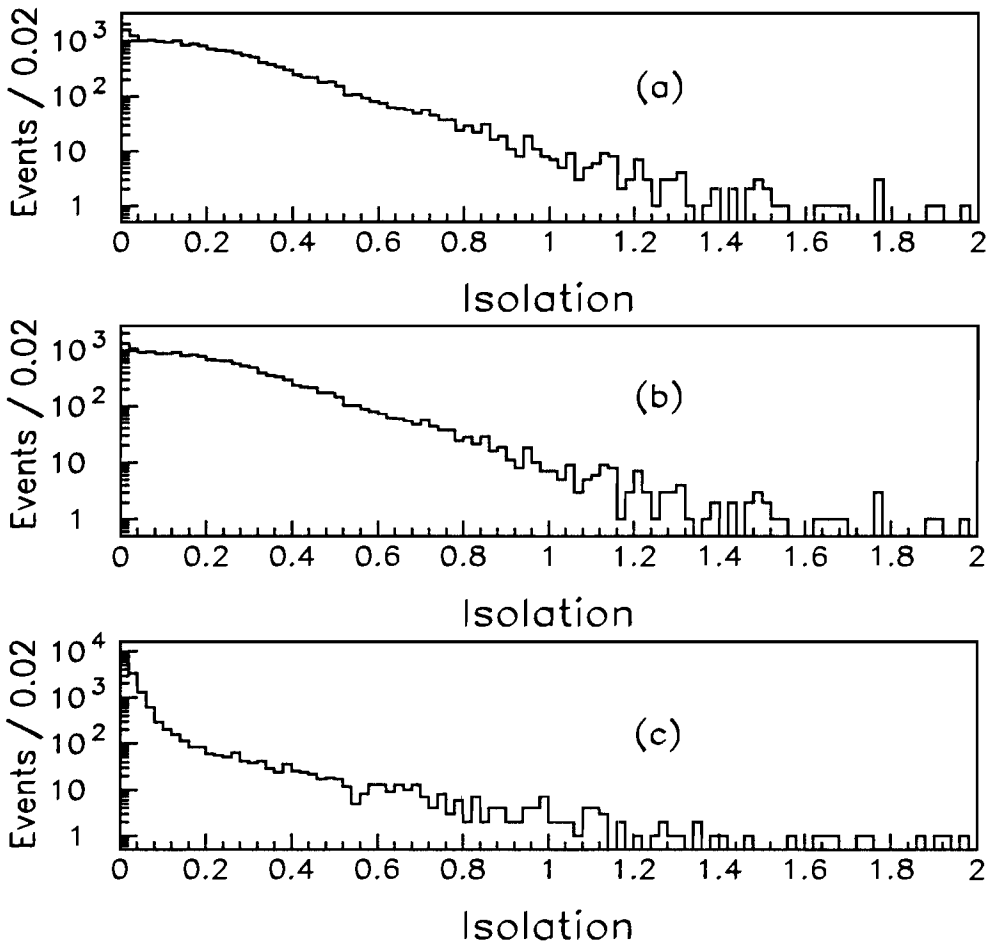

Fig. 5.2: *Iso* of the central electron in two subsets of the $E_T < 10$ *GeV* sample and for the $E_T > 20$ *GeV* sample: (a) Control Sample 1, (b) Control Sample 2, and (c) the $E_T > 20$ *GeV* sample.

events and Control Sample 2 has 16541 events. Control Sample 2 is a subset of Control Sample 1. The control samples give:

$$\text{Control Sample 1: } r \equiv \frac{\#\ \text{Events in Region 1}}{\#\ \text{Events in Region 2}} = 1.5$$
$$\text{Control Sample 2: } r \equiv \frac{\#\ \text{Events in Region 1}}{\#\ \text{Events in Region 2}} = 2.0$$

We take the average of these two results to be $<r> = 1.8 \pm 0.3$ to account for the systematic difference between the two samples .

We must justify the fact that we can extrapolate the Isolation distribution up to higher values of E_T. We break up the *Iso vs.* E_T plot in Figure 3.5 into bins of E_T. Figure 5.3 shows the mean Isolation from of the electron as a function of the E_T bin from Figure 3.5. At 20 - 30 *GeV* in E_T, one can clearly see the *W* signal changes the mean Isolation, but at lower E_T, the mean *Iso* is roughly flat *vs.* E_T. We take this flatness to mean that the QCD *Iso* shape may be extrapolated upwards in E_T.

5.2.3 Determination of Background:

There are 499 events in Region 3. The *Iso* method for determining the background gives (for a $E_T > 20$ *GeV* cut):

$$\begin{aligned} W\ \text{Background} &= <r> \cdot 499 \\ &= (1.8 \pm 0.3) \cdot 499 \\ &= 898 \pm 155 \text{ events.} \end{aligned}$$

Given the 13796 *W* candidates with $E_T > 20$ *GeV* and *Iso* < 0.1, this is a 6.5% background contribution from electrons from hadron jets.

Note in Figure 5.4 the E_T shape of the events in Region 3. This shape suggests that most of the W background piles up at the threshold of our E_T cut.

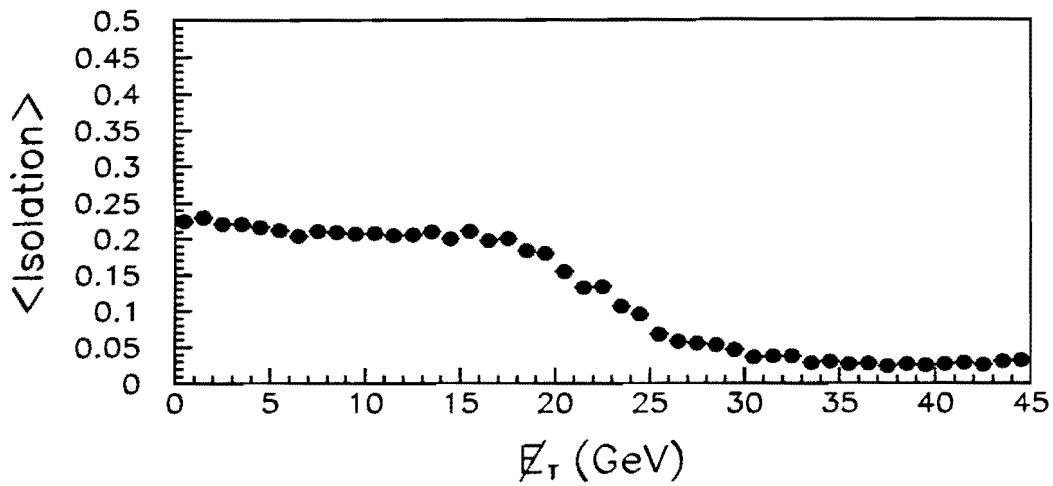

Fig. 5.3: Mean electron *Iso vs.* $\not{E}_T$ in the event.

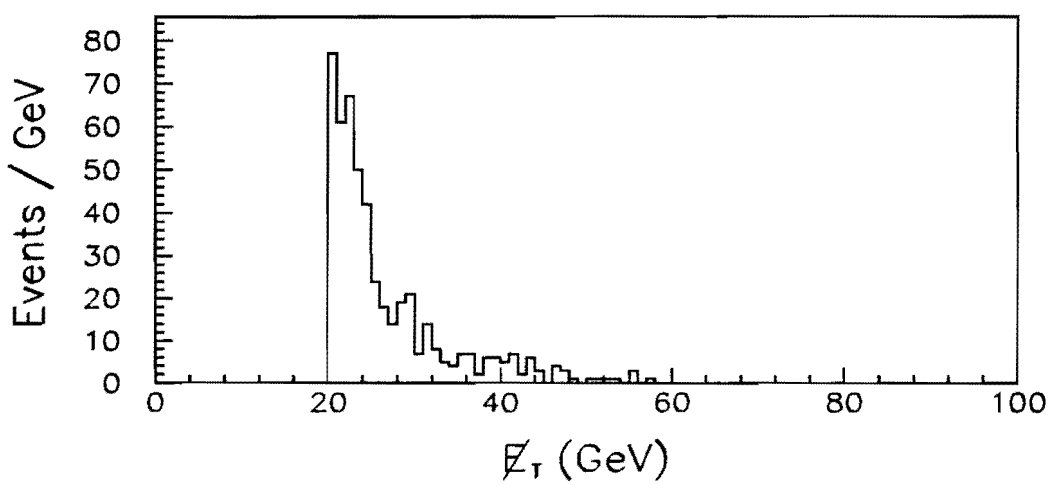

Fig. 5.4: $\not{E}_T$ of electrons with $Iso > 0.3$, $\not{E}_T > 20$ GeV, indicating that most W backgrounds from hadron jets lie in the 20 - 30 GeV range of $\not{E}_T$.

If we place a cut of $\not{E}_T > 25\ GeV$, the total background would be (for a $\not{E}_T > 25\ GeV$ cut):

$$\begin{aligned} W\,\text{Background} &= (1.80 \pm 0.3) \cdot 115 \\ &= 207 \pm 40 \text{ events.} \end{aligned}$$

This estimate would be skewed if W events had $Iso > 0.3$ and hence populated Region 3. Figure 3.7 shows the transverse mass of the electron+$\not{E}_T$ events in Regions 3 and 4. The events in Region 4 (the W signal region) have the characteristic peak at 80 GeV/c^2 expected for W's. The events in Region 3 show no clear transverse mass peak. From looking at the Iso of Z^0 electrons, we believe this $Iso > 0.3$ probability for W electrons to be $< 0.1\%$. This systematic bias is small compared to other systematic errors that go into the estimate.

5.3 Cross-Check of Hadron Jet Background

The Iso extrapolation method estimates the sum background from all hadron jet sources. We check the Iso extrapolation method by estimating the background from the individual backgrounds separately, namely the backgrounds from photon conversions, from b decay, and from fake electrons from hadron showers. Because of limited statistics, we estimate the QCD contamination to the $\not{E}_T > 20\ GeV$ region with the Iso cut removed. To further determine how much of this goes into the $Iso < 0.1$ region requires more statistics than is now available.

The Iso vs. $\not{E}_T$ method may also be used to determine the QCD background to the $\not{E}_T > 20\ GeV$ (any Iso) region. Instead of using the $\not{E}_T < 10\ GeV$ sample to determine the ratio $r \equiv (Iso < 0.1)/(Iso > 0.3)$, we use the QCD electrons to determine another ratio,

$$R \equiv \frac{\text{any } Iso \text{ and } \not{E}_T < 10\ GeV}{Iso > 0.3 \text{ and } \not{E}_T < 10\ GeV}$$

This ratio, averaging over the two Control Samples 1 and 2, is $<R> = 4.2 \pm 0.7$, and so the *Iso vs.* $\not{E}_T$ method predicts that the QCD contamination in the $\not{E}_T > 20$ *GeV* (any *Iso*) region is:

$$\text{QCD Contamination} = <R> \cdot (499 \text{ events}) = 2100 \pm 350$$

We compare this total number of events to the sum of the individual hadronic processes below.

5.3.1 Background from Conversion Electrons

We estimate now the conversion contamination of the $\not{E}_T > 20$ *GeV* (any *Iso*) region. We identify conversions by searching for the partner track to the electron using the $\delta(r\text{-}\phi)$ and $\delta(\cot\theta)$ cuts from Chapter 4. The efficiency of these cuts for real conversions is 85.1 ± 4.4 %.

We observe 1023 events with $\not{E}_T > 20$ *GeV* that are flagged as conversions. The $\not{E}_T$ spectrum of these events is shown in Figure 5.5. It is evident that many of these events pile up at the $\not{E}_T$ cut threshold. There is also a cluster of events at 40 *GeV*, suggesting that the cuts falsely identify some *W*'s as conversions.

The over-efficiency of the conversion cuts when acting on *W* electrons is studied using electrons from $Z^0 \rightarrow e^+e^-$ decays. Applying the conversion cuts to the first leg of the Z^0's, we find that 1.8 ± 0.5 % of the Z^0 electrons are flagged as conversions. Multiplying by the 13796 *W* candidates, we expect 248 ± 55 false conversion tags of *W* events. This overefficiency is also shown in Figure 5.5. Scaling up by the conversion-finding efficiency, the true number of conversions in the $\not{E}_T > 20$ *GeV* (any *Iso*) region is [(1023 tags) - (248 ± 55 false tags)]/0.851 = $(775 \pm 64)/0.851$ = 910 90 events.

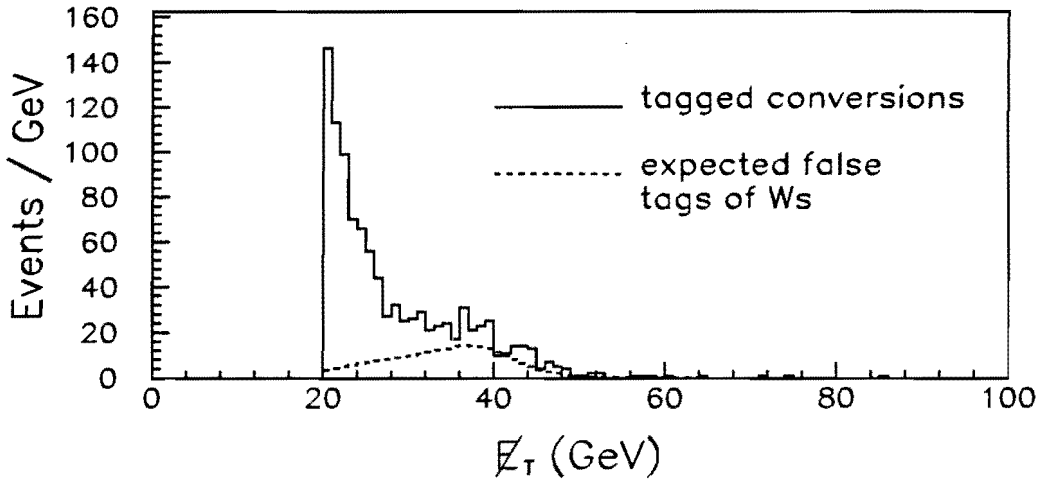

Fig. 5.5 E_T for events with electrons tagged as conversions with $E_T > 20$ *GeV*, along with the expected E_T shape for *W* events, where the *W* electron event is falsely tagged as a conversion. No *Iso* cut is placed on the electron. The *W* shape comes from the Monte Carlo described in Chapter 7 and is normalized to the number of *W* candidates times the conversion false tag rate (obtained from the Z^0's).

5.3.2 Background from Heavy Quark Decay

To estimate the contamination to the $E_T > 20$ GeV region from b electrons we employ the impact parameter method described in Chapter 4. In Figure 5.6(a) is plotted the signed impact parameter significance for the electrons with $E_T > 20$ GeV that go through the SVX. The population in the tails is $B = 9.2 \pm 0.3$ %, greater than that for the Z^0's (see Chapter 4). From the known impact parameter resolution obtained in the Z^0's, this says that there is an excess population in the tails of 9.2 - 7.1 = 2.1 ± 0.8 %. Using the expected populations, B_i, of b's, conversions, and W's in the tails of impact parameter significance, we obtain $f_b = 5.6 \pm 2.2$ % for the $E_T > 20$ GeV sample. This is 850 ± 360 events with $E_T > 20$ GeV from heavy quark decays.

In Figure 5.6(b), we show the E_T distribution of the electrons with $D/\sigma > 2$. There is a bump at 40 GeV, which indicates that some W electrons have a large impact parameter significance, simply due to resolution effects. Superimposed is the expected E_T curve for W electrons, normalized to 7.1% of the W events (the resolution expected from the Z^0's). The histogram shows that some of the events in the D/σ tails pile up at the threshold of the E_T cut, inconsistent with W production.

5.3.3 Background from Fake Electrons

In Chapter 4, we used the CPR charge near the electron track to distinguish hadron fakes (hadrons which shower early and thus fake an electron) from real electrons. In Figure 5.7 we show the CPR charge for the electrons in which there is $E_T > 20$ GeV in the event (with the *Iso* cut removed). Also shown is the expected shape for good electrons (which is obtained from the Z^0's) and for hadrons (which is obtained from tracks which point to jets). The CPR shape shows that there are 580 ± 370 of the 15229 events with $E_T > 20$ GeV are really hadron fakes.

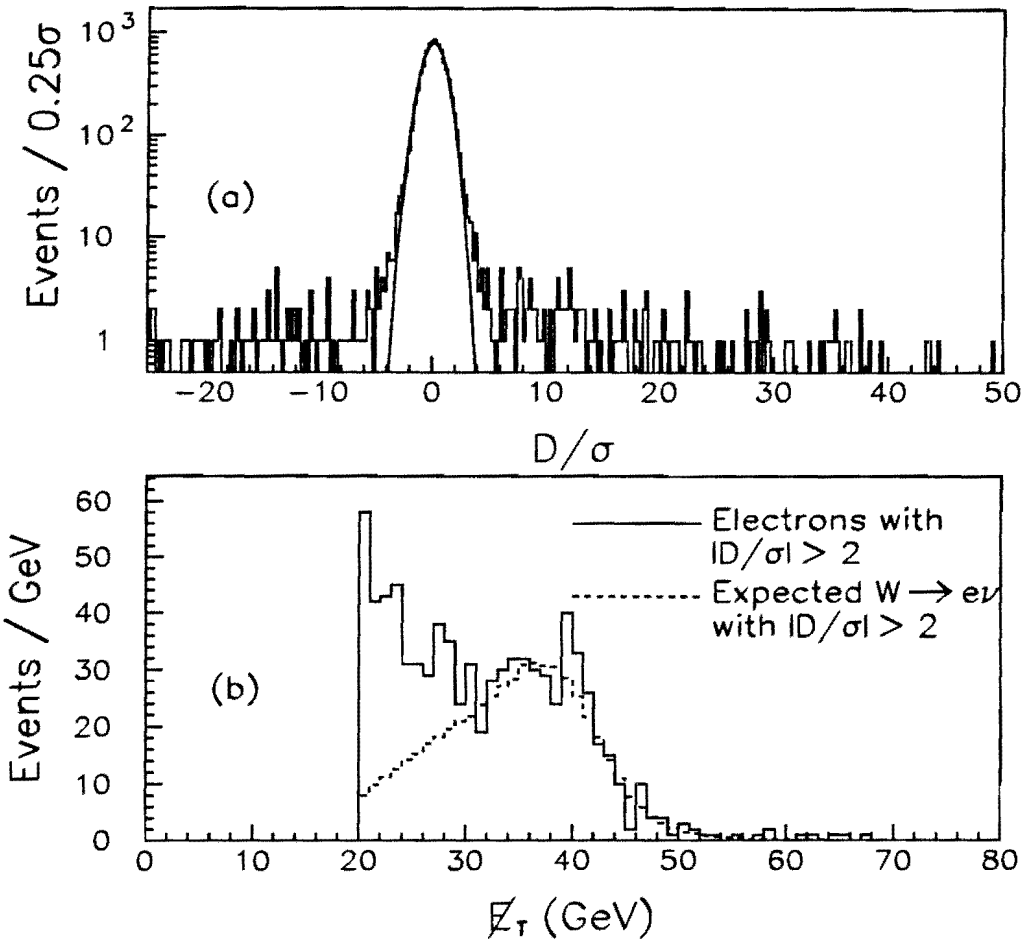

Fig. 5.6 (a): D/σ of electrons in the $E_T > 20$ GeV sample. The gaussian fit is to the data in the range $-2 < D/\sigma < 2$.
(b): E_T (solid histogram) of events with $E_T > 20$ GeV in which the electron has $D/\sigma > 2$, along with the E_T shape for W's (dashed histogram). The W shape is normalized to the number of W candidates times 7.1%.

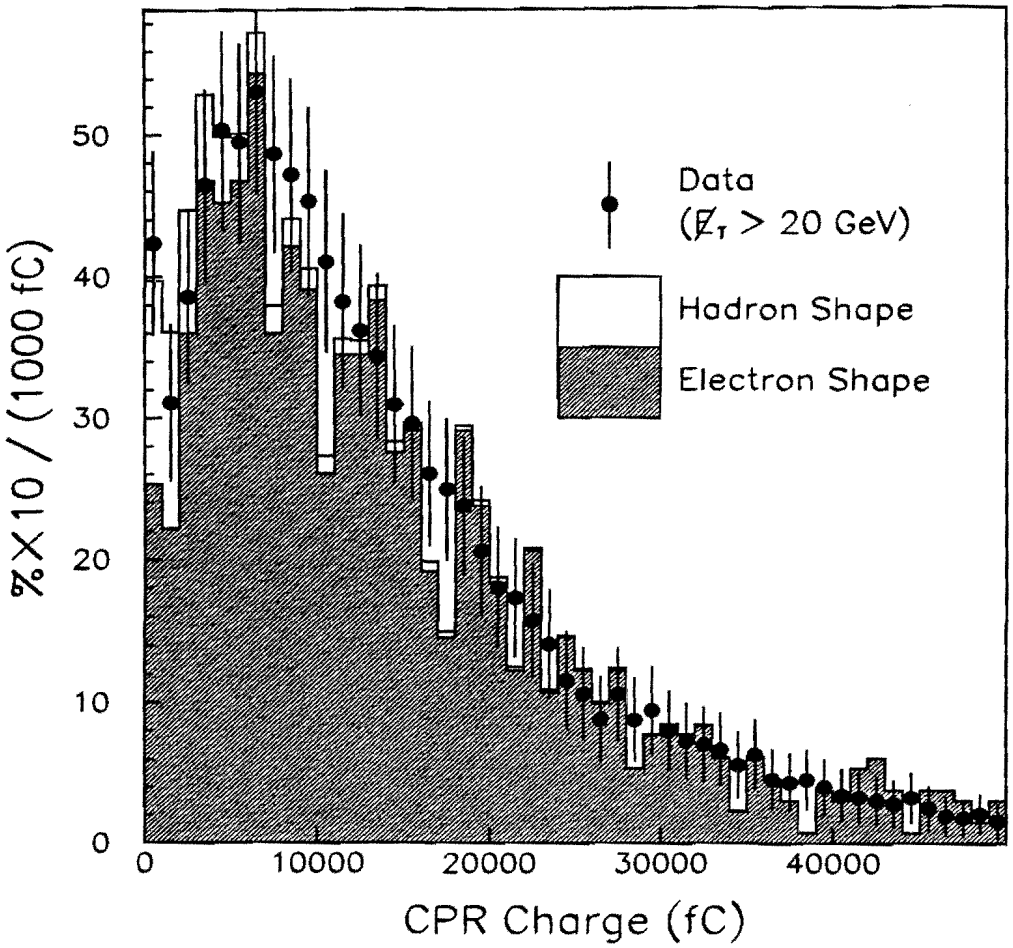

Fig. 5.7: CPR charge of $\not{E}_T > 20$ GeV electrons (points with errors), along with the expected shape of electrons (shaded histogram) and the shape for hadrons (unshaded histogram). The electron and hadron shape are normalized using the first two bins.

5.3.4. Summary of Iso Extrapolation Cross Check

We have used the *Iso* extrapolation to estimate that the total QCD electron contamination in the region of $\not{E}_T > 20\ GeV$ (any *Iso*) is 2100 ± 350 events. Using the conversion filter, we estimate that there are 910 ± 90 conversions in this region. Using the impact parameter of the electron, we estimate that there are 850 ± 360 *b* electrons contaminating this region. Finally, we estimate that 580 ± 370 hadron fakes contaminate the region. If we add these three individual estimates, we obtain 2340 ± 530 QCD events contaminating the $\not{E}_T > 20\ GeV$ (any *Iso*) region, which compares well to the 2100 ± 350 obtained using the Isolation extrapolation. This agreement lends further credibility to the *Iso* extrapolation used to determine the hadron jet background to the *W*'s.

5.4 Background from $Z^0 \rightarrow e^+e^-$

The process $Z^0 \rightarrow e^+e^-$ can fake the *W* signal if one electron falls within the central region and the second electron is lost because it travels to an uninstrumented region of the detector, producing $\not{E}_T$. We use the ISAJET Monte Carlo and a detector simulation to determine the fraction of $Z^0 \rightarrow e^+e^-$ decays that mimic the *W* signature. We find that the fraction is 6.2%. We normalize this fraction to the measured[42] cross section times branching ratio $\sigma \cdot B(p\bar{p} \rightarrow Z^0 \rightarrow e^+e^-)$ at $\sqrt{s} = 1800\ GeV$. The systematic error in this estimate is taken to be 10% error from the cross section plus 10% error from the luminosity. An additional 5% uncertainty is added because ISAJET produces a P_T spectrum of the Z^0's that is slightly harder than that observed in our data: 56% of the ISAJET Z^0's have $P_T(Z^0) > 10\ GeV/c$, while only 44% do in our data. A non-zero P_T is required for one but not both of the electrons from a Z^0 to be lost, so the incorrect shape can overestimate the background. We take the background to the *W*'s from the process $Z^0 \rightarrow e^+e^-$ to be 281 ± 42 events.

5.5 Cross-Check of Background from $Z^0 \rightarrow e^+e^-$

The ISAJET Monte Carlo and a detector simulation are used to determine several of the backgrounds, its performance is checked using $Z^0 \rightarrow e^+e^-$ decays. In the central region, the second electron in $Z^0 \rightarrow e^+e^-$ decays is typically not observed in the calorimeter because it goes through a ϕ crack or the $\theta = 90°$ crack or the chimney module. While its cluster is not observed in the calorimeter, its charged track may still be detected in the Central Tracking Chamber. ISAJET studies indicate that 29% of the Z^0's that fake W's would be detectable as having a charged track with $P_T > 10$ GeV/c, even though the calorimeter cluster is not observed. This is 81 ± 12 Z^0 events that should be observable in the W sample in the data.

In our W sample, Figure 5.8 shows the invariant mass of the tight central electron and the highest P_T track with $P_T > 10$ GeV/c. Approximately 3800 events are observed to have such a track. Figure 5.8 shows variables that are used to select stiff tracks from $Z^0 \rightarrow e^+e^-$ decays. The "track isolation" is defined as the sum P_T in a cone around the second track divided by the second track's P_T. The invariant mass of the 904 events passing these cuts is shown in Figure 5.8. In 213 events, there is at least 20 GeV of E_T. Figures 5.10(a) and 5.10(b) show that events with $E_T > 20$ GeV tend to have the second track point to a crack and that the E_T is often near the second track. In 83 of the 213 events, no second electron cluster is observed, and this compares well to the 81 ± 12 events predicted by ISAJET. Figure 5.11 compares the invariant mass spectrum of the all tight electron plus track Z^0 candidates observed in the data and predicted spectrum from ISAJET.

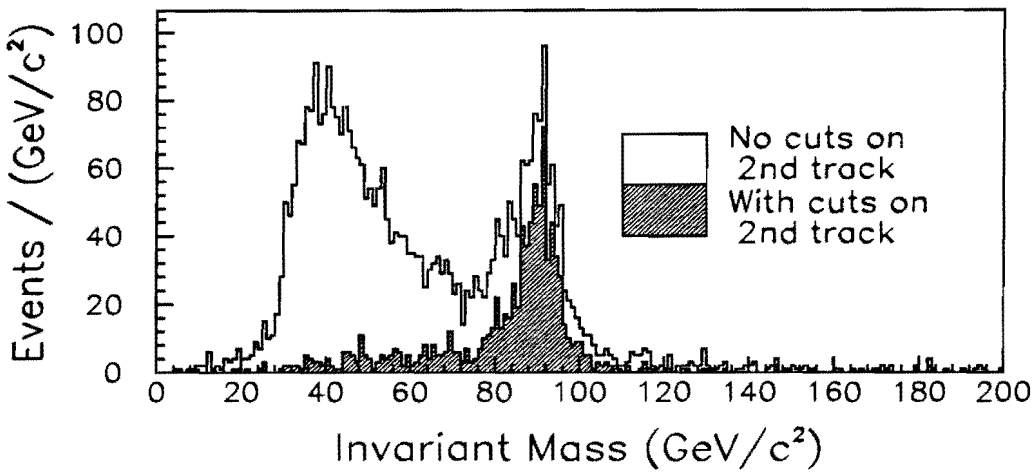

Fig. 5.8: Invariant mass of the tight central electron and the second stiff track, both with and without the cuts on the second track shown in Figure 5.9.

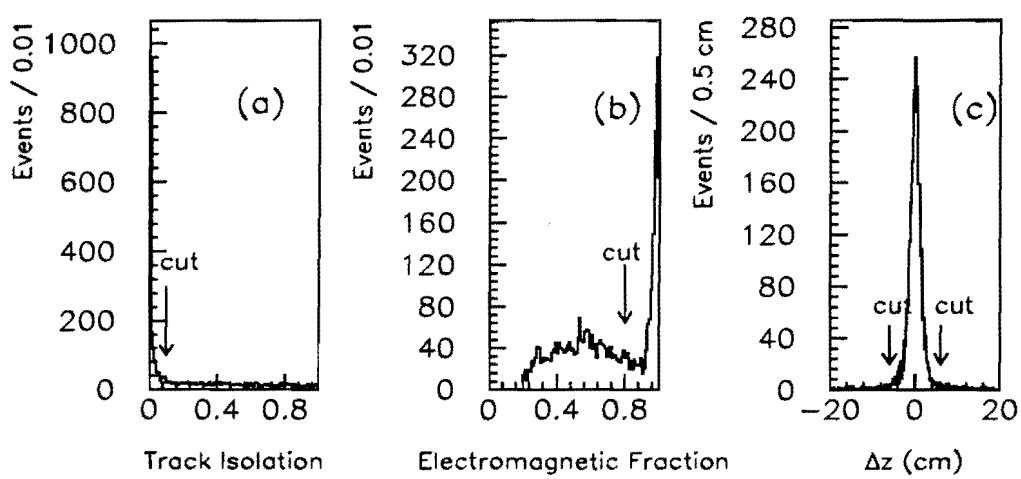

Fig. 5.9: Z^0 selection variables when only a second, oppositely-signed CTC track with $P_T > 10$ GeV/c is required to identify the second electron: (a) the "track isolation;" (b) the electromagnetic fraction of the calorimeter cluster (if observed) near the track; (c) the separation, Δz, between the electron track and the second stiff track at the beamline.

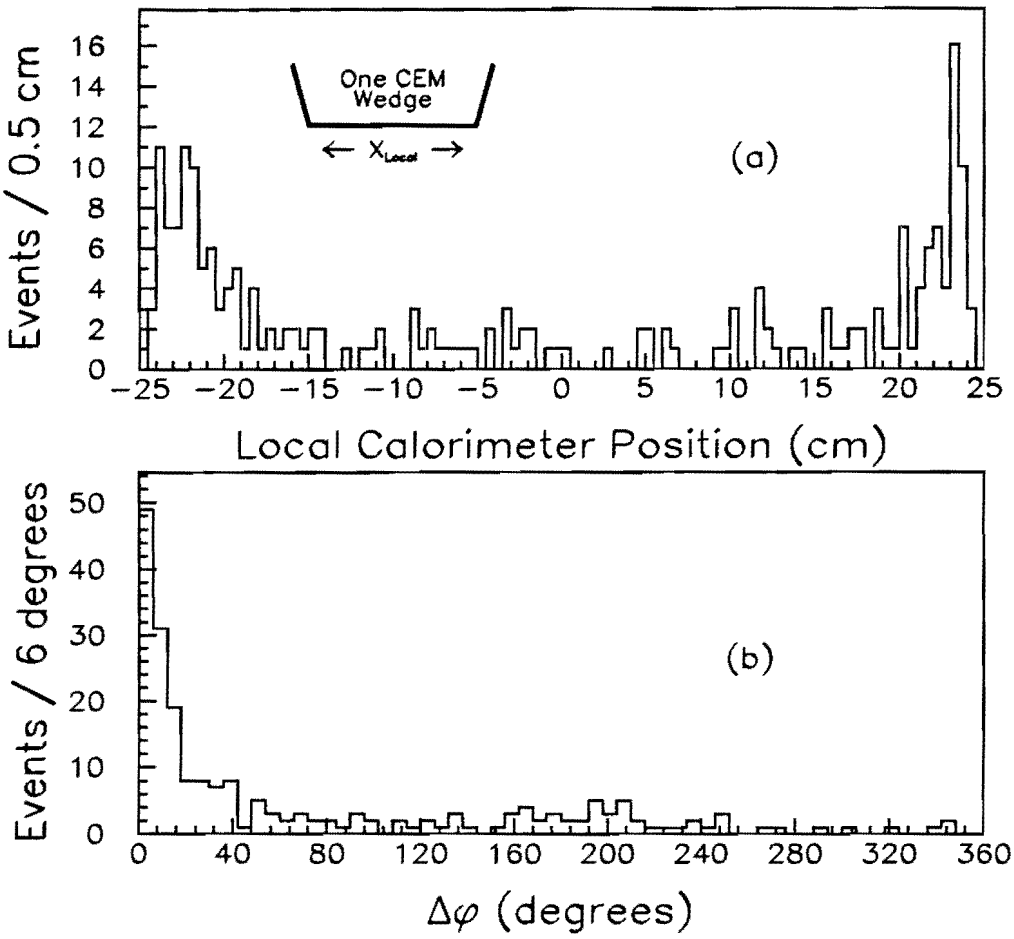

Fig. 5.10 Variables for $Z^0 \rightarrow e^+e^-$ decays when the second electron is unobserved in the calorimeters and only the second track is observed:
(a): calorimeter position, x_{local}, of the extrapolated second track.
(b): $\Delta\phi$ between the second track and the E_T in the event.

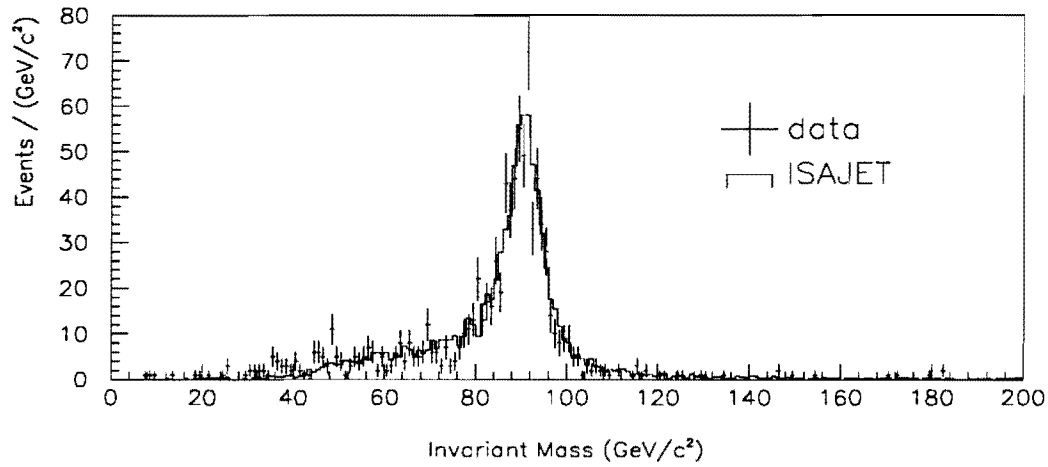

Fig. 5.11: Invariant mass of $Z^0 \rightarrow e^+e^-$ decays when the second electron is selected using only the second CTC track in both the data and ISAJET Monte Carlo.

5.6 Background from $Z^0 \rightarrow \tau^+\tau^-$

The process $Z^0 \rightarrow \tau^+\tau^-$ can mimic the W signature if one τ decays to an electron. Using ISAJET and a detector simulation to determine the fraction of $Z^0 \rightarrow \tau^+\tau^-$ events for which pass the W cuts, and normalizing to the measured Z^0 cross section, we find the background from this process to be 48 $\pm$ 7 events.

5.7 Background from $W \rightarrow \tau\nu$

The process of real W bosons decaying to τ's, where the τ then decays leptonically to an electron, can also produce a high P_T electron in the central region with large $\not{E}_T$. We use ISAJET estimate the acceptance for this process to get into our signal, where fraction of generated $W \rightarrow \tau\nu$ events that pass our W cuts. We also use ISAJET to determine the $W \rightarrow e\nu$ acceptance. We then define the ratio

$$R(e/\tau) = \frac{W \rightarrow e\nu \text{ Acceptance from ISAJET}}{W \rightarrow \tau\nu \text{ Acceptance from ISAJET}} .$$

and use the equations

$$\begin{aligned} \#\ W \rightarrow e\nu \text{ candidates} &= (\#\text{ real } W \rightarrow e\nu\text{'s}) + (\#\ W \rightarrow \tau\nu \text{ background}) \\ &\quad + (\text{other } W \rightarrow e\nu \text{ background}) \\ (\#\ W \rightarrow \tau\nu \text{ background}) &= (\#\text{ real } W \rightarrow e\nu\text{'s}) \,/\, R(e/\tau) \end{aligned}$$

From ISAJET, we find that $R(e/\tau) = 26.6 \pm 1.4$, where the uncertainty is from the τ branching ratio and the 5% error for the ISAJET P_T spectrum. If we subtract all other backgrounds from the W candidates, we have that

$$W \rightarrow \tau\nu \text{ background} = \frac{(12569 \pm 77)}{R(e/\tau)} = 472 \pm 29.$$

The effect of this method is to minimize the uncertainty from the luminosity and the previously measured W cross section.

5.8 Background from Heavy Top Quark

The background of real W's produced from a heavy top quark is considered. Direct searches[43] for the top quark have to date shown no evidence for its existence. We take this background to be 0, but with an error given by the number of events expected for a 120 GeV/c^2 top, which is the 68% confidence level limit on its mass. Using ISAJET, we find the expected background is 0^{+52}_{-0} events. While a 120 GeV/c^2 top would contribute 52 events background, a 150 GeV/c^2 top quark would lead to an expected background of 19 events and a 175 GeV/c^2 top quark would lead to 9 events background.

5.9 Summary of W Signal, Backgrounds.

In Figures 5.12, 5.13, and 5.14 we plot the electron E_T, the neutrino $\not{E}_T$, and the transverse mass of the W candidates, along with the background estimates and the expectations of the Monte Carlo described in Chapter 7. The agreement of the shapes of all of these distributions gives further confidence in the background estimates presented here. Note that, among these three distributions, the electron E_T shows the poorest agreement with the Monte Carlo since it is sensitive to the boson P_T input to the Monte Carlo. The $\not{E}_T$ is in principle sensitive to the boson P_T as well, but the neutrino resolution is poor enough that the shape mismatch less noticeable. The transverse mass distribution is insensitive to the boson P_T and hence is well-modeled.

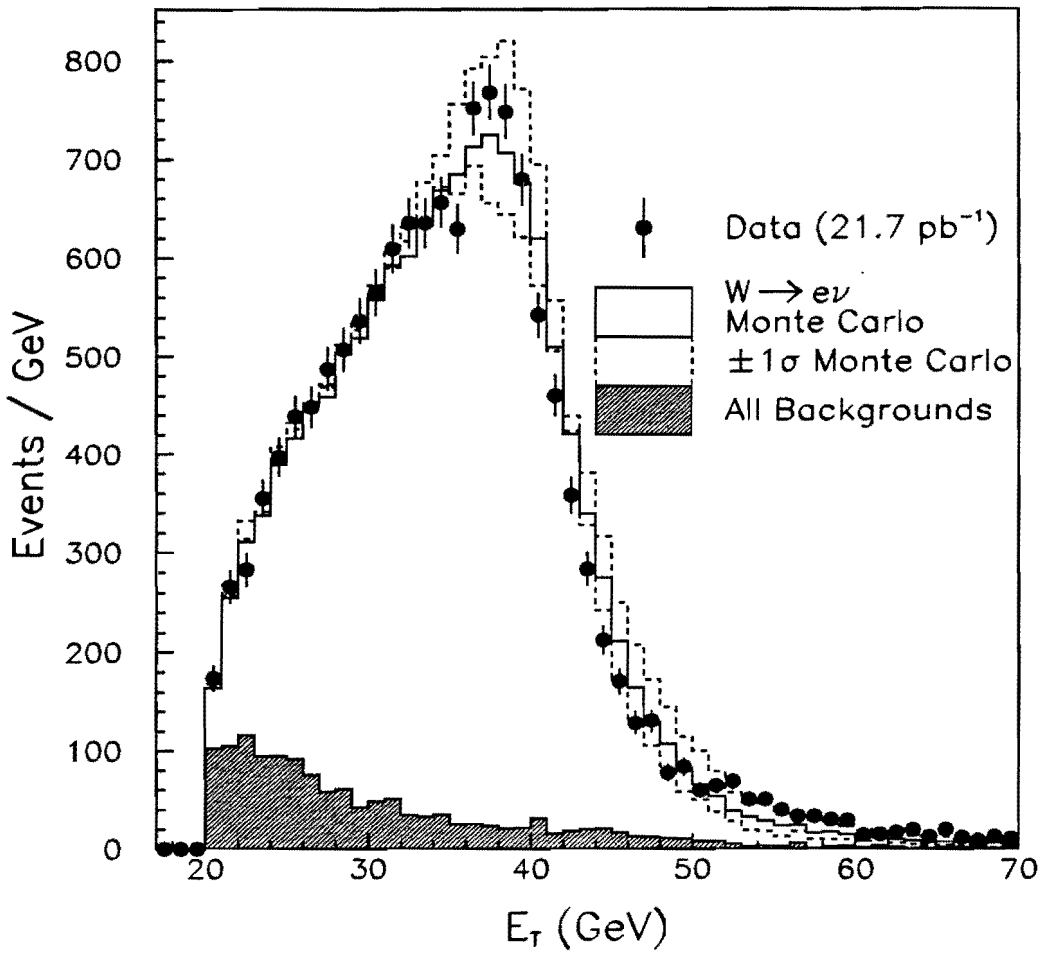

Fig. 5.12: Electron E_T in $W \to e\nu$ decays. The background contributions are described in Chapter 5 and the W shape is determined using the Monte Carlo described in Chapter 7. The σ in the Monte Carlo is the spread resulting from the uncertainty on the W boson P_T shape that is input to the Monte Carlo.

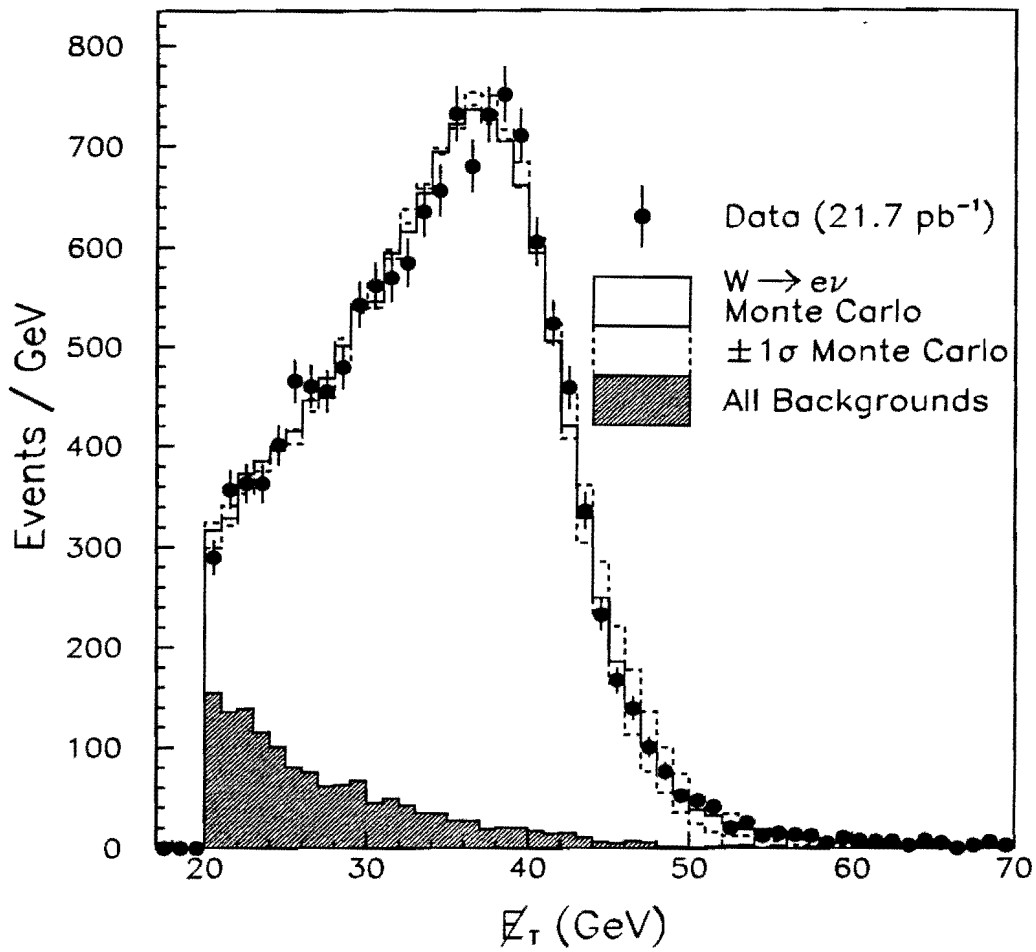

Fig. 5.13: $\not{E}_T$ of $W \rightarrow e\nu$ decays. The background contributions are described in Chapter 5 and the W shape is determined using the Monte Carlo described in Chapter 7. The σ in the Monte Carlo is the spread resulting from the uncertainty on the W boson P_T shape that is input to the Monte Carlo.

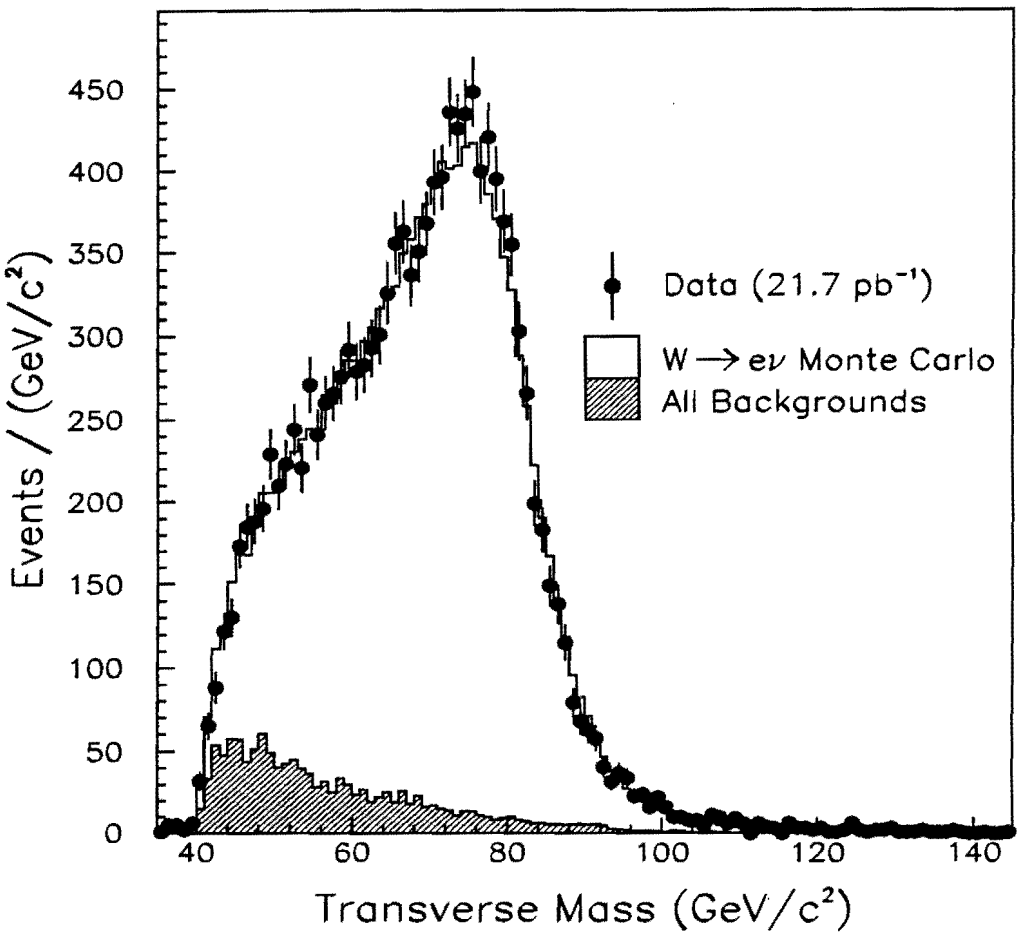

Fig. 5.14: Transverse mass of $W \to e\nu$ decays. The background contributions are described in Chapter 5 and the W shape is determined using the Monte Carlo described in Chapter 7.

Chapter 6

Z^0 Candidate Sample

The signature used to select $Z^0 \rightarrow e^+e^-$ candidates is an isolated, tight central electron plus a second, loosely-selected electromagnetic cluster. Very few processes mimic the signature of two high-P_T electron clusters. Thus, while the $W \rightarrow e\nu$ candidate sample had backgrounds from other processes totaling approximately 12% of the observed candidates, the backgrounds to the Z^0 candidates are observed total less than 2%.

6.1 Z^0 Candidate Selection

Z^0 candidates are selected from the inclusive electron sample by requiring an isolated tight central electron and a second isolated electron which passes loose selection criteria. The cuts on the tight electron are summarized in Table 3.1 and for the second electron in Table 3.2. Figure 3.3 shows the invariant mass spectrum of electron pairs passing these cuts. We observe 1312 events which fall in the 66 - 116 GeV/c^2 mass range.

6.2 Background from Hadron Jets

Two-jet, three-jet, *etc.*, hadron jet events can fake the signature of a Z^0 decay into electrons if two of the jets fluctuate in such a way as to fake electrons. As with the hadron jet background to W's, we attempt to measure the hadron jet background to Z^0's from the data by extrapolating Isolation shapes of the electrons. Figure 6.1 shows the electron-positron invariant mass *vs.* the Isolation of the second (loosely selected) cluster. In this plot we have already placed an Isolation cut on the first electron. While there is an unambiguous cluster at the Z^0 mass and low Isolation, some background events extend as far as 1.4.

We posit that all events with $Iso > 0.3$ on either leg are background from hadron jets. This assumption is equivalent to assuming that an Isolation cut of 0.3 is 100% efficient for electrons from Z^0's. This is quite reasonable, since in Figure 2.4(g) none of the 9000 W electrons have $Iso > 0.14$. We divide the electron pairs into four regions:

1) Events with $Iso_1 < 0.1$ and $Iso_2 < 0.1$
2) Events with $Iso_1 < 0.1$ and $Iso_2 > 0.3$
3) Events with $Iso_1 > 0.3$ and $Iso_2 < 0.1$
4) Events with $Iso_1 > 0.3$ and $Iso_2 > 0.3$

None of samples 2) - 4) have a Z^0 peak. The Z^0 background calculated from the equation:

$$\frac{Z^0 \text{ Background}}{\#\text{ Events in Region 2}} = \frac{\#\text{ Events in Region 3}}{\#\text{ Events in Region 4}}$$

We find that there are 20 ± 9 events background to the Z^0 candidates due to hadron jets. We find that 0^{+1}_{-0} of these come from the central-central Z^0's, whereas the plug contributes 14 ± 14 events background and the forward contributes 6 ± 3 events background.

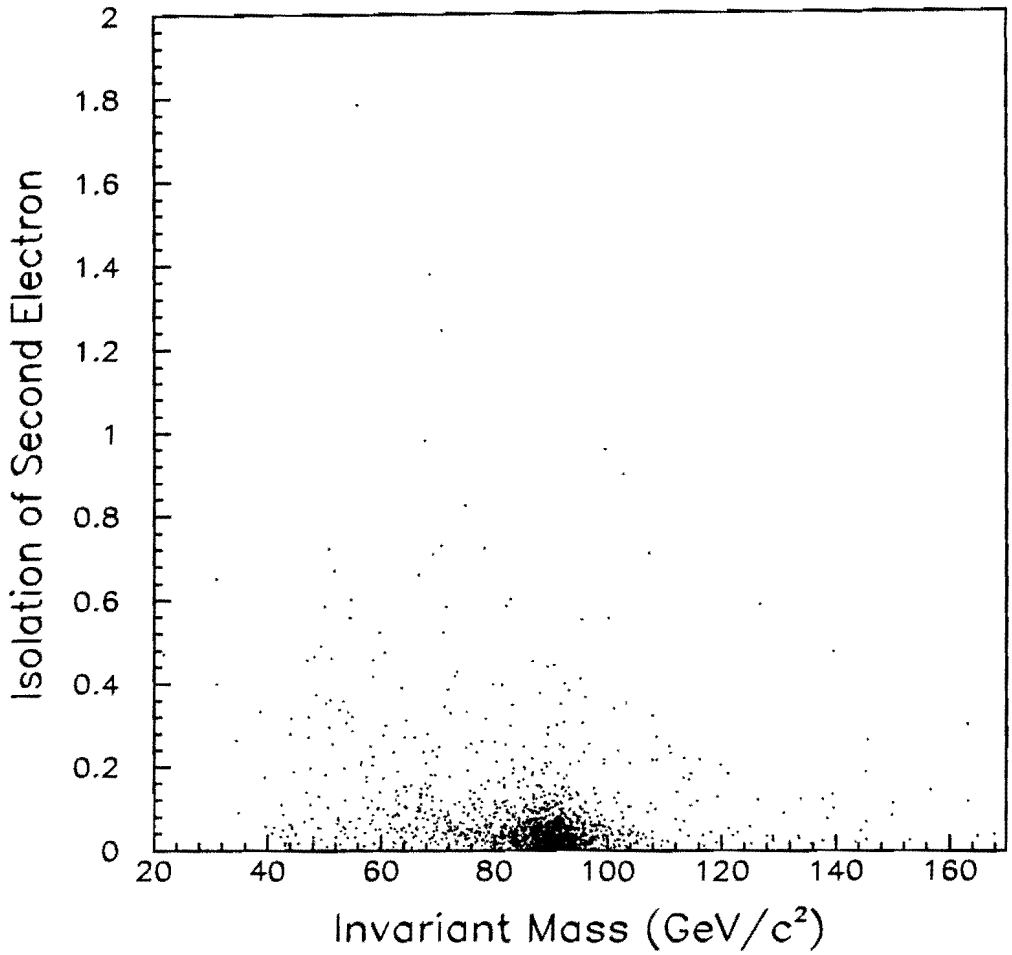

Fig. 6.1: Invariant mass, *M(ee)*, of the two electrons *vs.* the *Iso* of the second electron.

In the central region, the same-sign electrons in the central region serve as a cross check of background estimated by the *Iso* extrapolation method. Background would likely have equal numbers of same- and opposite-sign events. This hypothesis is supported by the fact that most non-isolated same-sign pairs have $E/p > 2$, indicating that they are mostly hadron misidentifications and not b electron pairs (b electron pairs would have $E/p < 2$, and would be mostly oppositely signed, with only $\approx$ 30% same-sign). There are 3 central-central same-sign $e^{\pm}e^{\pm}$ pairs in the mass window passing all our cuts, to be compared with the *Iso* estimate of 0^{+1}_{-0} central-central background events.

6.3 Background from $Z^0 \rightarrow \tau^+\tau^-$

The production of $Z^0 \rightarrow \tau^+\tau^-$ can fake $Z^0 \rightarrow e^+e^-$ decay if both taus decay via $\tau \rightarrow e\nu\nu$ and if the electrons form an invariant mass in the 66 - 116 GeV/c^2 invariant mass range. We use the ISAJET Monte Carlo and a detector simulation to estimate that the background due to $Z^0 \rightarrow \tau^+\tau^-$ as 1 $\pm$ 1 event.

6.4 Background from the Drell Yan Process

We apply a correction to the number of Z^0 candidates to account for the fact that some e^+e^- pairs in the 66 - 116 GeV/c^2 mass range come from continuum $p\bar{p} \rightarrow \gamma^* \rightarrow e^+e^-$, and not resonant Z^0 production. The correction is applied so our result is consistent with theoretical calculations, which typically use only the Z^0 amplitude, and not the γ^* term or the Z^0-γ^* interference term. We include in our Monte Carlo described in Chapter 7 both the Z^0 and γ^* amplitudes to determine the number of the events in our mass window from continuum Drell-Yan production. This correction also takes into account the effect of the mass window cut, since this is not accounted for in the Monte Carlo results of Chapter 7. We compute the integrals

$I_1 \equiv \int_{66}^{116} |Z^0 + \gamma|^2 dM$ and $I_2 \equiv \int_0^{\infty} |Z^0|^2 dM$. The number of Z^0 candidates must be divided by the number I_1/I_2, which we find to be 1.005 ± 0.002.

6.5 Background from W + Jet Production:

The process of W production, where the W decays to an electron and neutrino, can mimic $Z^0 \rightarrow e^+e^-$ decays if the W is produced in association with a hadron jet that showers in the EM calorimeters and the electron from the W and the jet together form the Z^0 mass. This background is accounted for in the hadron jet background (Section 6.2), since many of the second, misidentified electrons would be non-isolated. In this section we simply give a rough estimate of how big this background could be.

As discussed in Chapter 5, there are approximately 12000 W candidates, of which approximately 3000 have a jet with $P_T > 20$ GeV. From Chapter 2, the misidentification rate of jets to be identified as electrons is $\approx 10^{-5}$ for tight electron cuts. For the loose electron cuts used in the Z^0 selection, this rate is 10^{-3} - 10^{-4}. We might expect that 0.2 - 2 W + jet events will be identified as di-electrons, of which approximately one third (see Figure 6.2), or 0.06 - 0.6 will fall under the Z^0 peak.

6.6 Comparison of Z^0 Signal, Backgrounds:

Finally, in Figure 6.2 we show the invariant mass distribution for the e^+e^- candidates, along with the shape for the $Z^0+\gamma^*$, and the expected hadron jet background shape. The $Z^0+\gamma^*$ signal shape is derived from the Monte Carlo described in Chapter 7). The background shape is derived from 'dielectrons' in Region 2 in Section 6.2 above, and is normalized to have 20 events in the 66 - 116 GeV/c^2. The signal Monte Carlo is normalized to 1291 events in the 66 - 116 GeV/c^2 mass range.

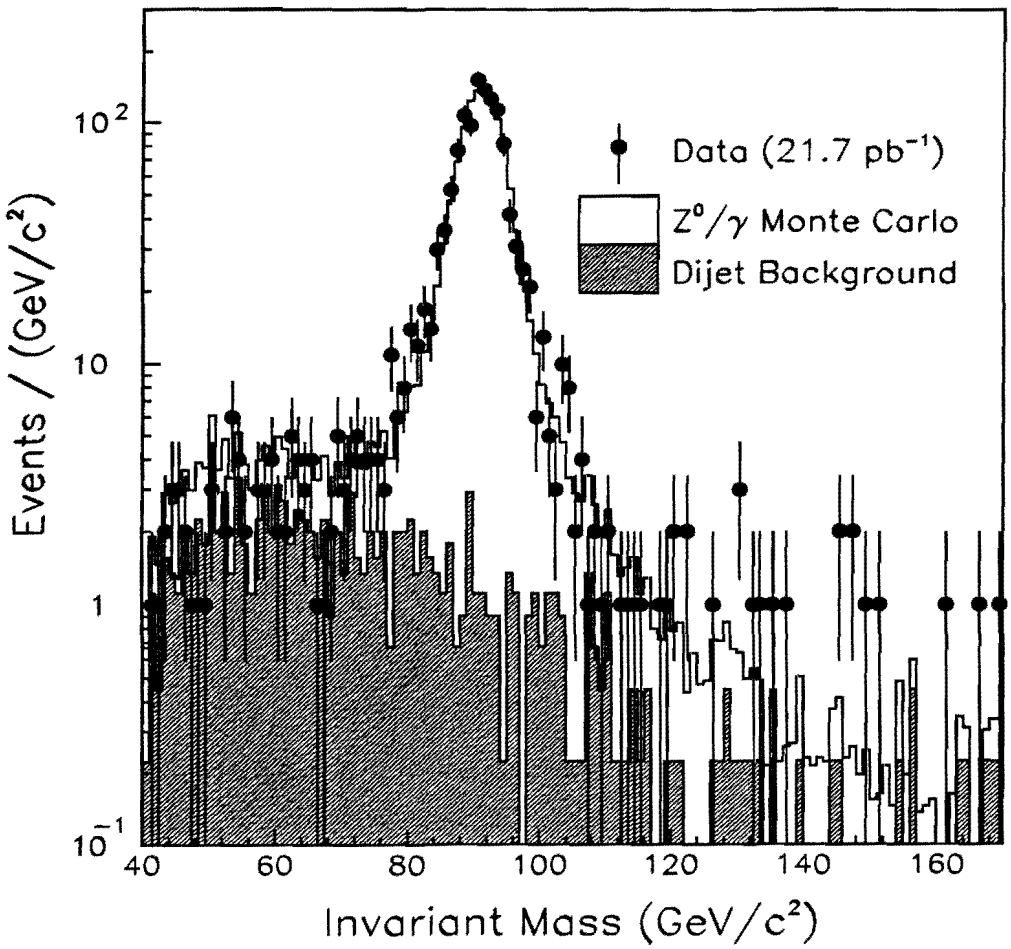

Fig. 6.2: Invariant mass of $Z^0 \to e^+e^-$ decays. The background shape is obtained from dielectron events where the first electron is isolated ($Iso < 0.1$) and the second electron is non-isolated ($Iso > 0.3$), normalized to have 20 events in the signal region. The Z^0 shape comes from a Monte Carlo described in Chapter 7, where Z^0 and Drell-Yan photon terms are included.

Chapter 7

Acceptances

We use a simple W and Z^0 Monte Carlo[44] to determine the kinematic and geometric acceptances A_W and A_Z. A detector model is then used to smear the leptons. The kinematic portion of the acceptance is the efficiency of W and Z^0 events to pass our P_T cuts on the leptons, and the geometric portion of the acceptances is the efficiency for the leptons to fall into the parts of the detector accepted as part of our fiducial volume.

7.1 Description of the Monte Carlo

The Monte Carlo generates W's and Z^0's using the lowest order diagram, $q\overline{q} \rightarrow W(Z^0)$. No quark-gluon diagrams or initial-state radiation are considered. The bosons are generated according to a relativistic Breit-Wigner distribution, truncated at ±6 widths. In order to mimic the effects of higher-order diagrams, the bosons are given a P_T according to the measured[45] W P_T distribution in $p\overline{p}$ collisions at $\sqrt{s} = 1.8$ TeV. The leptons are propagated to the calorimeter and smeared according the nominal detector resolutions. The electrons in our Monte Carlo are required to propagate to a fiducial region of the detector.

An underlying event model is used to model the $\not{E}_T$ resolution. In this model, we use ISAJET to generate W events and a detector simulation to parameterize the component of the $\not{E}_T$ parallel and perpendicular to the P_T of the boson as a function of the boson P_T. Given a generated boson P_T, the $\not{E}_T$ in our present Monte Carlo is then smeared according to the parameterization from ISAJET. Using `the parameters $M_W = 80.21\ GeV/c^2$, $M_Z = 91.18\ GeV/c^2$, and $sin^2\theta_W \equiv 1 - \frac{M_W^2}{M_Z^2}$ and the MRS D-' parton distribution functions,[46] we find $A_W = 0.3416 \pm 0.0008$ and $A_Z = 0.4120 \pm 0.0008$, where the errors are statistical only. Note that the Z^0 acceptance is higher, as expected, because central-central Z^0's have two chances of having one leg in the central.

7.2 Systematic Uncertainties in A_W, A_Z

In this section, we investigate the systematic uncertainties due the choice of parton distribution functions (PDF's), the underlying event model, the boson masses, the calorimeter energy scales, the P_T distribution input to the Monte Carlo, and higher order diagrams. For each possible source of systematic uncertainty, we repeat the Monte Carlo calculation with different values for these parameters and take the error to be one half of the spread in the results. For the ratio of cross sections, half the spread in the ratio of acceptances, A_W/A_Z, is used as the uncertainty. As is discussed below, while the individual acceptances are sensitive to variations in these parameters, the ratio is more stable. In the tables which follow, all of the values for W and Z^0 acceptances have a statistical error of $\pm$ 0.2%.

7.2.1 Systematics from Parton Distribution Functions

In order to estimate the systematic uncertainty due to the parton distribution functions, we run the Monte Carlo with different sets of PDF's not excluded by current experimental data. Using M_W = 80.21 GeV/c^2, M_Z = 91.18 GeV/c^2, and $sin^2\theta_W$ = 0.2263, and the underlying event model, we find a 1.1% uncertainty in A_W/A_Z due to PDF's, as shown in Table 7.1 below.

Table 7.1: Acceptances Derived Varying Parton Distribution Functions

PDF	A_W (%)	A_Z (%)	A_W/A_Z
MRS D-'	34.16	41.02	0.833
MRS D0'	34.58	41.33	0.837
MRS S0'	34.86	41.18	0.847
CTEQ 1M	35.22	41.37	0.851
CTEQ 1MS	35.17	41.52	0.847
CTEQ 1L	34.22	40.96	0.835
CTEQ 1ML	35.33	41.59	0.849
Uncertainty:	0.59	0.29	0.009

7.2.2 Systematics from M_W, $sin^2\theta_W$

The acceptances depend upon the W mass through the lepton P_T's and $sin^2\theta_W$. Using M_Z = 91.18 GeV/c^2, and MRS D-' PDF's we find a 0.1% uncertainty in A_W/A_Z, as shown in Table 7.2 below:

Table 7.2: Acceptances Derived Varying M_W

M_W (GeV/c^2)	A_W (%)	A_Z (%)	A_W/A_Z
80.06	34.18	40.96	0.834
80.21	34.16	41.02	0.833
80.36	34.24	41.04	0.834
Uncertainty:	0.04	0.04	0.001

7.2.3 Systematics from the Boson P_T Distribution

The P_T distribution which we input to our Monte Carlo is important because we are generating W's and Z^0's using a lowest order diagram. The P_T distribution is our way of taking into account the generation of higher order diagrams. We take the 'nominal' P_T distribution to be the measured spectrum, the 'soft' P_T distribution to be the distribution one gets when varying the nominal by one error bar in each bin so as to give a more steeply falling spectrum (deforming about the point $P_T = 16\ GeV/c$), and the 'hard' distribution to be the shape that one gets by varying by one sigma so as to get a more slowly falling spectrum. Trying these three shapes for the P_T choice, we find (using MRS D-' and the nominal boson masses), a 0.2% variation in A_W/A_Z, is found, as shown in Table 7.3 below.

Table 7.3: Acceptances Derived Varying P_T Distribution

P_T Choice	A_W (%)	A_Z (%)	A_W/A_Z
Soft	34.42	41.31	0.835
Nominal	34.16	41.02	0.833
Hard	34.04	40.94	0.831
Uncertainty:	0.19	0.13	0.002

In the above estimate of the systematic error from the boson P_T distribution, it was assumed that the W and Z^0 have the same P_T spectra. Experimental measurements of these spectra are consistent with this assumption.[47] Theoretical calculations[48] further confirm that the differences are less than 2%. If we assume that the spectra are different, and use calculations[49] of their individual P_T spectra, we observe a shift in A_W/A_Z of 0.0010 from our nominal result. The extra uncertainty from this effect is thus 0.0005, and is negligible compared to the ± 0.002 uncertainty from our knowledge of the W P_T spectrum.

7.2.4 Systematics from the Underlying Event Model:

Finally, we try to estimate the effect of the choice of underlying event model on the acceptances. The underlying event model goes most sensitively into the smearing of the $\not{E}_T$, and hence into the result for A_W. We have, in addition to the simulation-based model, estimated the acceptances with two other underlying event models. One model, used in CDF's previous measurement of the W mass, has been described elsewhere.[50]

We have also used a model[51] which uses Z^0 data to characterize the calorimeter resolution. This last model is identical in spirit to the simulation-based model, but Z^0 data from this run are used to measure the calorimeter response as a function of boson P_T instead of the detector simulation. This new method would in principle be the best model to use, since it comes directly from the data, but we lack adequate statistics in the Z^0's at high P_T, where the $\not{E}_T$ smearing is the most dramatic. We find a 0.6% systematic uncertainty in A_W/A_Z due to the underlying event model, as shown in Table 7.4.

Table 7.4: Acceptances Derived Varying Underlying Event

Model	A_W (%)	A_Z (%)	A_W/A_Z
Z^0 Data Model	34.39	41.02	0.838
ISAJET Model	34.16	41.02	0.833
W Mass Model	34.00	41.02	0.829
Uncertainty:	0.20	-	0.005

7.2.5 Systematics from the Energy Scale.

The energy scale in the data is set using $Z^0 \rightarrow e^+e^-$ decays to an accuracy of approximately 0.2%. We vary the energy scale of the central calorimeters in the simulation by 0.5% and compare the derived acceptances in Table 7.5. Variations in the plug scale cause similar variations in A_W/A_Z, while variations in the forward energy scale result in 0.2 times this variation in

A_W/A_Z because the Forward has 0.2 times the acceptance of the central and Plug. We take the uncertainty due to the 0.2% possible deviation in the scale to be one half the effect in Table 7.5, since acceptances for 0.5% changes in scale are shown. The uncertainty in A_W/A_Z due to the energy scale is estimated to be 0.4%.

Table 7.5: Comparison of Acceptances for Different Energy Scales.

Energy Scale	A_W (%)	A_Z (%)	A_W/A_Z
0.995	34.05	40.56	0.840
1.000	34.15	41.02	0.833
1.005	34.25	40.68	0.842
Uncertainty	0.05	0.30	0.003

7.3 Effects of Radiative Corrections

The effects of radiative decay are largely accounted for in our calculations of the E/p and Iso efficiencies for electrons (See Chapter 8), since most radiated photons tend to be collinear with one of the electrons in W or Z^0 decay. In order to account for the effect of photons radiated at wide angles to the electrons that would shift the observed e^+e^- pair mass downward, we use a Monte Carlo[52] with the full matrix elements for radiative decay, to find that 0.3 ± 0.2 % of Z^0's fall outside of the 66-116 GeV/c^2 mass range for Z^0's. This shifts the result for A_Z from 0.4102 to 0.4090 and A_W/A_Z from 0.833 to 0.835.

7.4 Comparison with an $O(\alpha_S)$ Monte Carlo

The generator in our Monte Carlo uses only the lowest order (LO) diagram for boson production, namely $q\overline{q} \rightarrow W$ or Z^0. The bosons are then given P_T according to the measured spectrum for W's in order to mimic the effect of higher order diagrams which also produce W's and Z^0's, such as $qg \rightarrow Wq$ or Z^0q and $qq \rightarrow Wg$ or Z^0g. With the LO Monte Carlo the η distribution

of leptons seems well-modeled (see Figures 3.4 and 3.8). It is likely that the ratio of acceptances is insensitive to QCD corrections, since one chooses a common leg in the central region and then the only thing that can change the ratio is a difference in the way the second electron in Z^0's and the neutrino in W's are distributed. In this section we investigate the assumption that the ratio A_W/A_Z is insensitive to higher-order diagrams.

We have employed a next-to-leading order (NLO) Monte Carlo by Giele *et al.*[53] which includes next-to-leading order diagrams. The events from this generator are fed through the same detector simulation as with the LO Monte Carlo so as to minimize differences in the comparison. The only exception is that the E_T modeling is not applied to the NLO Monte Carlo because it contains its own model. The results are in Table 7.6 below. The difference in results, 0.006, is taken as the systematic uncertainty from higher order diagrams.

Table 7.6: Comparison of Acceptances from the LO and NLO Generators.

Generator	A_W	A_Z	A_W/A_Z
Lowest Order	0.342	0.409	0.835
Next-to-Leading Order	0.341	0.406	0.841
Uncertainty	0.001	0.003	0.006

The Giele calculation uses the matrix elements calculated to next-to-leading order (NLO) for $e^+e^- \rightarrow$hadrons. Through crossing symmetry the matrix element for $e^+e^- \rightarrow V \rightarrow q\overline{q}g$, for example, may be related to that for $q\overline{q} \rightarrow Vg \rightarrow e^+e^-g$, where $V = \gamma^*$ or Z^0. In this way initial state radiation, *etc.*, may be calculated using far fewer diagrams. The final state partons are evolved in this Monte Carlo down to some scale s_{min}. After reaching this scale, partons are clustered into jets of a given cone size and minimum E_T^{cut} chosen to match the experiment. The scale s_{min} is chosen such that the dependence of observable cross sections have plateaued in this variable. Inclusive W or Z^0 production, therefore, is modeled by generating W + 0 jet production, but with the experimental jet E_T^{cut} set to an arbitrarily large value (like 900 *GeV*). The resulting calculations are thus fully differential in all observables, in contrast to other NLO calculations,[54] which merge together perturbative and non-perturbative calculations

7.5 Summary of Acceptance Results

We find for the acceptances:

$$A_W = 0.342 \pm 0.001 \text{ (stat.)} \pm 0.008 \text{ (sys.)}$$
$$A_Z = 0.409 \pm 0.001 \text{ (stat.)} \pm 0.005 \text{ (sys.)}$$
$$A_W/A_Z = 0.835 \pm 0.001 \text{ (stat.)} \pm 0.013 \text{ (sys.)}$$

We also use the Monte Carlo to calculate the fractions F_{cc}, F_{cp}, and F_{cf} of Z^0's with one leg in the central that have the second leg in the central, plug, or forward, respectively. We find:

$$F_{cc} = 0.372 \pm 0.001 \text{ (stat.)} \pm 0.007 \text{ (sys.)}$$
$$F_{cp} = 0.509 \pm 0.001 \text{ (stat.)} \pm 0.007 \text{ (sys.)}$$
$$F_{cf} = 0.120 \pm 0.001 \text{ (stat.)} \pm 0.004 \text{ (sys.)}$$

Again, it is important to note that the uncertainty in the ratio of acceptances is smaller than the sum of the uncertainties in the individual acceptances. This smaller uncertainty is a result of the method of requiring a common central electron for W and Z^0 decays which decreases our sensitivity to many of the systematic effects discussed in this chapter.

Chapter 8

Efficiencies

This chapter concerns the efficiencies of the leptons from W and Z^0 decays to pass the electron selection criteria described in Chapter 3 and to pass the electron trigger. To estimate these efficiencies, we select a sample of high P_T electrons unbiased by the cuts whose efficiencies we wish to estimate. The high P_T electrons we use come from W and Z^0 decay, but are selected with criteria different from those used in Chapter 3.

We identify 5 efficiencies which must be measured: (1) the efficiency, which we call "c_1," for a central electron in the fiducial region from W or Z^0 decay to pass the tight cuts; (2) the efficiency, "c_2," for the second leg of a Z^0 in the fiducial central region to pass the loose central cuts; (3) the efficiency, "p," for the second leg of a Z^0 in the plug region to pass the loose plug cuts; (4) the efficiency, "f," for the second leg of a Z^0 in the forward region to pass the loose forward cuts; and finally (5) the efficiency, "ε_T" of a central electron from W or Z^0 decay which passes the tight c_1 cuts to pass the electron trigger.

The electron identification efficiencies are measured using the second leg of Z^0 events. The Z^0 events are selected with tight cuts on the first central leg and asking for a second cluster that has an invariant mass with the first in a tight window around the Z^0 mass. No identification cuts are used on the second leg. Efficiencies are then measured by observing what fraction of the Z^0 second electrons pass the identification cuts.

8.1 Tight Central Identification Efficiency, c_1

We select a sample of central-central Z^0's which satisfy the following requirements on the event:

One leg passes tight cuts
Second electromagnetic cluster in central with $E_T > 20\ GeV$
CTC (opposite sign) track pointing at 2nd cluster, $P_T > 5\ GeV$
$Iso < 0.05$ on first electron
Had/EM < 0.05 on first electron
$81 < M_{e+e-} < 101\ GeV/c^2$

There are 514 central-central Z^0's satisfying these cuts. This composes our efficiency sample. The efficiency each of the tight central cuts c_1 are summarized in Table 8.1. The result is that the cuts are 85.1 ± 1.1 % efficient.

There two corrections to apply to the result for c_1. There is first an efficiency for the offline track reconstruction algorithm to reconstruct a track. This efficiency has been estimated by examining at W's which pass $\not{E}_T$ triggers in Level 2 and Level 3. These triggers require only an EM cluster and $\not{E}_T$. W candidates were selected by requiring $E_T > 25\ GeV$, $\not{E}_T > 25\ GeV$, $Lshr < 0.2$, $Iso < 0.1$, $[(\chi^2{}_{strip})^2 + (\chi^2{}_{wire})^2]^{1/2} < 20$. Events with no 3-dimensional track pointing at the cluster were counted as tracking failures. The tracking efficiency was found to be 99.7 ± 0.2 %

We also correct for a small E/p bias in our Z^0 efficiency sample. In our Z^0 efficiency sample, we require a track with $P_T > 5\ GeV$ to point at the second cluster. We made this cut to suppress events with like-sign tracks, which act as an indicator of the background in the efficiency sample. This cut also throws away real Z^0's with $E/p > 4$ from our efficiency sample. To estimate the magnitude of this effect, we scanned the Z^0's which failed the $P_T > 5\ GeV$ cut on the second electron. We factor an additional efficiency of 99.5 ± 0.3 % efficiency as an estimate of this bias.

Table 8.1: Efficiency of the Tight Central Cuts

Efficiency c_1 , 514 Z^0's in sample	
Cut	Efficiency (%)
Had/EM	100.0 ± 0.5
Iso	97.3 ± 0.5
Lshr	98.0 ± 0.4
E/p	95.0 ± 0.7
δx	94.1 ± 0.8
δz	98.2 ± 0.4
$\chi^2 strip$	95.0 ± 0.7
All Cuts	85.1 ± 1.1
Tracking, E/p Corrections	99.2 ± 0.4
c_1 Efficiency	84.5 ± 1.2

8.2 Loose Central Identification Efficiency, c_2

We use the same sample of central-central Z^0's as was used to measure the tight cut efficiency c_1, but now we apply just the loose cuts to the second leg. We find a 91.7 ± 0.8 % efficiency of the cuts, as summarized in Table 8.2.

Table 8.2: Efficiency of the Loose Central Cuts

Efficiency c_2 , 514 Z^0's in sample	
Cut	Efficiency (%)
Had/EM	100.0 ± 0.5
Iso	97.3 ± 0.5
E/p	95.0 ± 0.7
All Cuts	92.4 ± 0.7
Tracking, E/p Corrections	99.2 ± 0.4
c_2 Efficiency	91.7 ± 0.8

8.3 Loose Plug Identification Efficiency, p

To measure the efficiency of the plug electron identification efficiencies, we select central-plug Z^0 events which pass the following cuts:

One central leg that passes tight cuts
Second electromagnetic cluster in plug with $E_T > 15\ GeV$
No other jets with $E_T > 10\ GeV$ in the event
$81 < M_{e+e-} < 101\ GeV/c^2$
$Iso < 0.05$ on central electron
Had/EM < 0.05 on central electron
VTX Occupancy > 0.5 in octant pointing to plug cluster

There are 418 events passing these cuts which will compose our efficiency sample in the plug. We find a 90.9 ± 1.4% efficiency (see Table 8.3).

Table 8.3: Efficiency of the Loose Plug Cuts

Efficiency p, 418 Z^0 's in sample	
Cut	Efficiency (%)
Had/EM	100.0 ± 0.3
Iso	96.4 ± 0.9
$\chi^2_{3\times3}$	95.2 ± 1.1
p Efficiency	90.9 ± 1.4

8.4 Loose Forward Identification Efficiency, f

To measure the efficiency of the forward electron identification, we select a sample of central-forward Z^0 events identical to the plug sample above, but this time with a forward electron with $E_T > 10\ GeV$ and VTX Occupancy > 0.25. There are 64 events passing these cuts. We find an efficiency of 85.9 ± 4.4%.

Table 8.4: Efficiency of the Loose Forward Cuts

Efficiency f, 64 Z^0 's in sample	
Cut	Efficiency (%)
Had/EM	100.0 ± 1.8
Iso	85.9 ± 4.4
f Efficiency	85.9 ± 4.4

8.5 Central Electron Trigger Efficiency, ε_T

The trigger efficiency is defined as the probability that a high P_T central electron which passes the tight cuts c_1 will pass the inclusive electron trigger. The efficiency of the inclusive electron trigger in Level 2 and Level 3 is measured with W's that come in on an independent trigger. We select W's that pass our electron cuts and come in on a trigger that selects events with E_T and an EM cluster in the central. A total of 10813 of our W candidates come in on the E_T triggers. Table 8.5 below shows the results of events that pass the inclusive electron triggers in Level 2 and Level 3.

Table 8.5: Efficiency of the Central Electron Trigger

Efficiency ε_T, 10813 W's in efficiency sample	
Trigger	Efficiency (%)
Level 1 Trigger	99.2 ± 0.1
Level 2 Trigger	91.5 ± 0.3
Level 3 Trigger	98.2 ± 0.1
Total Trigger Eff., ε_T	89.2 ± 0.3

The Level 1 calorimeter trigger efficiency is estimated using inclusive muon events that trigger the Level 1 and Level 2 muon triggers. Calorimeter clusters are searched for elsewhere in these events and are run through a simulation of the trigger to see if any calorimeter clusters in these events should have also satisfied the Level 1 calorimeter trigger. The Level 1 calorimeter trigger efficiency is the ratio of these muon-triggered events with a cluster elsewhere in the event that triggered the calorimeter trigger divided by the number that should have triggered the calorimeter trigger.

The Level 1 Calorimeter Trigger is 99.18 ± 0.08% efficient for $E_T > 12\ GeV$ (see Figure 2.15).

8.6 Combined Efficiencies ε_W and ε_Z :

Combining the results above, we may now find the efficiencies ε_W and ε_Z for W and Z^0 events to pass our electron selection. The W selection efficiency for electrons in the fiducial region is

$$\varepsilon_W = \varepsilon_T \cdot c_1$$

The Z^0 efficiency is more complicated because the central-central Z^0's have two chances for passing the inclusive electron trigger and because we have placed different lepton ID cuts in the three detector regions:

$$\varepsilon_Z = \varepsilon_T \cdot c_1 \ [\ F_{cc}(2c_2 - \varepsilon_T \cdot c_1) + F_{cp}p + F_{cf}f\ ]$$

where the fractions F_{cc}, F_{cp}, and F_{cf} are the fractions of the Z^0's in our acceptance which have one leg in the central region and the second in the central, plug, and forward, respectively. These fractions are determined with the Monte Carlo described in Chapter 7. Combining the efficiency numbers from above and the Monte Carlo results for F_{cc}, F_{cp}, and F_{cf}, we find

$$\varepsilon_W = 75.4 \pm 1.0\ \%$$
$$\varepsilon_Z = 72.9 \pm 1.6\ \%$$
$$\varepsilon_W / \varepsilon_Z = 1.035 \pm 0.016$$

It is important to note that the factor $\varepsilon_T \cdot c_1$ nearly cancels in the ratio $\varepsilon_W / \varepsilon_Z$, and thus the systematic error in $\varepsilon_W / \varepsilon_Z$ is smaller than one gets adding the errors of ε_W and ε_Z in quadrature. This lower systematic uncertainty is one of the motivations for selecting a common tight central electron in measuring the ratio of the two cross sections.

Chapter 9

Conclusions

9.1 Summary of Results for R

The background, efficiency, and acceptance results from the previous sections are summarized in Table 9.1. We find for R:

$$R = 10.90 \pm 0.32\ (stat.) \pm 0.29\ (sys.).$$

We have also redone this analysis using an E_T cut on the first leg of $E_T > 25\ GeV$ (for both W's and Z^0's), and a cut of $E_T > 25\ GeV$ (for W's). The results of this cross check are summarized in Table 9.2. As expected, the number of background events decreases, but the systematic uncertainty due to the underlying event resolution increases and the statistical error increases. The results are shown below:

$$\frac{\sigma \cdot B(W \rightarrow e\nu)\ (20\ GeV\ \text{cuts})}{\sigma \cdot B(W \rightarrow e\nu)\ (25\ GeV\ \text{cuts})} = 0.992 \pm 0.003\ (stat.) \pm 0.008\ (sys.)$$

$$\frac{\sigma \cdot B(Z^0 \rightarrow e^+e^-)\ (20\ GeV\ \text{cuts})}{\sigma \cdot B(Z^0 \rightarrow e^+e^-)\ (25\ GeV\ \text{cuts})} = 0.995 \pm 0.007\ (stat.) \pm 0.008\ (sys.)$$

$$\frac{R\ (20\ GeV\ \text{cuts})}{R\ (25\ GeV\ \text{cuts})} = 0.995 \pm 0.008\ (stat.) \pm 0.011\ (sys.)$$

where the statistical uncertainty in the ratios reflects the large statistical overlap between the two samples and the systematic uncertaintiy in the ratios is the additional uncertainty in the Monte Carlo that results from making higher kinematic cuts. The two measurements are complementary, since both the background and acceptance calculations are thus checked. Although this second result provides a good cross check, we use the 20 GeV kinematic cuts in Table 9.1 for our result.

Recall that the ratio of cross sections is given by the formula

$$R \equiv \frac{\sigma \cdot B(p\overline{p} \to W \to e\nu)}{\sigma \cdot B(p\overline{p} \to Z^0 \to ee)} = \frac{\sigma(p\overline{p} \to W)}{\sigma(p\overline{p} \to Z^0)} \frac{\Gamma(W \to e\nu)}{\Gamma(Z^0 \to ee)} \frac{\Gamma(Z^0)}{\Gamma(W)}$$

We use a theoretical calculation[55] of the ratio of production cross sections $\sigma(p\overline{p} \to W)/\sigma(p\overline{p} \to Z^0) = 3.33 \pm 0.03$, together with the LEP[56] measurements of $\Gamma(Z^0) = 2.492 \pm 0.007$ GeV and $\Gamma(Z^0 \to e^+e^-) = 83.33 \pm 0.30$ MeV to obtain a measurement for the branching ratio:

$$\Gamma(W \to e\nu)/\Gamma(W) = 0.1094 \pm 0.0033(stat.) \pm 0.0031(sys.).$$

The Standard Model Prediction,[14] assuming heavy ($m_{top} > M_W - m_b$) top is $\Gamma(W \to e\nu)/\Gamma(W) = 0.1084 \pm 0.0002$. If we use a calculation[57] of the W leptonic partial width $\Gamma(W \to e\nu) = 225.8 \pm 0.9$ GeV, we may obtain a value for the W decay width:

$$\Gamma(W) = 2.064 \pm 0.061 \ (stat.) \pm 0.059(sys.) \ GeV.$$

The Standard Model prediction,[14] assuming a heavy ($m_{top} > M_W - m_b$) top and using the measured W mass and the value of G_F from muon decay, is $\Gamma(W) = 2.067 \pm 0.021$ GeV.

In order to set a model-independent limit on the top mass, we use the 'inverse' branching ratio since its error is more nearly gaussian:

$$\Gamma(W)/\Gamma(W \to e\nu) = 9.14 \pm 0.28(stat.) \pm 0.26(sys.)$$

As the mass of the top quark increases toward the W mass, the partial width $\Gamma(W \to tb)$ goes to zero, and the ratio $\Gamma(W)/\Gamma(W \to e\nu)$ approaches the Standard Model value of 9.225. In Figure 9.1 we plot our value for $\Gamma(W)/\Gamma(W \to e\nu)$ along with the expected curve as a function of top mass. We establish the limit[58]

$$m_{top} > 62\ GeV/c^2 \text{ (95\% confidence level)}$$

We emphasize again that this limit is independent of models of the top quark's allowed decay modes, providing that the W can decay with normal coupling to $t\bar{b}$. Previous direct searches for the top have assumed that the top must decay only to a W boson and a b quark.

9.2 Future Prospects for $BR(W \to e\nu)$ and $\Gamma(W)$

The uncertainties in the present measurement of $BR(W \to e\nu)$ are listed in Table 9.3, along with the uncertainties from the previous[24] measurement from CDF using electrons. As well, we list possible improvements in the statistical and systematic uncertainties with future collider data sets to be collected at CDF. Note that the systematic uncertainty in this measurement from the backgrounds is larger than the previous measurement[24] because we have not employed the 'no jet' cut described in that paper. The 'no jet' cut introduced a 0.5% uncertainty not present in our result. The methods of this thesis will allow the backgrounds to be better studied in the future and will allow the uncertainty due to the background to be decreased with more data. The next barrier to be broken in the BR measurement is in the Monte Carlo, which could be improved by using the Giele Monte Carlo,[53] which only became available late in the course of this analysis.

The predicted systematic uncertainties for future experiments are derived assuming that some systematic uncertainties will scale with statistics. Others are expected to improve because of other measurements that will be made. For example, future deep inelastic scattering experiments at HERA and W charge asymmetry measurements at CDF will constrain the u/d ratio in the

Table 9.1: Summary of Results for R.
Kinematic Cuts of $E_T(1st\ ele) > 20\ GeV$,
$\not{E}_T > 20\ GeV$

	W's	Z^0's
Candidates:	13796	1312
Background:		
hadron jets	898 ± 155	20 ± 9
$W^{\pm}\to\tau^{\pm}\nu$	473 ± 29	-
$Z^0\to\tau^+\tau^-$	48 ± 7	1 ± 1
$Z^0\to e^+e^-$	281 ± 42	-
heavy top	0^{+52}_{-0}	-
Total Background:	1700^{+171}_{-163}	21 ± 9
Signal:	$12096 \pm 117^{+163}_{-171}$	1291 ± 36 ± 9
Acceptance:		
$A_{W,Z}$	0.342 ± 0.008	0.409 ± 0.005
$A_W\ /\ A_Z$	0.835 ± 0.013	
F_{cc}	-	0.372 ± 0.007
F_{cp}	-	0.509 ± 0.007
F_{cf}	-	0.120 ± 0.004
Efficiencies:		
$\varepsilon_T \cdot c_1$	0.754 ± 0.011	0.754 ± 0.011
c_2	-	0.917 ± 0.008
p	-	0.909 ± 0.014
f	-	0.859 ± 0.044
$\varepsilon_{W,Z}$	0.754 ± 0.011	0.729 ± 0.016
$\varepsilon_W\ /\ \varepsilon_Z$	1.035 ± 0.016	
Drell-Yan Correction	-	1.005 ± 0.002
Luminosity	21701 nb^{-1}	21701 nb^{-1}
Vertex Cut Effic.	0.962 ± 0.001	0.962 ± 0.001
$\sigma \cdot B$ (no lum error)	2.250 ± 0.022 ± 0.062	0.206 ± 0.006 ± 0.005
$\sigma(W\to e\nu)\ /\sigma(Z\to ee)$	10.90 ± 0.32 (*stat.*) ± 0.29 (*sys.*)	

Table 9.2: Summary of Results for R
Kinematic Cuts of E_T(1st ele) > 25 GeV,
$\not{E}_T$ > 25 GeV

	W's	Z^0's
Candidates:	11182	1201
Background:		
hadron jets	207 ± 40	5 ± 5
$W^{\pm}\to\tau^{\pm}\nu$	313 ± 18	-
$Z^0\to\tau^+\tau^-$	22 ± 6	0 ± 1
$Z^0\to e^+e^-$	216 ± 32	-
heavy top	0^{+30}_{-0}	-
Total Background:	758^{+62}_{-55}	5 ± 5
Signal:	$10424 \pm 106^{-55}_{+62}$	1196 ± 35 ± 5
Acceptance:		
$A_{W,Z}$	0.292 ± 0.011	0.375 ± 0.006
A_W / A_Z	0.779 ± 0.020	
F_{cc}	-	0.411 ± 0.007
F_{cp}	-	0.504 ± 0.007
F_{cf}	-	0.085 ± 0.003
Efficiencies:		
$\varepsilon_T \cdot c_1$	0.754 ± 0.011	0.754 ± 0.011
c_2	-	0.917 ± 0.007
p	-	0.909 ± 0.014
f	-	0.859 ± 0.044
$\varepsilon_{W,Z}$	0.757 ± 0.010	0.735 ± 0.015
ε_W / ε_Z	1.026 ± 0.015	
Drell-Yan Correction	-	1.005 ± 0.002
Luminosity	21701 nb^{-1}	21701 nb^{-1}
Vertex Cut Effic.	0.962 ± 0.001	0.962 ± 0.001
$\sigma \cdot B$ (no lum error)	2.268 ± 0.023 ± 0.078	0.207 ± 0.006 ± 0.005
$\sigma(W\to e\nu)$ / $\sigma(Z\to ee)$	10.96 ± 0.34 (*stat.*) ± 0.33 (*sys.*)	

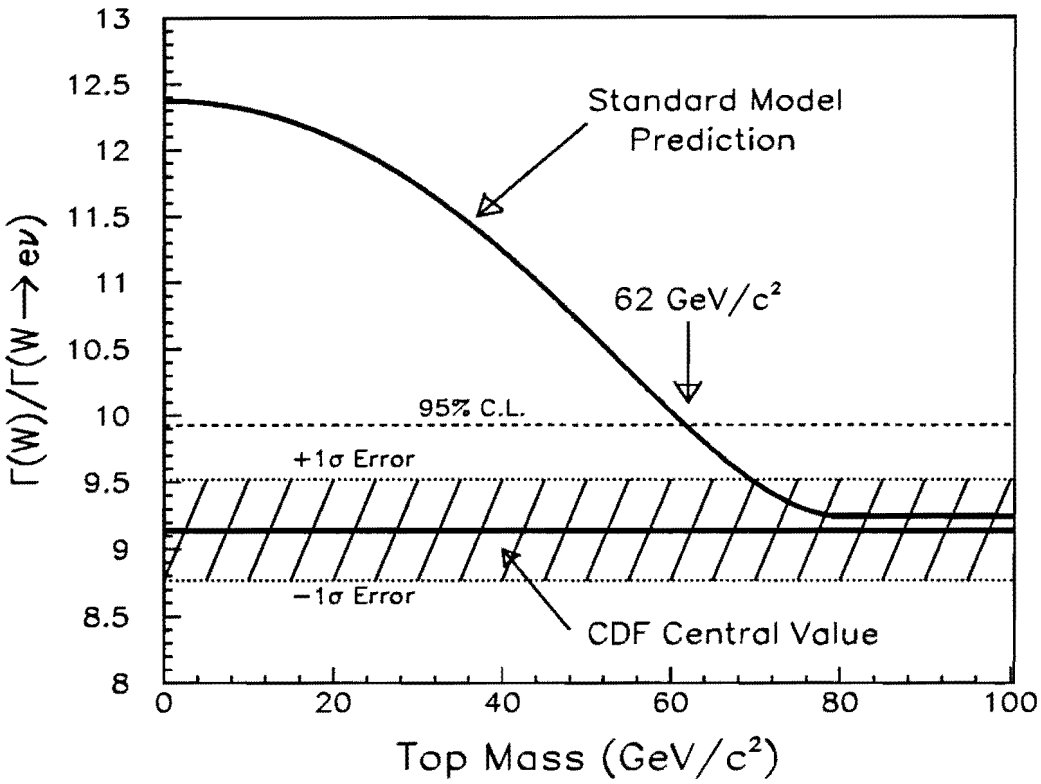

Fig. 9.1: $BR(W \to e\nu)^{-1}$ *vs.* M_{top}. As the top mass increases toward the W mass, the phase space for the decay $W \to tb$ is reduced.

proton and the allowed parton distribution functions. A future measurement of $\frac{d\sigma}{dP_T}(W)$ from either CDF or DØ would constrain the Monte Carlo modeling uncertainty. Even a measurement of the W P_T shape using the present CDF data would decrease the uncertainty from the P_T shape by a factor of two.

With the uncertainties quoted in Table 9.3 for $BR(W \rightarrow e\nu)$, one would, for example, be able to set limits of $m_{top} > 72$ (77) GeV/c^2 on the top quark in 1995 (1998) at the 95% C.L. A top quark with $m_{top} = 62$ GeV/c^2 would show up as a 3.1 σ and 4.2 σ discrepancy in $BR(W \rightarrow e\nu)$ in 1995 and 1998, respectively.

Table 9.3: Present and Future Uncertainties in the $BR(W \rightarrow e\nu)$ Measurement

Uncertainty	1988 [24] 4.4 pb^{-1} Uncertainty(%)	This Result 21.7 pb^{-1} Uncertainty(%)	1995 100 pb^{-1} Uncertainty(%)	1998 (Run II) 1 fb^{-1} Uncertainty(%)
Statistics	7.8	2.9	1.2	0.4
Backgrounds				
W	0.7	1.4	0.7	0.5
Z^0	1.6	0.7	0.5	0.2
Acceptances				
Proton Structure	2.5	1.1	0.8	0.5
Boson P_T	0.6	0.2	0.1	0.1
Neutrino Model	-	0.6	0.5	0.5
$O(\alpha_s)$ Diagrams	1.0	0.8	0.4	0.4
Other	0.7	0.4	0.2	0.1
Total Acceptances	2.9	1.6	1.0	0.8
Efficiencies	2.9	1.5	1.0	0.5
'No-jet' Cut	0.5	-	-	-
Total Uncertainty in R	8.8	4.1	2.0	1.2
Theoretical Uncert.	3.0	1.1	1.0	1.0
Total Uncertainty in $\Gamma(W \rightarrow e\nu)/\Gamma(W)$	9.3	4.2	2.2	1.6

The uncertainties in the W width from the transverse mass distribution has been reviewed in Appendix A. With the present data sample, a 16% percent measurement is possible. With the data set expected in 1994-1995, a

7.2% measurement should be possible, better than the 10% uncertainty anticipated after 5 years of data-taking at LEP200. With 1 fb^{-1}, a 2.5% measurement CDF is possible. Perhaps with in combination with the dataset to be accumulated with the larger acceptance of the DØ detector, a measurement approaching 1% is possible, which would begin to be sensitive to the loop effects at the W vertex. The direct measurement of $\Gamma(W)$ should replace the value extracted from R, since only the former is a measurement of the total width. The interesting radiative corrections to the W width affect the effective coupling, g, of the W to fermions, and hence one does not want to have to assume a value for g to obtain the width, as is done in the case of R.

Appendix A

A Direct Measurement of $\Gamma(W)$

As noted in Section 1.2, the W total decay width, $\Gamma(W)$, may be measured from the shape of the transverse mass distribution, $\frac{dN}{dM_T}$, of W events produced in $p\overline{p}$ collisions. This Appendix describes a measurement of $\Gamma(W)$ with this method and the prospects for improvement in the uncertainty of the measurement in future collider runs. The method is sensitive to very different systematic effects than the width determination from the R measurement, so provides a very complementary measurement. Whereas in the R measurement issues such as non-W/Z^0 backgrounds and the boson acceptances were paramount, here biases from selection criteria and the resolution of the detector for the transverse mass are of greater importance.

A.1 Selection of Dataset for W Width Measurement

Many of the electron selection criteria used at CDF are biased against electrons which Bremsstrahlung and also against extremely high-P_T electrons. The electrons from W's can fail the Had/EM cut as the high-P_T electrons leak more into the hadronic compartment. They can also fail calorimeter isolation, E/p, χ^2_{strip}, δx, and δz cuts, since higher P_T electrons can radiate more energetic photons that alter the shapes of these variables. Figure A.1 shows that the efficiency of some of the electron identification cuts

used in the W and Z^0 cross section measurement *vs.* the electron E_T. These varying efficiencies can cause biases when we determine $\Gamma(W)$ from the transverse mass shape, and so must be avoided.

For this direct measurement of $\Gamma(W)$, we select W events with as few selection cuts on the electron as possible, exploiting the event topology of W's. Furthermore, since the width information comes from events with $M_T > M_W$, we may make higher kinematic cuts to suppress the non-W backgrounds (see Chapter 5). The cuts are summarized in Table A.1:

Table A.1: Selection Criteria for W Dataset

Electron $E_T > 30$ *GeV*
Electron $P_T > 13$ *GeV/c*
$\not{E}_T > 30$ *GeV*
Had/EM $< 0.055 + 0.045 \times \frac{E}{100}$
track isolation, *Iso(trk)* < 5 *GeV*
$\lvert Z_{vertex} \rvert < 60$ cm
E_T(out-of-time) < 100 *GeV*

The track isolation is the scalar sum of the P_T of CTC tracks within a cone of $\Delta R = 0.25$ in η-ϕ space around the electron track. The out-of-time energy is measured in the CHA and is time-stamped by TDC's in this calorimeter. There are 10845 events passing these cuts. All possible trigger paths are allowed to feed this dataset, unlike in the cross section analysis, so as to guarantee no trigger bias at high values of M_T. The triggers which can feed this dataset require either an electron, $\not{E}_T$, a jet, or combinations of these three. The transverse mass of these events is shown in Figure A.2.

To reject events from $Z^0 \rightarrow e^+e^-$ decays, where one electron is detected and the other is lost in the calorimeters, we reject events which satisfy the cuts listed in Table A.2. A total of 93 events are discarded. Figures A.3 and A.4 show the invariant mass of the events with a second lepton candidate found. Also shown are the variables with which the Z^0 events are identified.

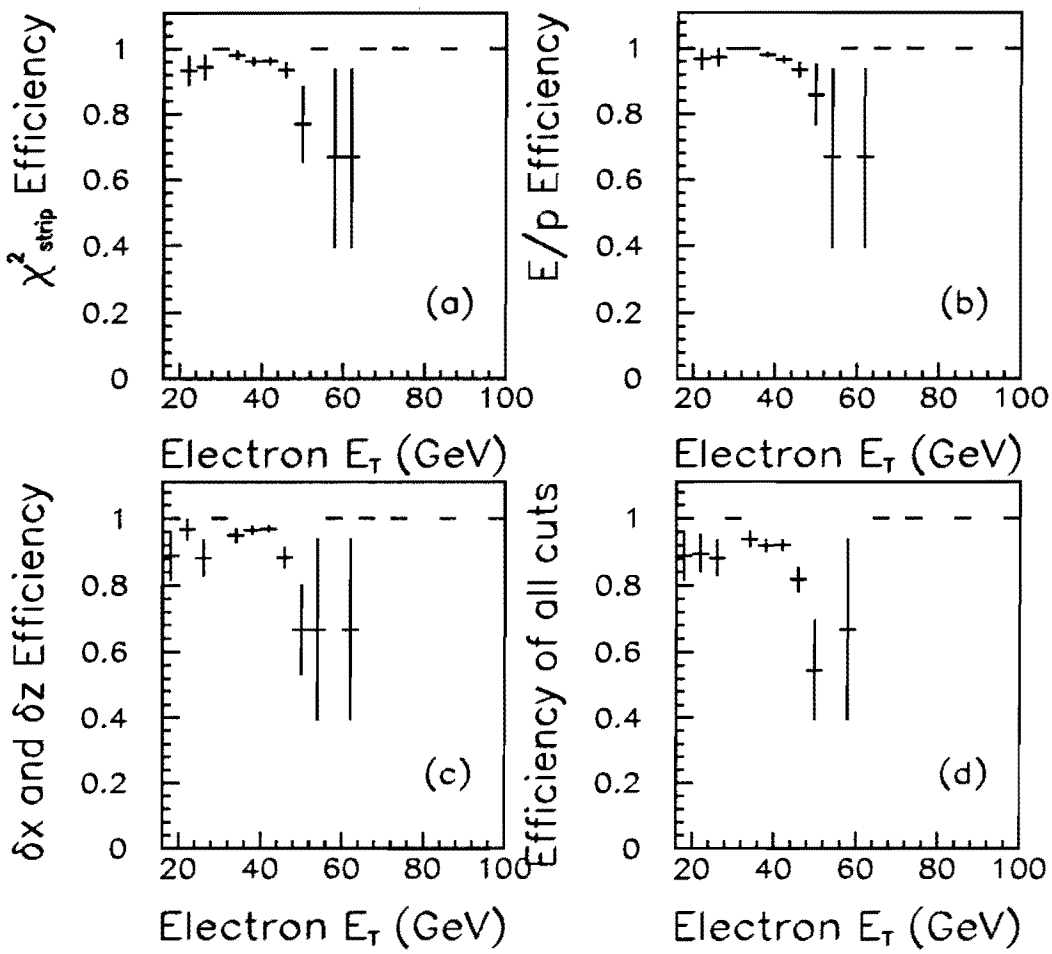

Fig. A.1: Efficiency of three electron identification variables *versus* the E_T of the electron: (a) χ^2_{strip}, (b) E/p, and (c) δx and δz, and (d) all of the above cuts. The efficiencies are obtained from an unbiased sample of electrons from $Z^0 \rightarrow e^+e^-$ decays, where no ID cuts are used to select the second electron.

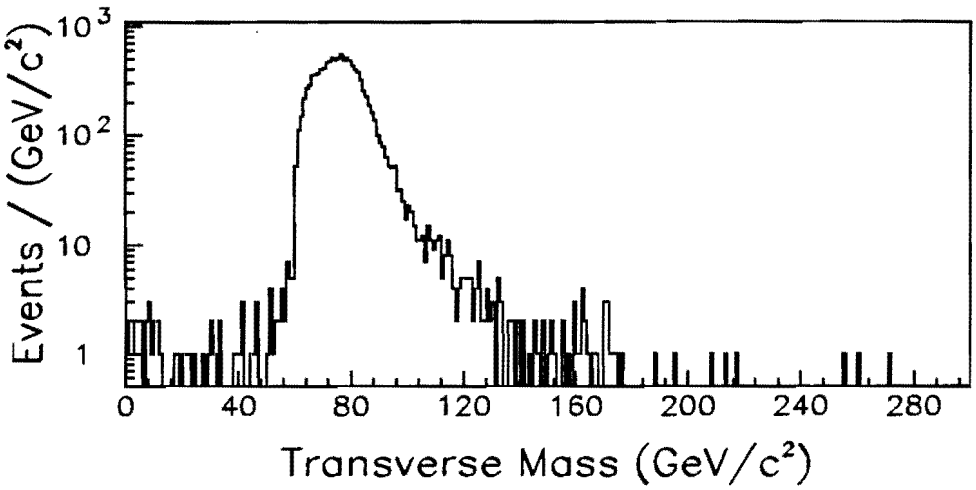

Fig. A.2: Transverse mass distribution for all $W \rightarrow e\nu$ candidates. The 10845 events in the plot pass all of the cuts in Table A.1.

Table A.2: Selection Criteria to Remove Z^0 Events from the W Sample.

Events with a Second CTC Track Passing...	Events with a Second Calorimeter Cluster Passing...
$P_T^{(2)} > 10\ GeV/c$	$E_T^{(2)} > 10\ GeV$
Opposite Sign to First Electron	Had/EM < 0.1
$Iso(trk) < 0.06 \times P_T^{(2)}$	Calorimeter $Iso < 0.1 \times E_T^{(2)}$
EM fraction in Calorimeter > 0.8	$\chi^2_{3\times3} < 5$ (if in PEM)
$\lvert\Delta z\rvert$ between tracks < 8 cm	$76 < M_{(ee)} < 106\ GeV/c^2$

Because of the fewer cuts used to select the electron, a greater background from hadron jets can be expected, where one jet is identified as an electron and the other is either mismeasured or is not detected, creating $\not\!\!E_T$. We have developed a simple set of cuts to remove these events with high efficiency for background and low removal for W signal. The basis for the removal cuts is that, while the second, mismeasured jet may not be observed in the calorimeters, it may still be observed as a cluster of high-P_T tracks in the CTC which point to an uninstrumented region of the calorimeter. The uninstrumented regions of the detector are near $|\eta| \approx 0$ and $|\eta| \approx 1.1$.

In our jet removal algorithm, seed tracks with $P_T > 5\ GeV/c$ are searched for within $\Delta\phi < 90°$ of the $\not\!\!E_T$ vector. A cluster of tracks is formed by summing all of the tracks within a $\Delta R = 0.4$ cone in η-ϕ space around the seed track (the track origins at the beam pipe must be within 5 cm of the seed track's position). Track clusters with $|\eta| < 0.12$ or with $0.85 < |\eta| < 1.4$ and with $cos(\Delta\phi) > 0.95$, where $\Delta\phi$ is the angle between the $\not\!\!E_T$ vector and the total P_T vector of the track cluster, are rejected as dijets. A total of 226 events are removed by this cut. Figure A.5 shows (a) the P_T of the found track clusters, (b) the collinearity of these clusters with the $\not\!\!E_T$ vector, and (c) their distribution in η.

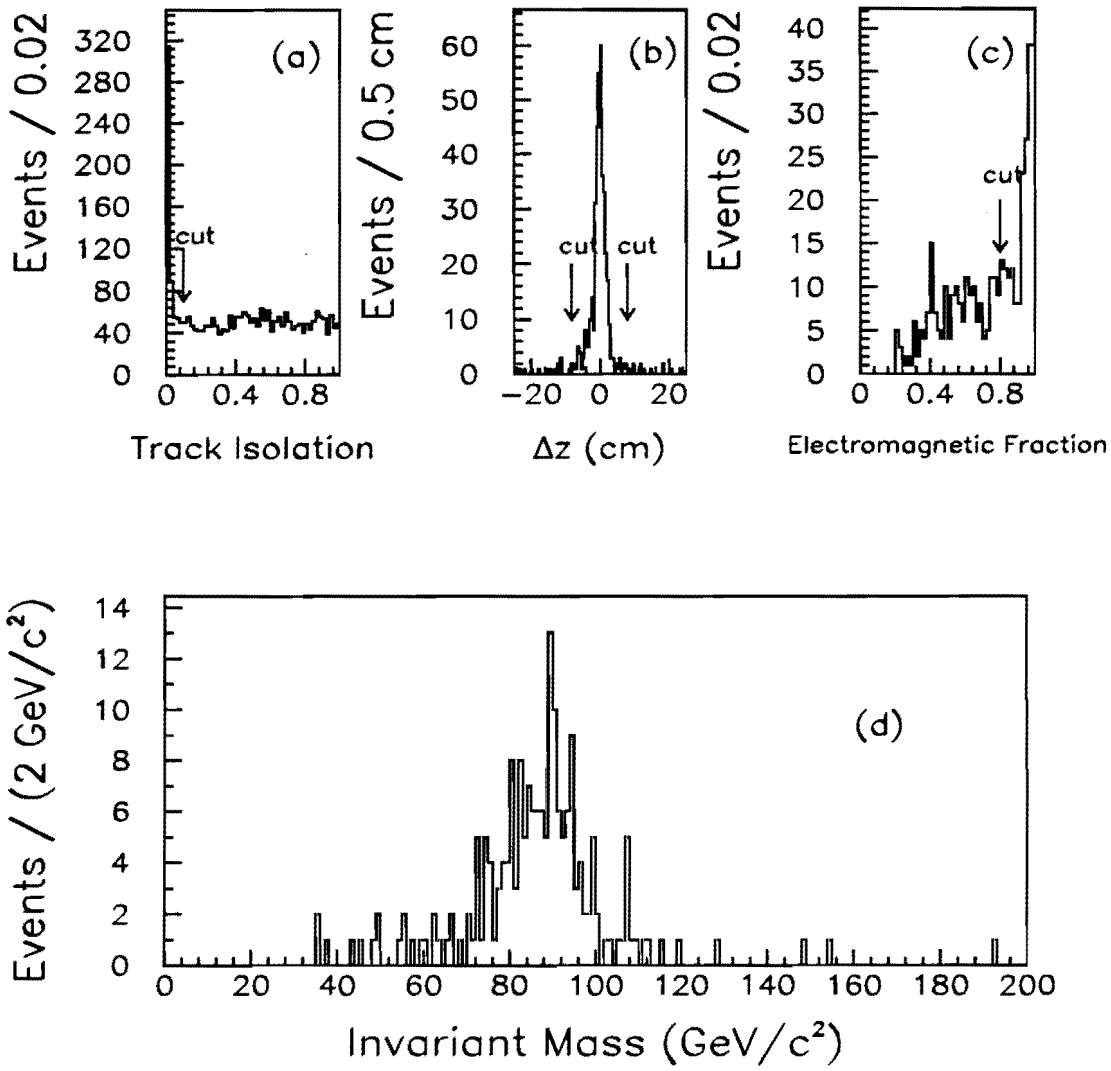

Fig. 3: Variables used to remove $Z^0 \rightarrow e^+e^-$ decays from the W sample. Events in these plots pass the W cuts (Table 1) and have a second, opposite sign track with $P_T > 10$ GeV/c: (a) Track Isolation near the second track (here defined as sum P_T in a cone near the second track divided by the second track P_T); (b) Δz between the "W electron track" and the second track at the beamline (after the track isolation cut); (c) electromagnetic fraction of the calorimeter cluster (if one is observed) to which the second track points (after *iso* and Δz cuts); (d) Invariant Mass of the electron and the second track. In (d) the mass has a long, low-side tail due to Bremsstrahlung radiation by the second track (see Figure 5.11).

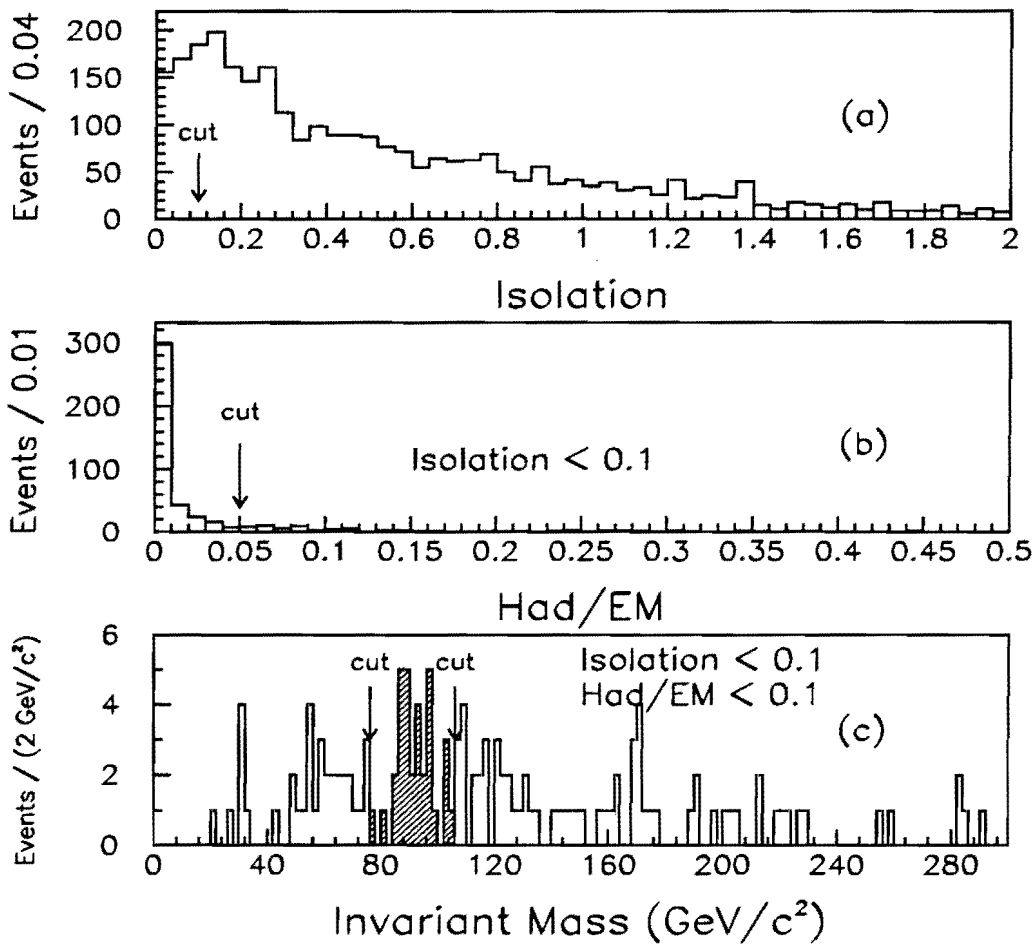

Fig. A.4: Variables used to remove $Z^0 \rightarrow e^+e^-$ decays from the W sample. Events pass the W cuts (Table A.1) and have a second electromagnetic calorimeter cluster with $E_T > 10$ GeV: (a) Calorimeter Isolation of the second cluster; (b) Had/EM of the second cluster (after the *iso* cut); (c) Invariant Mass of the electron and second cluster. The shaded bins are removed as likely $Z^0 \rightarrow e^+e^-$ decays. From the invariant mass sidebands, there are $\approx$ 20 too many events removed.

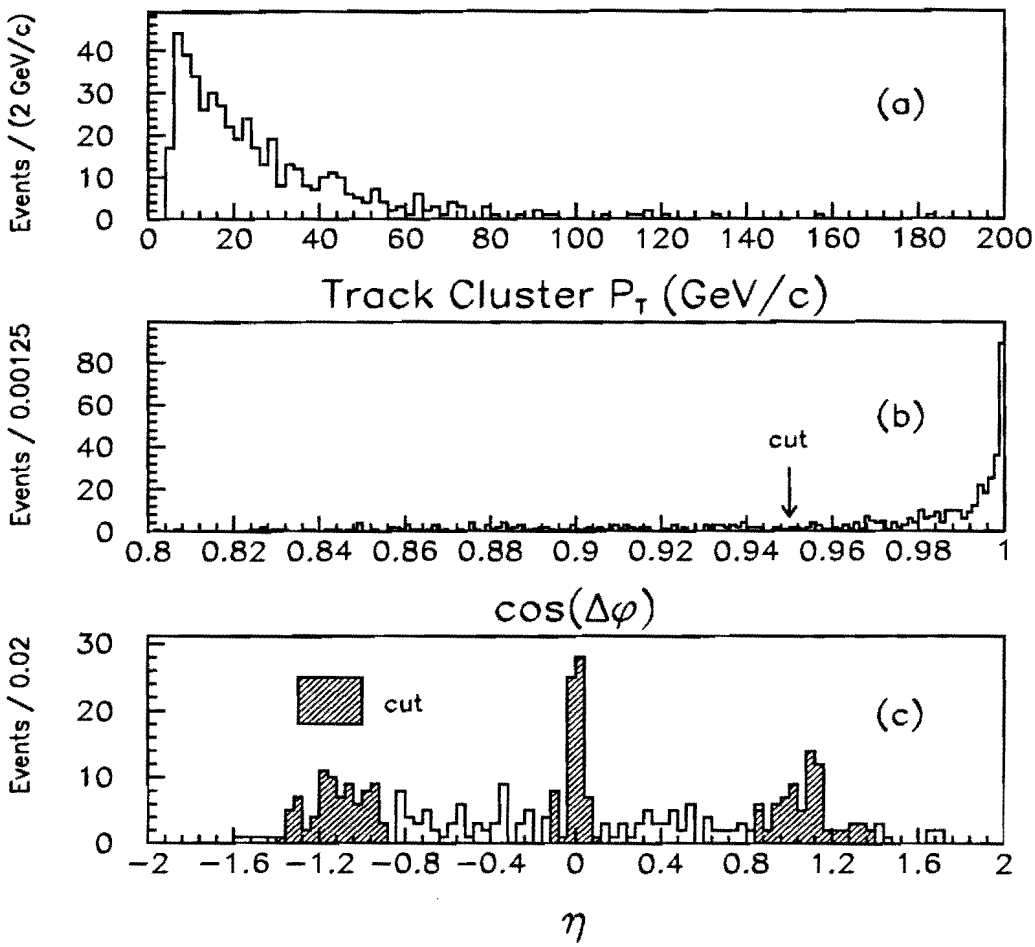

Fig. A.5: Variables used to remove *QCD* dijets from the *W* event sample. All events in these plots pass the *W* cuts in Table A.1. (a) the P_T of the clusters of tracks besides the electron jet; (b) cosine of the angle between the cluster of tracks and the $\not{E}_T$ vector; and (c) the distribution in η of those track clusters near the $\not{E}_T$ vector in ϕ.

A.2 Backgrounds

The principal backgrounds to the W sample are QCD dijets, $Z^0 \rightarrow e^+e^-$ decays, where one electron is lost in the calorimeters to create $\not{E}_T$, and the process $W \rightarrow \tau\nu \rightarrow e\nu\nu$. In this section, we estimate the magnitude of these backgrounds and their transverse mass shapes.

A.2.1 $Z^0 \rightarrow e^+e^-$

We estimate the number of $Z^0 \rightarrow e^+e^-$ decays contaminating the W sample using the ISAJET Monte Carlo and a detector simulation. In the R analysis, ISAJET predicted well the number of $Z^0 \rightarrow e^+e^-$ decays in which the second electron could be observed using the second track. Here, we estimate the acceptance for $Z^0 \rightarrow e^+e^-$ decays to contaminate the W sample (including that they must pass the Z^0 removal cuts), and normalize to the measured cross section $\sigma \cdot B(p\overline{p} \rightarrow Z^0 \rightarrow e^+e^-)$. We find the number of Z^0 background candidates remaining in the W sample to be 39 $\pm$ 8 events. Alternatively, if we normalize to the number of events removed from the W sample by the Z^0 removal cuts, we find that the number of Z^0 events remaining is 54 $\pm$ 5 events. We take the average of these two estimates to be 50 $\pm$ 15 Z^0 events contaminating the W sample. The transverse mass shape of this background (see Figure A.6(a)) is obtained from ISAJET.

A.2.2 $W \rightarrow \tau\nu$

The background from $W \rightarrow \tau\nu$ is similarly estimated using ISAJET. Normalizing to the measured cross section $\sigma \cdot B(p\overline{p} \rightarrow W \rightarrow e\nu)$ (which is the same as for $W \rightarrow \tau\nu$), and factoring an additional 18% for the $\tau \rightarrow e\nu\nu$ branching ratio, we find that the background from $W \rightarrow \tau\nu$ is 150 $\pm$ 45 events. The transverse mass shape of this background (see Figure A.6(b)) is obtained from ISAJET.

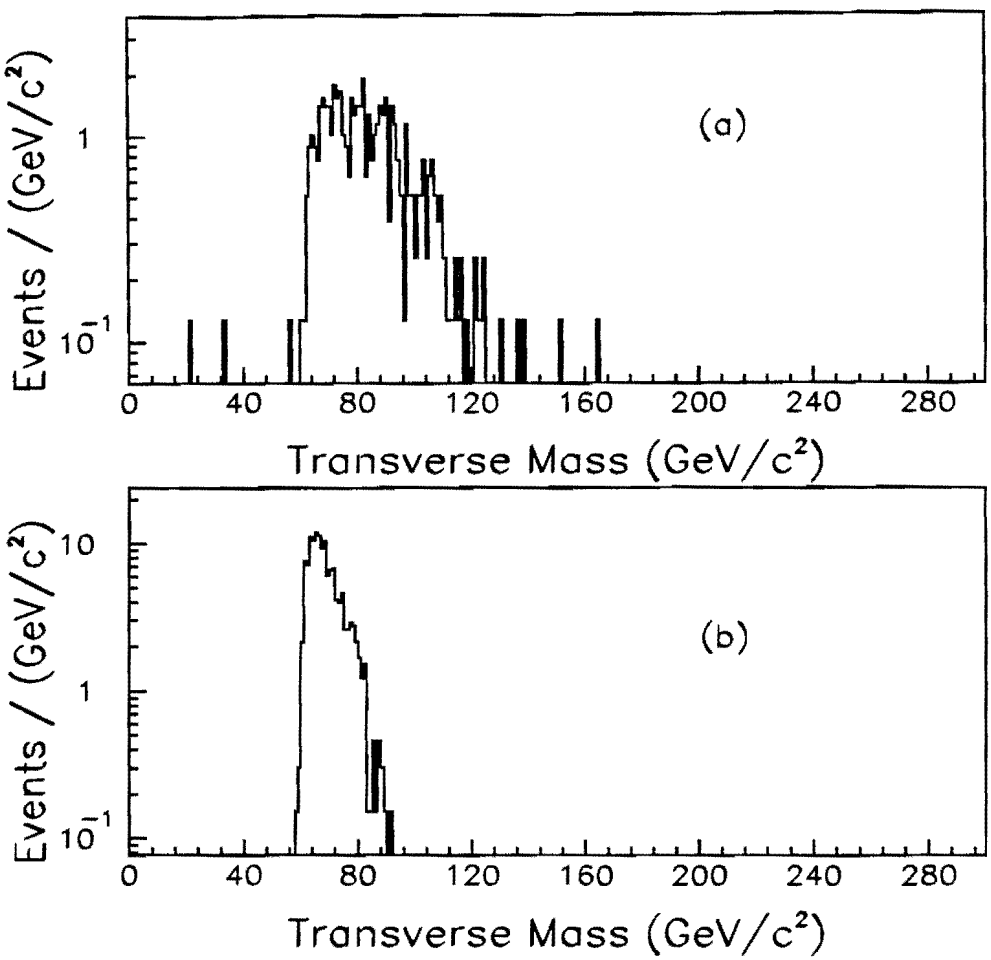

Fig. A.6: Transverse mass shape of the backgrounds from decays of electroweak bosons that get into the W sample, estimated from ISAJET Monte Carlo and a detector simulation. The shapes are normalized to the expected number of events in the W sample: (a) $Z^0 \rightarrow e^+e^-$ decays; and (b) $W \rightarrow \tau\nu \rightarrow e\nu\nu$ decays .

A.2.3 QCD Dijets

The magnitude and shape of this background is estimated from the data. We study this background using a sample of events with non-isolated electrons and $\not{E}_T$, in which the "electron" has $Iso(trk) > 6\ GeV$ and $E_T > 30\ GeV$, and in which $\not{E}_T > 30\ GeV$. These events are presumably dijets. A total of $N^{Tot}_{Bckgd} = 6466$ events make up this background sample. Figure A.7(a) shows the transverse mass of these events. Using our jet removal algorithm (see Section A.1) a total of $N^{Tag}_{Bckgd} = 2732$ of the $N^{Tot}_{Bckgd} = 6466$ events in this sample are identified as dijets. This leaves $N^{No\text{-}tag}_{Bckgd} = 3734$ events untagged as dijets in the background sample. Figure A.7(b) shows the transverse mass shape of the events identified and not identified as dijets in this sample using this technique.

We may normalize the background transverse mass shape to the W signal region by using the number of dijets, N^{Tag}_{W}, removed from the W signal. A total of 226 events were removed from the W sample (see Section A.1) using the dijet cuts. This is not the same as the number of dijets removed from the W sample, however, since some of the events removed were W's. We estimate from the false tag rate that 50 ± 20 W's are falsely tagged as dijets. So, we estimate the number of dijets removed from the W sample is $N^{Tag}_{W} = 176 \pm 20$. The number of dijets left in the sample may then be estimated as:

$$\begin{aligned} N^{No\text{-}tag}_{W} &= N^{Tag}_{W} \times (N^{No\text{-}tag}_{Bckgd} \ / \ N^{Tag}_{Bckgd}) \\ &= (176 \pm 20) \times (3734/2732) \\ &= 241 \pm 40 \end{aligned}$$

dijet events remaining in the W sample. For the transverse mass shape of this background we use the un-tagged dijets in the background sample (see Figure A.7(b)).

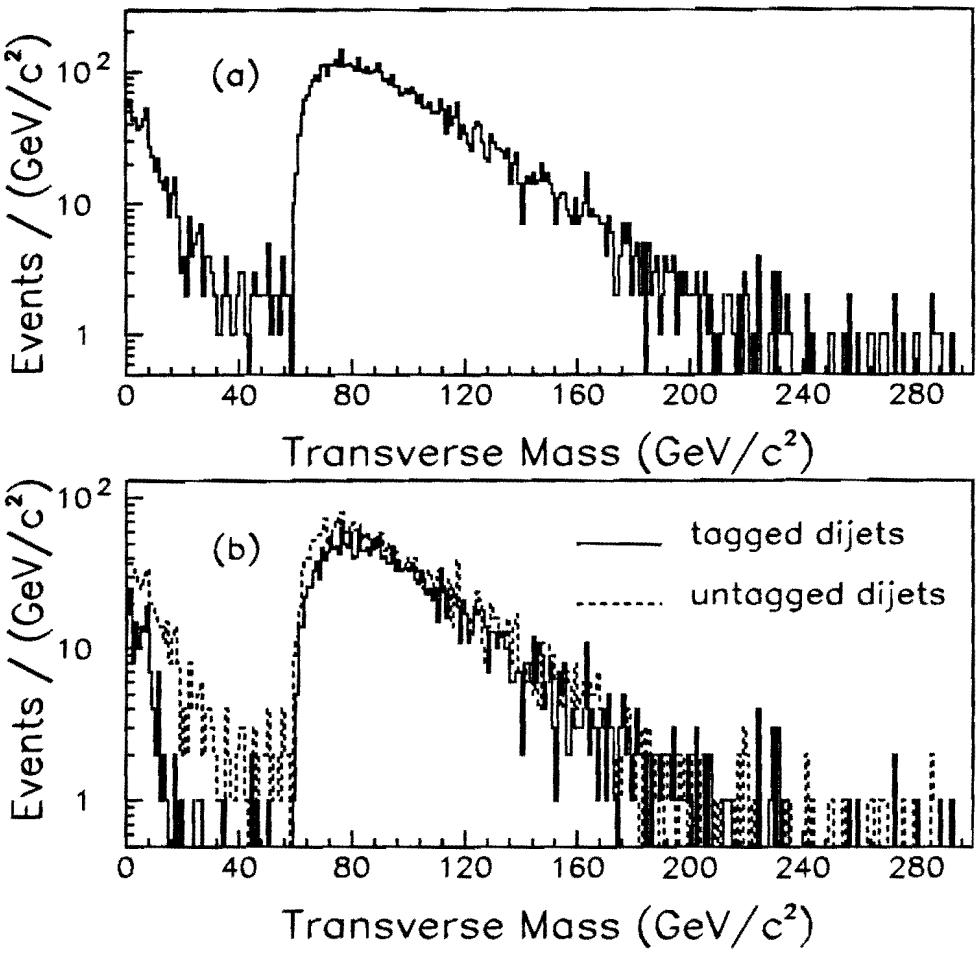

Fig. A.7: (a) Transverse mass shape of the *QCD* dijet background sample described in Section A.3.3. (b) Transverse mass shapes of the events in the background sample that are tagged and those that are not tagged as dijets by the identification algorithm of Section A.1.

A.3 Kinematic Cuts to Reduce W Width Uncertainties

As mentioned in the Section 1.2, the transverse mass distribution is invariant to first order in β, where[59] $\beta^2 = (1+\frac{M_W^2}{P_T^2})^{-1}$ is the W velocity in the transverse plane. The W velocity β, or the W P_T, does alter the M_T distribution at second order. Very high-P_T W's are boosted to the region $M_T > M_W$, which is the region in which we hope to be sensitive to $\Gamma(W)$. Furthermore, because the W P_T distribution that is input to the Monte Carlo has its own measurement uncertainties, we expect some uncertainty in our ability to predict the transverse mass distribution due to the W P_T. Figure A.8 shows the expected variation in the transverse mass distribution in the Monte Carlo from the W P_T, and also the variation expected from $\pm$ 200 MeV changes in $\Gamma(W)$. These variations due to the P_T lead to a 700 MeV uncertainty in $\Gamma(W)$.

Figure A.9 shows the transverse mass distribution for the 10526 W candidates, along with the expected contribution for the backgrounds described above and the expected shape from the Monte Carlo. In the region $M_T > 110$ GeV/c^2, beyond the falling edge of the resolution and where high-events are due primarily to the W lifetime, the background is expected to be $\approx$ 50% of the observed signal, rather high for purposes of our measurement.

Both of the above systematic effects can be reduced with a simple kinematic cut on the P_T of the W: we require $P_T^W < 20$ GeV/c. A total of 9701 events in the data survive this cut. As shown in Figure A.10, the Monte Carlo indicates that, at least qualitatively, the uncertainty due to the W P_T is now comparable to the variation from $\pm$ 200 MeV changes in $\Gamma(W)$. As well, the non-W background at high M_T is reduced, since much of that background has high-P_T (see Figure A.11). The background in the tail goes from $\approx$ 50% without the P_T^W cut to 10% afterwards. Figure A.12 shows the transverse mass distribution of the W's after the P_T^W cut. As a cross-check that the $P_T^W < 20$ GeV/c cut is well-modeled in the Monte Carlo and the background calculations, we show in Table A.3 the estimated W cross section, before and after the P_T^W cut. Also shown is the cross section from the R analysis.

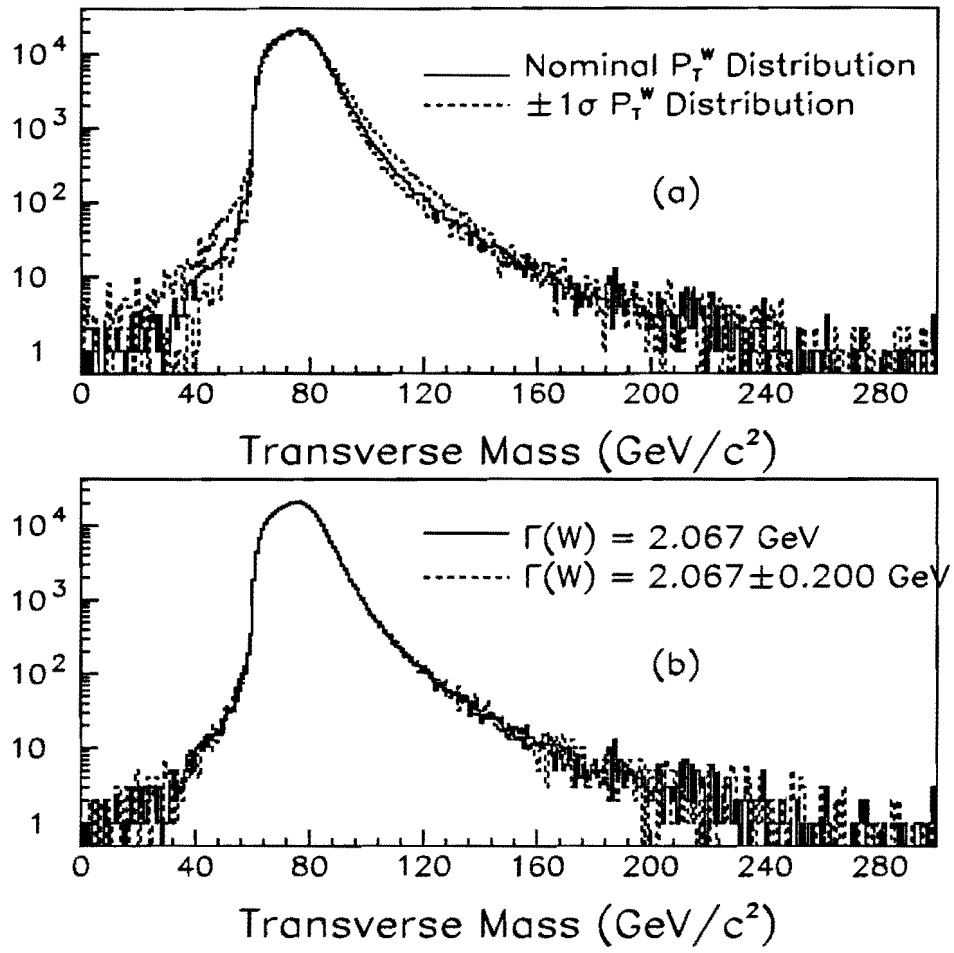

Fig. A.8: Expected variation in the transverse mass distribution in the Monte Carlo, with no W P_T cut imposed, due to:

(a) the uncertainty in the $\frac{dN}{dP_T}$ distribution which is input to the Monte Carlo,

(b) $\pm$ 200 MeV changes in the W width, $\Gamma(W)$.

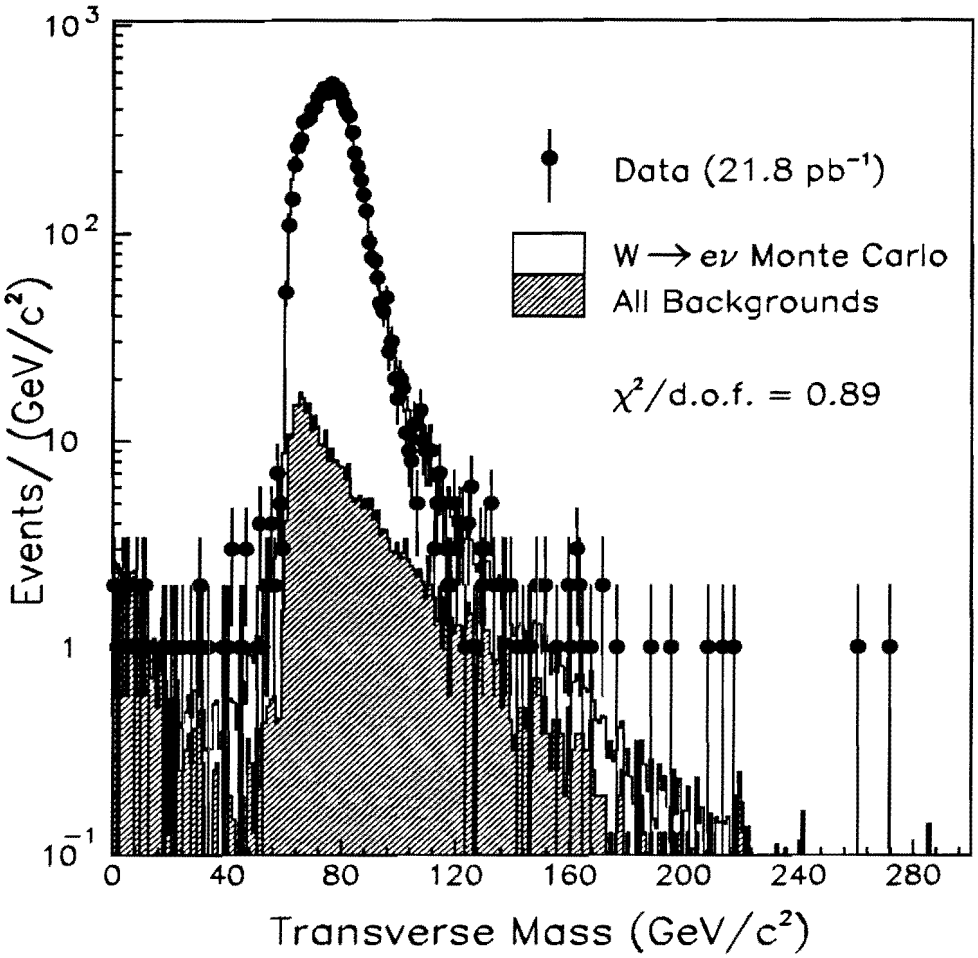

Fig. A.9: Transverse Mass distribution of the 10526 W candidates, along with the expectation for the background and the expected W shape from the Monte Carlo. No P_T^W cut is imposed. In the Monte Carlo, $\Gamma(W) = 2.067$ GeV was used.

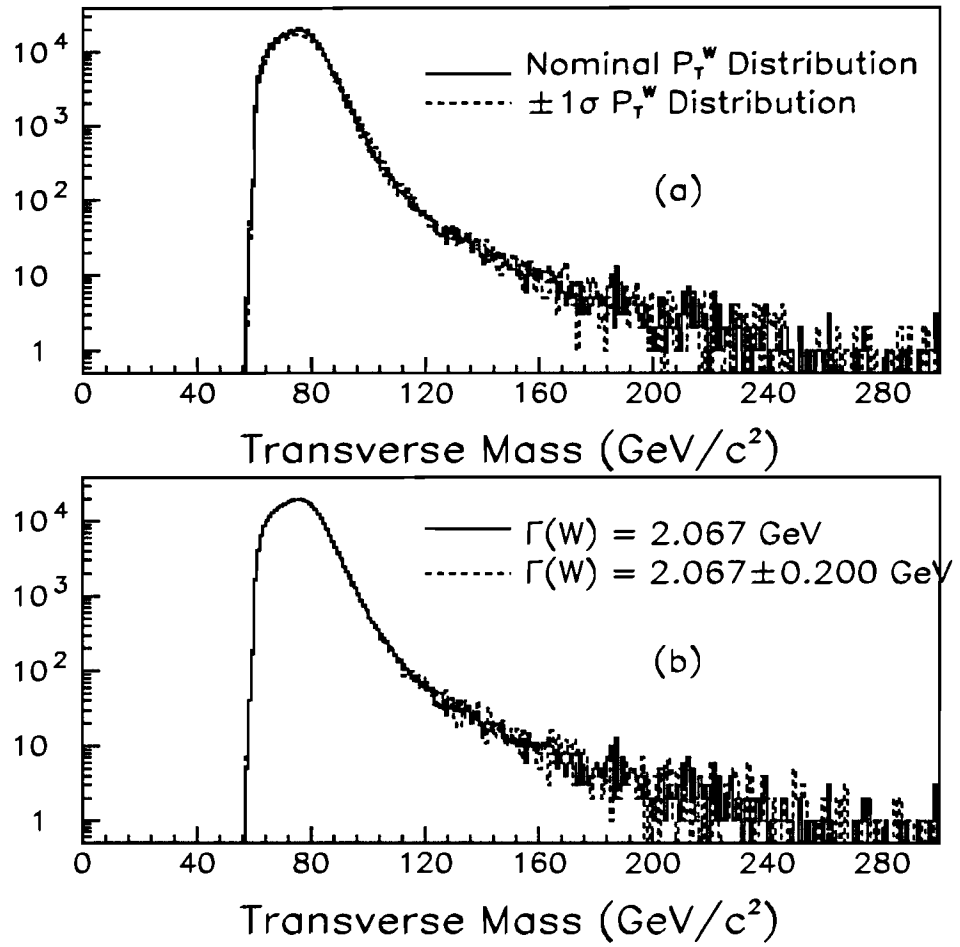

Fig. A.10: Expected variation in the transverse mass distribution in the Monte Carlo, with a cut of $P_T^W < 20$ GeV/c imposed, due to:

(a) the uncertainty in the $\frac{dN}{dP_T}$ distribution which is input to the Monte Carlo,

(b) $\pm$ 200 MeV changes in the W width, $\Gamma(W)$.

Note that the P_T^W cut removes events with $M_T < 50$ GeV/c^2.

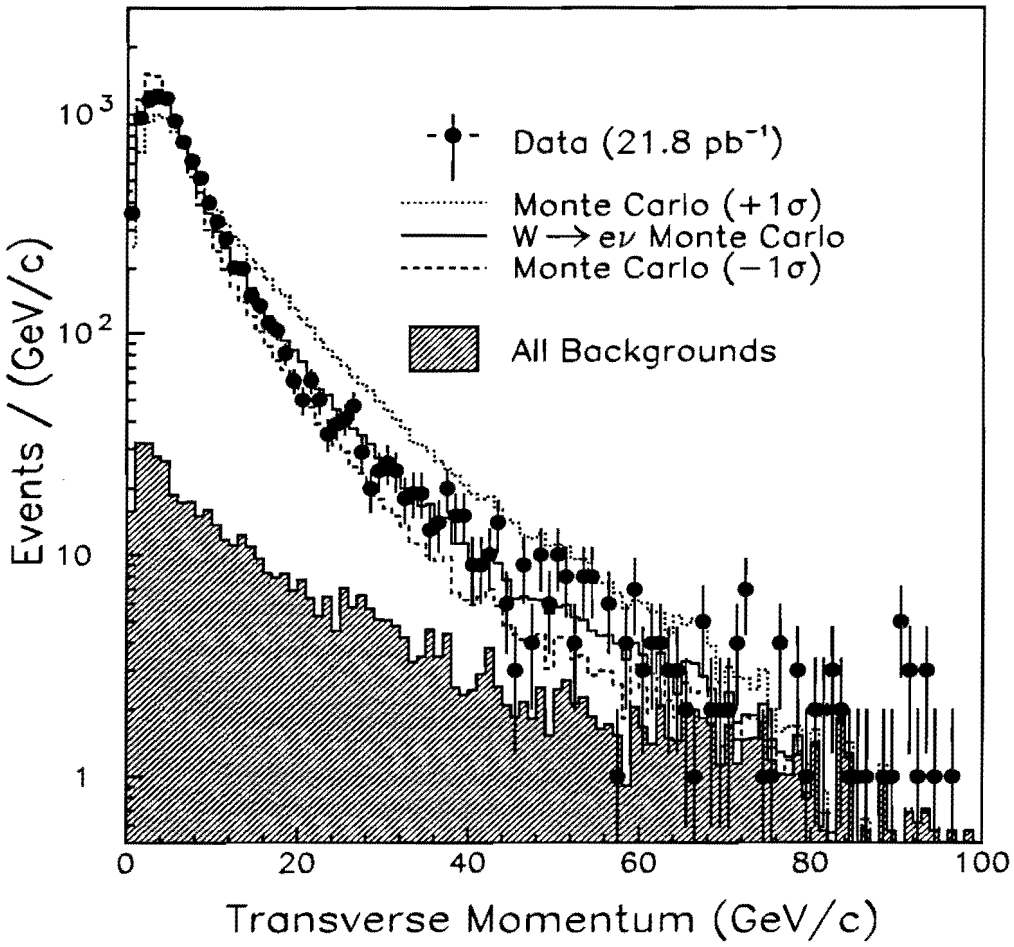

Fig. A.11: Transverse momentum distribution of the 10526 W candidates, along with the expectation for the background and the expected W shape from the Monte Carlo. The $\pm$ 1σ bounds on the Monte Carlo are also shown, where the σ is due to the uncertainty on the P_T^W shape input to the Monte Carlo.

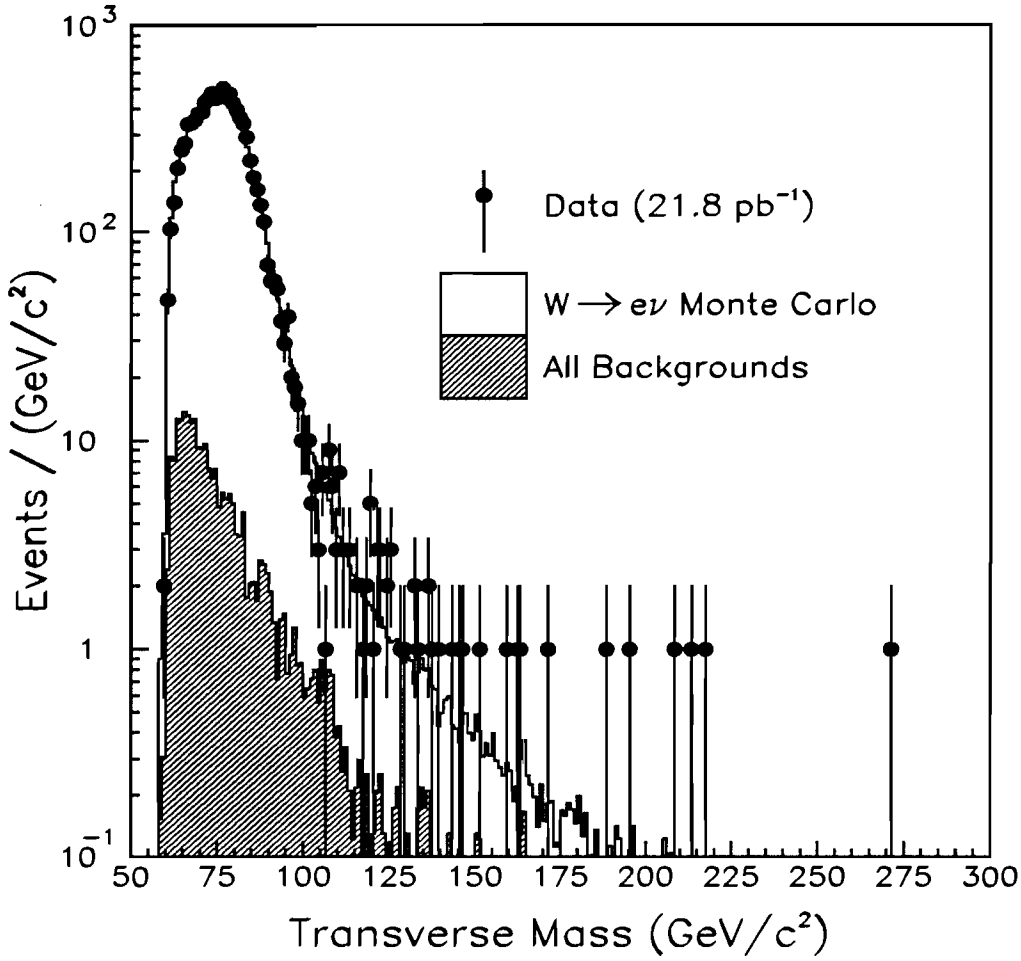

Fig. A.12: Transverse Mass distribution of the 9701 W candidates surviving a cut of $P_T^W < 20$ GeV/c, along with the expectation for the background and the expected W shape from the Monte Carlo. In the Monte Carlo, $\Gamma(W) = 2.067$ GeV was used. Note that the P_T^W cut removes events with $M_T < 50$ GeV/c^2.

Table A.3: Comparison of W Cross Section Using R and W Width Samples

	R Analysis	This Analysis (no P_T^W cut)	This Analysis ($P_T^W < 20\ GeV/c$)
W Candidates	13796	10526	9701
Background	1700 ± 165	441 ± 62	224 ± 44
W Signal	12096 ± 117 ± 165	10085 ± 103 ± 62	9477 ± 99 ± 44
A_W [a]	0.342 ± 0.008	0.217 ± 0.006	0.203 ± 0.006
ε_W [b]	0.725 ± 0.011	0.937 ± 0.010	0.938 ± 0.010
Luminosity	21701 nb^{-1}	21787 nb^{-1}	21787 nb^{-1}
$\sigma \cdot B(W \rightarrow e\nu)$ [c]	2.25 ± 0.02 ± 0.06	2.27 ± 0.02 ± 0.07	2.28 ± 0.02 ± 0.07

[a] Assuming $\Gamma(W) = 2.067\ GeV$.
[b] Including vertex cut efficiency
[c] No luminosity uncertainty included

A.4 Determination of the W Width

A.4.1 Method

The sensitivity to the W width comes from the events with $M_T >> M_W$. The events in the region 80 $GeV/c^2 \lesssim M_T \lesssim 110\ GeV/c^2$ (see Figure A.12) are dominated by the calorimeter resolution. Little sensitivity to $\Gamma(W)$ can come from this region because of the still non-negligible variations in the transverse mass shape due to the W P_T distribution uncertainty, as shown in Figure A.10. The sensitivity to $\Gamma(W)$ comes from the region $M_T > 110\ GeV/c^2$.

The W width will be determined by performing a fit of the $\frac{dN}{dM_T}$ distribution in the data to Monte Carlo templates with different values of $\Gamma(W)$. The fit will be performed over the region $M_T > 110\ GeV/c^2$, where the Monte Carlo indicates that the systematic variations in the shape are small. The sources of the systematical uncertainties are discussed below. The fit is a log likelihood where the likelihood is given by

$$\ln \mathcal{L} \equiv \sum_i \left[x_i \cdot \ln(\mu_i) - \mu_i - \ln(x_i!) \right]$$

where the sum is over the bins in the transverse mass distribution, x_i is the number of events observed in each transverse mass bin i, and μ_i is the expected number of events in each bin (both from W signal and remaining non-W backgrounds): $\mu_i = Bckgd_i + W_i$. In the Monte Carlo, the background shape $Bckgd_i$ is normalized to 224 events and the W shape W_i is normalized to 9477 events (see Table A.3).

The results of the likelihood fit are shown in Figure A.13. The fit favors a value of $\Gamma(W) = 2.04 \pm 0.28$ GeV, where the uncertainty is statistical only. This statistical uncertainty is determined by the point where the log likelihood decreases by 0.5. To check that this variation does represent the statistical uncertainty, we have used our Monte Carlo to perform many Monte Carlo "experiments" of 9477 events each. We have verified that the mean $\Gamma(W)$ returned is the same as input to the fit, and that the r.m.s. of the fitted widths is approximately 280 MeV, as shown in Figure A.14. One interesting feature of Figure A.13 is the asymmetric shape of the likelihood curve. The shape has been fit to a cubic polynomial to determine the peak position. The same asymmetric shape is observed in the Monte Carlo, indicating that the uncertainties are non-gaussian and that there is less sensitivity to small values of $\Gamma(W)$.

A.4.2 Systematic Uncertainties

The systematic uncertainties in this determination of the W width are effects with alter the shape of the transverse mass distribution. They are: the P_T^W distribution, the electron resolution, the neutrino resolution, the backgrounds, and the electron energy scale. To estimate the uncertainties due to these effects, we generated Monte Carlo with these input parameters varied and then fit to the original Monte Carlo templates with the nominal parameters. The uncertainties are summarized in Table A.4.

Figure A.15 shows the $\not{E}_T$ smearing in the Monte Carlo and the data for $Z^0 \rightarrow e^+e^-$ decays, where any $\not{E}_T$ in the event is due to the energy response of

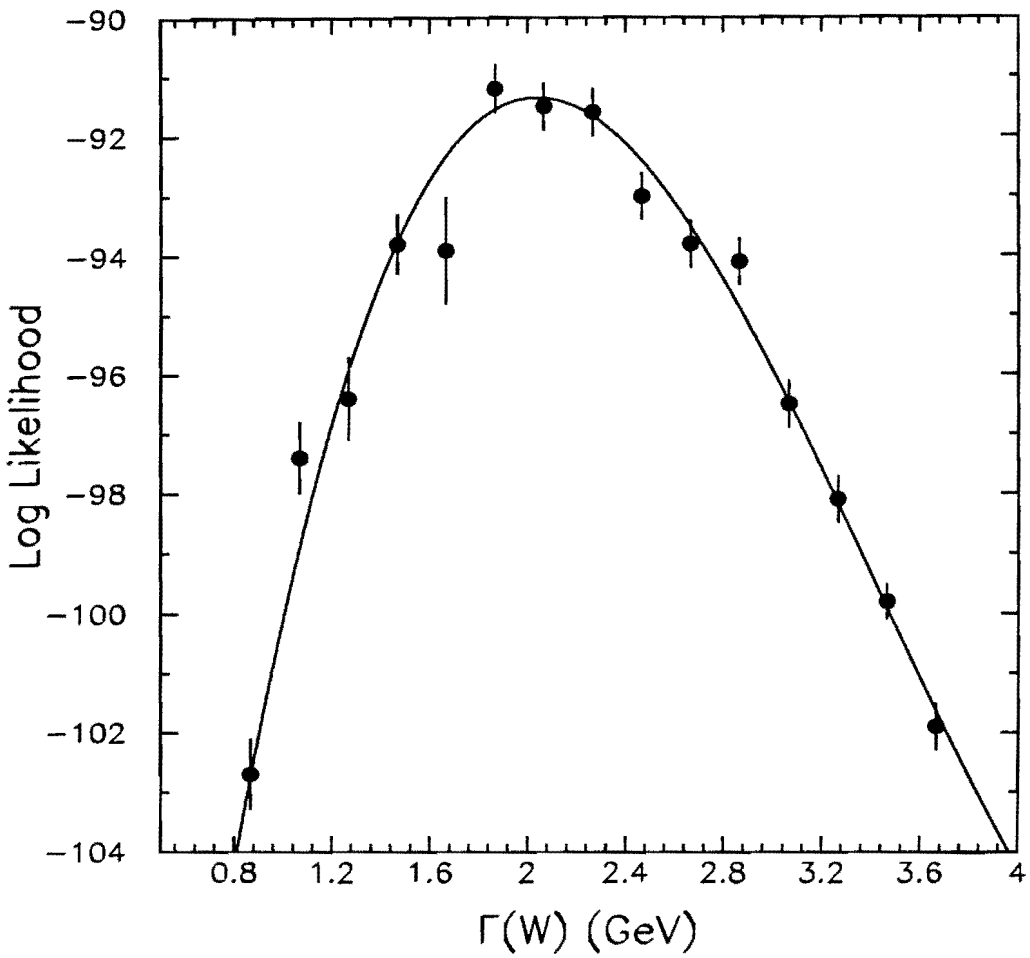

Fig. A.13: Results of the log likelihood fit of the data to Monte Carlo templates of different W widths. Each point represents a log-likelihood fit performed over the range $M_T > 110$ GeV/c^2. The curve is the best fit of the likelihood points to a cubic polynomial. The most likely value is at $\Gamma(W) = 2.04$ GeV.

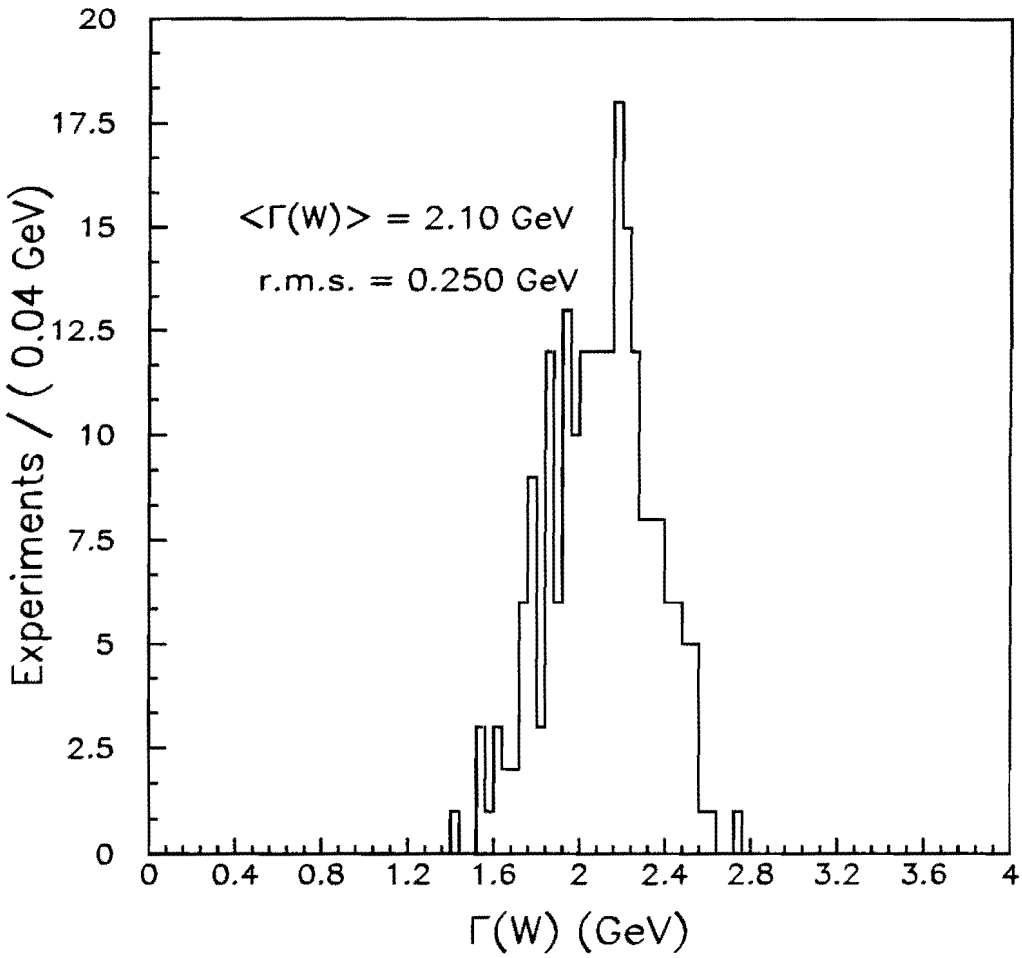

Fig. A.14: Results of the log likelihood fit of 213 Monte Carlo "experiments" of 9477 events each to Monte Carlo templates of different W widths. The Monte Carlo experiments each had a value of $\Gamma(W) = 2.07$ *GeV*, which is consistent with the mean fitted value of the many experiments. The estimated statistical uncertainty of 280 *MeV* from the log likelihood in the data is well reproduced by the r.m.s. of the experiments' results.

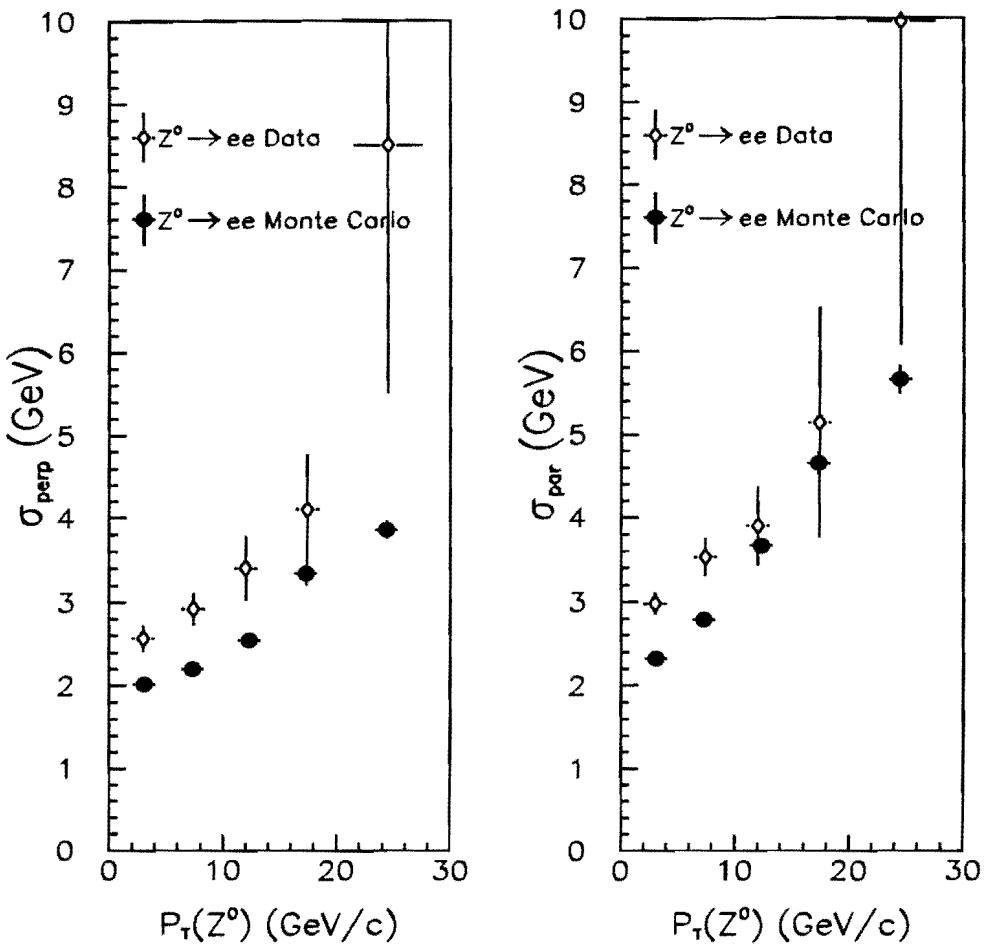

Fig. A.15:The spread on the resolution of the components of the $\not{E}_T$ perpendicular and parallel to the P_T vector of the Z^0 in $Z^0 \rightarrow e^+e^-$ decays, as a function of the Z^0 P_T. Shown is the Z^0 data and the Monte Carlo. The spread on each component is expected to be a gaussian whose sigma grows with boson P_T. The extra smearing in the data is consistent with that due to a minimum bias event present in 40% of the Z^0 events, an effect not present in this Monte Carlo calculation. The Monte Carlo results of Chapter 7 and elsewhere in this Appendix are given additional fudge factors to account for this effect.

the calorimeter, not due to neutrinos. The difference between the Z^0 data and the Monte Carlo is consistent with the expected resolution from 0.4 minimum bias events.[60] The Monte Carlo calculations in all of the above results include an additional fudge factor in the neutrino resolution to reflect the effect of the underlying event. Here, we have allowed this fudge factor to vary within the uncertainties allowed by the Z^0 data. The resulting variations in the W width are found to be 5%, or 100 MeV.

The energy scale of the central calorimeter is determined using $Z^0 \rightarrow e^+e^-$ decays where both of the electrons fall in the central region. The uncertainty due to the energy scale is taken to be the possible variation in the fitted W width when the scale is shifted by $\pm$ 0.4%, the accuracy to which it can be determined with the Z^0's. Allowing the energy scale to vary by this amount in the W Monte Carlo leads to 2.0% variations in the W width.

The energy resolution for electrons is of the form $(\sigma/E)^2 = \frac{(13.5\%)^2}{E_T\ (GeV)} + C_0^2$, where the constant term C_0 is due to tower-to-tower variations in the energy response and variations within cells as a function of shower position. This constant term is measured using the invariant mass width of $Z^0 \rightarrow e^+e^-$ decays, which has a finite width due to the lifetime of the Z^0 and due to the calorimeter resolution. The uncertainty on the electron resolution determined in this way is $\pm$ 1%. Allowing the electron resolution in the W Monte Carlo to vary by this amount leads to 0.6% variations in the W width.

The $\not{E}_T$ and electron resolutions have been assumed to be gaussian. We investigate here the possible effects of non-gaussian tails in the resolution. For the CDF detector, the effects of non-gaussian tails are most pronounced in the $\not{E}_T$ resolution. Studies of minimum bias data (see Figure 2.18) indicate that the σ of the $\not{E}_T$ resolution grows with the ΣE_T in the event. As shown in Figure A.16, the $\not{E}_T$ projection in the x and y directions fit well to a gaussian, but can accommodate a small exponential tail, too. If we insert such tails, with a magnitude and shape as given by the minimum bias data, into the Monte Carlo, this causes a 30 MeV shift in the width. The Monte Carlo indicates that

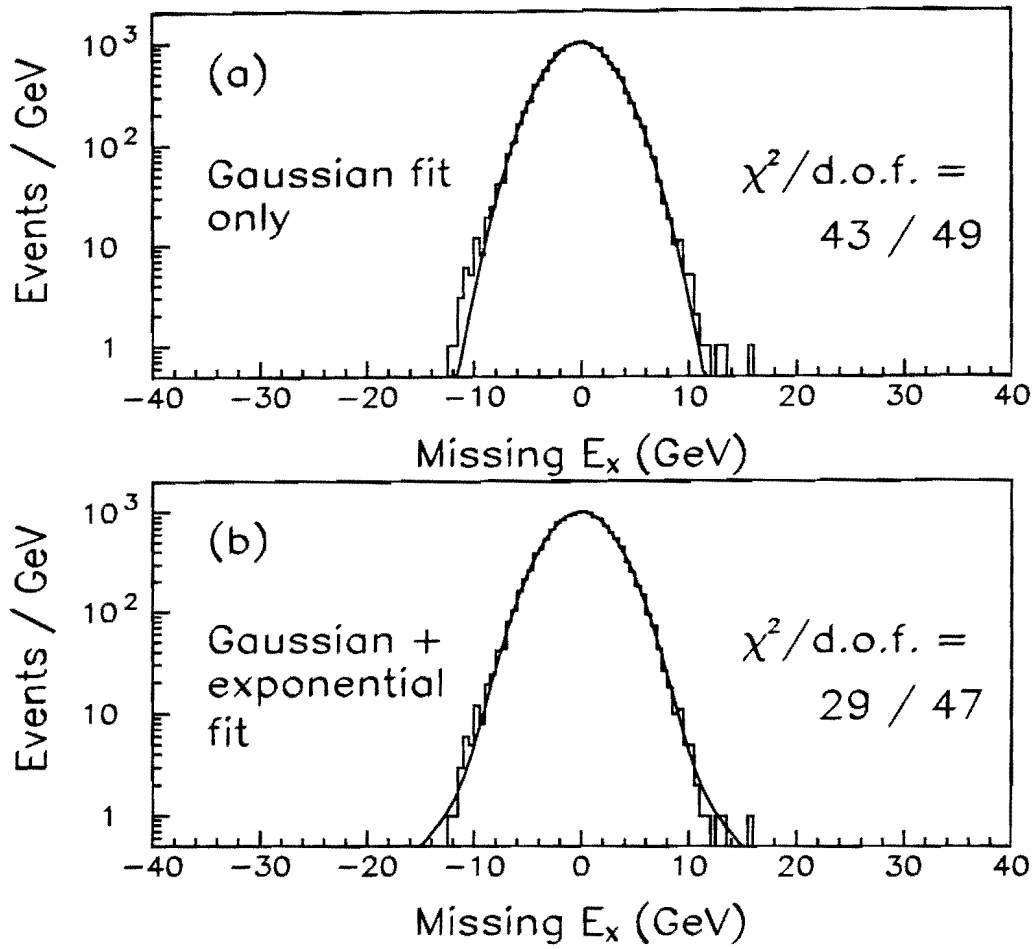

Fig. A.16: The $\not{E}_T$ component in the x direction from minimum bias data, for a typical slice in ΣE_T (this particular slice is 20 $GeV < \Sigma E_T < 25$ GeV): (a) with the best fit of the data to a gaussian only; (b) the best fit to a gaussian plus an exponential is shown. In the latter fit, the amplitude of the exponential is 32 $\pm$ 26 events, consistent with zero. Thus, while the data can accommodate a non-gaussian tail to the resolution, the tails are not statistically significant.

the shift is small because the $P_T^W < 20$ GeV/c cut is equivalent to a 20 GeV/c cut on the magnitude of the smearing. Thus, even if there were non-gaussian tails in the resolution, they are cut away and do not affect the width measurement. Since this is small compared to the previously quoted $\not{E}_T$ uncertainty (added in quadrature one would obtain 104 MeV), and since the tails are only marginally statistically-significant in the minimum bias data, we have assigned no additional uncertainty due to non-gaussian tails in the $\not{E}_T$ resolution.

The P_T^W uncertainty is taken to be half the spread in results obtained between using the 'hard' and 'soft' P_T^W distributions described in Chapter 7. We find a variation of 6%, or 120 MeV, in $\Gamma(W)$ due to variations in the W P_T. Allowing the normalization of the background shape to vary within its estimated uncertainty causes 16 MeV variations in $\Gamma(W)$.

A different kind of P_T^W uncertainty arises because of the theoretical expectation that the P_T^W distribution varies as a function of the mass of the W produced. The P_T^W distribution used in our data was measured predominantly at the W pole, and so it is possible that there is a bias. We have checked this possible source of bias in two ways: in the first way we have fit a Monte Carlo sample with a new P_T^W distribution to the Monte Carlo templates generated with the nominal distribution. The new P_T^W used is of the form[49] $\frac{d\sigma}{dP_T} = (1+\delta)\frac{d\sigma_0}{dP_T}$, where $\frac{d\sigma_0}{dP_T}$ is the nominal P_T^W distribution from the CDF measurement and $\delta \equiv \frac{\alpha_w \times \alpha_s}{P_T^2}\log(\frac{M^2}{P_T^2})$ and M is the possibly off-shell mass of the W produced. The fitted value of this new Monte Carlo sample to the templates yields a value of $\Gamma(W) = 2.089$ GeV as compared to the 2.067 GeV input to the Monte Carlo. This shift of 23 MeV is much smaller than the 120 MeV uncertainty quoted above for the uncertainty in $\Gamma(W)$ due to the W P_T.

In the second test of this possible P_T^W bias, we have performed this analysis once again but with a cut of $P_T^W < 10$ GeV/c. Figure A.17 shows the transverse mass spectrum of the W candidates with this new cut. Presumably if a bias exists, it is either accentuated or diminished by changing the P_T^W cut.

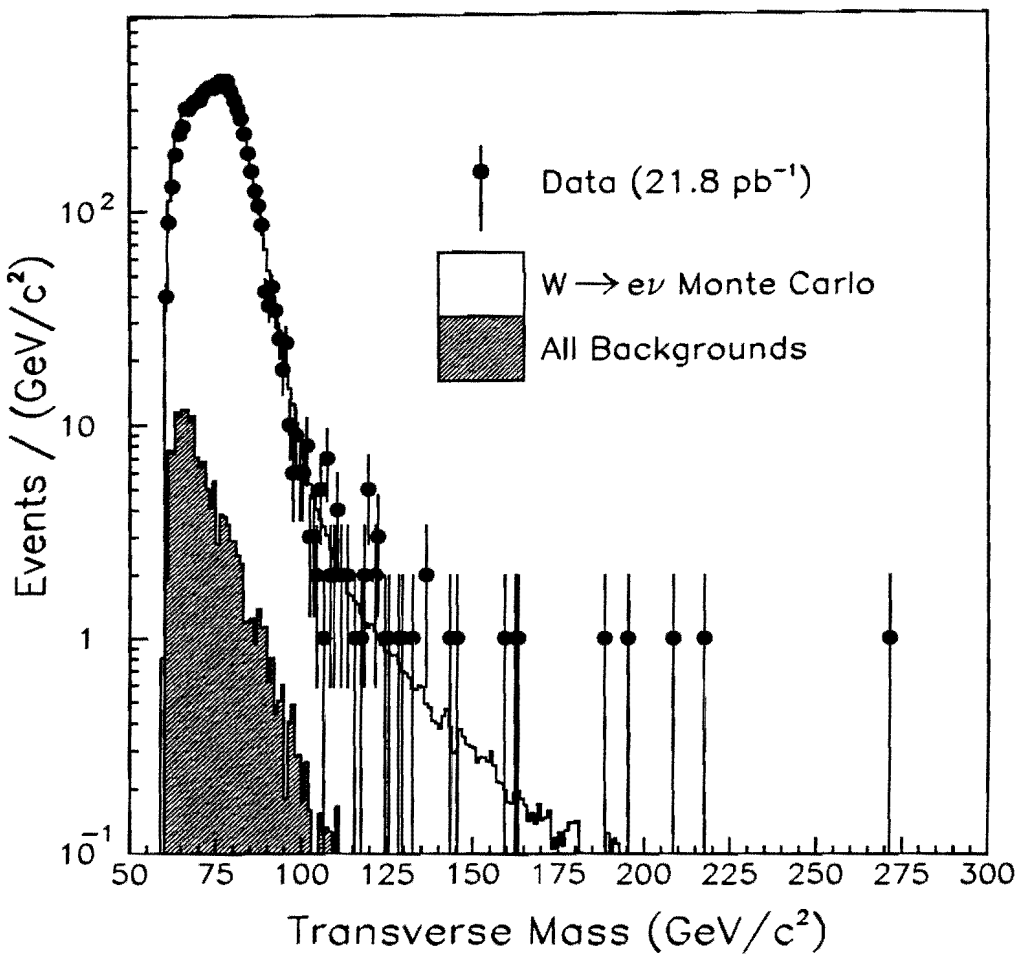

Fig. A.17: Transverse Mass distribution of the 8604 W candidates surviving a cut of $P_T^W < 10$ GeV/c, along with the expectation for the background and the expected W shape from the Monte Carlo. In the Monte Carlo, $\Gamma(W) = 2.067$ GeV was used. Note that the P_T^W cut removes events with $M_T < 50$ GeV/c^2.

Table A.4: Present and Future Uncertainties in the Direct Measurement of $\Gamma(W)$

	This Analysis ($21.8\ pb^{-1}$) Uncertainty (MeV)	Run 1B (1995) ($100\ pb^{-1}$) Uncertainty (MeV)	Run II (1998?) ($1.0\ fb^{-1}$) Uncertainty (MeV)
Statistics	280	124	40
Background	16	12	8
P_T^W	120	54	17
Energy Scale	40	18	6
Electron Resolution	12	12	10
Neutrino Resolution	100	45	14
Total	324	145	48

With this new cut we obtain $\Gamma(W) = 2.04 \pm 0.33(stat.) {}^{+0.10}_{-0.07}(sys.)\ GeV$, where here the interesting feature is that the P_T^W cut is so deep into the data's spectrum (see Figure A.11) that the P_T^W uncertainty has become quite asymmetric. This result has the same central value as the $P_T^W < 20\ GeV/c$ result. Given the small variation seen in these two tests as compared to the estimated uncertainty due the knowledge of the P_T^W shape, we have assigned no additional uncertainty due to the evolution of $P^W{}_T$ with M_W.

Table A.4 summarizes the uncertainties in $\Gamma(W)$. Assembling the results, the final result for the W width is:

$$\Gamma(W) = 2.04 \pm 0.28(stat.) \pm 0.16(sys.)\ GeV.$$

As a check, we have instead fit over the region $M_T > 120\ GeV/c^2$, and have obtained a value for $\Gamma(W)$ of $\Gamma(W) = 2.08 \pm 0.34(stat.) \pm 0.09(sys.)\ GeV$, where the systematic uncertainty is less because the cut-off for the fit is farther from the W mass peak. Note that the $M_T > 110\ GeV/c^2$ sample has 58 events and the $M_T > 120\ GeV/c^2$ sample has 35 events.

Also listed in Table A.4 are the future prospects for these uncertainties. All of the of the systematic uncertainties will scale like the statistical

uncertainty, since they simply require more data to measure. An example of this is the P_T^W shape input to the Monte Carlo. A measurement of P_T^W from the present CDF dataset, for example, could already halve the systematic uncertainty due to P_T^W. Another systematic effect which can be improved is the tower-to-tower calibration which feeds into electron resolution, which is determined from the width of the $Z^0 \rightarrow e^+e^-$ peak. Likewise, the neutrino resolution should improve as the number Z^0's of with which we study the calorimeter response to P_T increases. Ultimately, a measurement with better than 2.5% precision is possible from the CDF data. This analysis could similarly be performed with data from the DØ detector, where in principle the larger angular coverage for electrons and better $\not{E}_T$ resolution would yield a comparable or better result for the W width. Combined, a measurement approaching 1% in precision is possible, which approaches the level of the radiative corrections to the W width. Even this precision can be improved if the threshold for the fit (currently 110 GeV/c^2) can be lowered, which it could be if the W P_T and neutrino resolutions were better understood.

Appendix B

A Note On Calculating the *b* Electron Fraction

This Appendix contains a technical point concerning the calculation of *b* electron fractions, and may not be of interest to every reader. In Chapters 4 and 5 it was desired to use the electron D/σ shape in the SVX to determine the *b* fraction of electrons. The method was in a sense a fit to the D/σ distribution using the number of events in the tails. We discuss the details of the calculation for the non-W/Z^0 electron sample for demonstration. The equation used was:

$$B_{all} = (f_b \cdot B_b) + (f_{conv} \cdot B_{conv}) + [(1-f_{b's} - f_{conv}) \cdot B_{fake}]$$

where f_i (i = b, conversion, or fake) was defined as the fraction of the electron sample considered of type "i," counting electrons both in and outside of the SVX acceptance. The variables B_i were defined as the fraction of type "i" with $|D|/\sigma > 2.0$. Note that $f_{b's} + f_{conv} + f_{fake} = 1.0$. The fraction $f_{conv} = 41.5\%$ was determined in Section 4.2. The variables B_i for the *b*'s, fakes, and conversions, were determined in Section 4.3, as was $B_{all} = 25.9 \pm 0.5$ % for the 8090 electrons in the non-W/Z^0 sample that have an SVX track. Since one has that $f_{b's} = 1.0 - f_{conv} + f_{fake}$, one may in principle solve for $f_{b's}$.

An important correction arises, however, because the acceptance of the SVX is not the same for conversions as it is for "prompt" electrons, like those from pion fakes and *b* decays. Many conversions occur in the material outside the SVX, and thus one does not expect them to have an SVX track (see Figure 4.5). Thus, we may not use the fraction f_{conv} = 41.5% of *all* electrons (in- and outside of the SVX) that are from conversions in the above equation, because the fraction of the N_{all}^{SVX} = 8090 SVX tracks that are from conversions is not 41.5%.

While the acceptance of the SVX for prompt tracks is A_{prompt} = 61% (see Section 2.4.8), the SVX acceptance for conversions is A_{conv} = 26.5 ± 0.7 % (this is determined with the conversion sample described in Section 4.3.2). The fraction of *SVX tracks* ($\equiv F_{conv}$)that are from conversions is really

$$\begin{aligned} F_{conv} &= N_{conv}^{SVX} / N_{all}^{SVX} \\ &= (N_{conv}^{Tot} \times A_{conv}) / N_{all}^{SVX} \\ &= (7387 \times 0.265) \ / \ 8090 \\ &= 24.2 \pm 1.0\%. \end{aligned}$$

If we similarly define $F_{b's}$, F_{fake}, as the fractions of SVX tracks from *b*'s and fakes, we may solve for $F_{b's}$, and F_{fake}, and then scale the fractions up by the SVX acceptances to obtain $f_{b's}$ and f_{fake}. We solve (inserting F_{conv}= 24.2%):

$$B_{all} = (F_b \cdot B_b) + (F_{conv} \cdot B_{conv}) + [(1-F_{b's}-F_{conv}) \cdot B_{fake}]$$

With the numbers in Chapter 4 we obtain $F_{b's}$ = (40.9 ± 4.7) % and F_{fake} = (34.9 ± 5.5) %. Scaling up by the respective SVX acceptances for these categories, we obtain:

$$\begin{aligned} f_{conv} &= 41.5 \pm 2.2 \ \% \\ f_{b's} &= 31.5 \pm 3.7 \ \% \\ f_{fake} &= 27.0 \pm 4.4 \ \% \end{aligned}$$

References

[1] A.H. Compton, Bulletin Nat. Res. Council No. 20, p. 16 (1922); Phys. Rev. **21**, 715 and **22**, 409 (1923). See also A. H. Compton and S. K. Allison, X-Rays in Theory and Experiment, (New York: Van Nostrand), 1935, for a comprehensive review of the early experiements and theories on X-ray radiation.

[2] A. Einstein, Ann. d. Physik **17**, 145 (1905).

[3] E. Fermi, Ric. Sci. **4**, 491 (1933), and Z. Phys. **88**, 161 (1934).

[4] O. Klein, in *Les Nouvelles Théories de la Physique*, Proceedings of a symposium held in Warsaw, 30 May - 3 June 1938 (Institut International de Cooperation Intellectuelle, Paris, 1938) p. 6.

[5] S. Weinberg, Phys. Rev. Lett. **19** 1264 (1967).

[6] A. Salam, *Elementary Particle Theory*, ed. N. Svartholm (Stockholm: Almqvist, 1968), p. 367.

[7] S.L. Glashow, Nucl. Phys. **22** 579 (1961).

[8] L. Rolandi, Proceedings of the XXVI International Conference on High Energy Physics, Dallas, Texas, Aug. 1992.

[9] M. Woods, Proceedings of the XXIX Rencontres de Moriond, Moriond, France, March 1994.

[10] S.D. Drell and T.-M. Yan, Phys. Rev. Lett **25**, 316 (1970).

[11] F. Abe *et al.*, CDF Collaboration, Phys. Rev. **D43**, 2070 (1991).

[12] J. Alitti *et al.*, UA2 Collaboration, Phys. Lett. **B276**, 354 (1992).

[13] A. Denner and T. Sack, Zeit. Phys. **C46**, 653 (1990).

[14] J. Rosner, M. Worah, and T. Takeuchi, Enrico Fermi Institute preprint EFI-93-40 (1993).

[15] A. Denner, Fortschr. Phys. **41**, 307 (1993).

[16] A. Sirlin, Phys. Rev. **D22**, 971 (1980); W. Hollik, Fortschr. Phys. **38**, 165 (1990).

[17] The limit $m_t > 91$ GeV/c^2 has been pulished in F. Abe *et al.* Phys. Rev. **D45**, 3921 (1992), and the more recent limit $m_t > 131$ GeV/c^2 will appear in S. Abachi *et al.*, submitted to Phys. Rev. Lett., Jan. 4, 1994.

[18] A direct search for the decay $t \rightarrow Hb$ has also been carried out by the CDF Collaboration (Fermilab Preprint 93/338-E, submitted to Phys. Rev. Lett.), but this search is dependent upon the parameter $tan\beta = v_1/v_2$, where v_1 and v_2 are the vacuum expectation values for the two charged Higgs fields of the model considered in this search.

[19] N. Cabbibo, III Topical Conference on Proton-Antiproton Collider Physics, Rome, Jan. 1983; F. Halzen and M. Marsula, Phys. Rev. Lett. **51**, 857 (1983); K. Hikasa, Phys. Rev. **D29**, 1939 (1984); N.G. Deshpande *et al*, Phys. Rev. Lett. **54**, 1757 (1985); A.D. Martin, R.G. Roberts, and W.J. Stirling, Phys. Lett. **189B**, 220 (1987); E.L. Berger, F. Halzen, C.S. Kim, and S. Willenbrock, Phys. Rev. **D40**, 83 (1989).

[20] L. Rolandi, Proceedings of the XXVI International Conference on High Energy Physics, Dallas, Texas, Aug. 1992.

[21] See V. Barger and R.J.N. Phillips, Collider Physics, (Addison Wesley, Redwood City, 1987), pp. 259 - 261.

[22] G. Arnison *et. al.*, Phys. Lett. **122B**, 103 (1983); Phys. Lett. **126B**, 398 (1983); Phys. Lett. **129B**, 273 (1983); Phys. Lett. **134B**, 469 (1983); M. Banner *et. al.*, Phys. Lett. **122B**, 476 (1983); P. Bagnaia *et. al.*, Phys. Lett. **129B**, 130 (1983).

[23] P. Jenni, in Proceedigs of the 1987 International Symposium on Lepton and Photon Interactions at High Energies, Hamberg, Germany, ed. by W. Bartel and R. Rückl (North Holland Physics Publishing Division, Amsterdam, 1988), p. 341.

[24] CDF Collaboration, F. Abe *et. al.*, Phys. Rev. Lett. **64**, 152 (1990).

[25] CDF Collaboration, F. Abe *et. al.*, Phys. Rev. Lett. **69**, 28 (1992).

[26] UA1 Collaboration, Phys. Lett. **253B**, 503 (1991).

[27] UA2 Collaboration, Phys. Lett. **276B**, 365 (1991).

[28] DØ Collaboration, paper submitted by K. Hara to IX Topical Conference on Proton-Antiproton Physics, Tsukuba, Oct., 1993.

[29] P. Roudeau *et. al.*, in the "EFCA Workshop on LEP200," CERN-87-08, edited by A. Böhm and W. Hoogland, p. 62.

[30] CDF Collaboration, F. Abe *et al*, Nucl. Instrum. Methods Phys. Res., Sect. A **271**, 387 (1988). See also W. Carithers *et. al.*, Nucl. Instrum. Methods Phys. Res., Sect. A **289**, 388 (1990) for a description of the high-precision inner tracking chamber, the Silicon Vertex Detector (SVX). The SVX was installed prior to the 1992-1993 run.

[31] At CDF, cylindrical coordinates r, ϕ, and z are used. The angle ϕ is the azimuthal coordinate and θ is the polar angle, or angle with respect to the proton beam direction. The pseudo-rapidity, η, is approximately equal to the rapidity, y, for relativisitic particles and is defined as $\eta \equiv \ln(\cot(\theta/2))$.

[32] For clusters with $E_T > 100$ *GeV*, the Had/EM cut is not placed.

[33] The χ^2_{wire} variable tends to be biased, however, against electrons which emit Bremsstrahlung radiation as they pass through the material within the tracking volume.

[34] CDF Collaboration, F. Abe *et al*, submitted to Phys. Rev. D.

[35] CDF Collaboration, F. Abe *et al*, Nucl. Instr. and Meth. **A269**, 51 (1988).

[36] G.W. Foster *et. al.*, Nucl. Instrum. Methods Phys. Res., Sect. A **269**, 93 (1988).

[37] The efficiency of this trigger for electrons from heavy quark decay is lower as a result of the hadronic activity near the electron that causes the electron to fail the (Had+EM)/EM < 1.125 cut.

[38] Minimum bias triggers require only a coincidence of hits in both the forward and backward BBC's to signal the presence of an inelastic event. No requirements of the calorimeters are made.

[39] We have used ISAJET and a detector simulation of these processes and normalized to the observed number of W and Z^0 candidates. F. Paige and S. D. Protopopescu, ISAJET Monte Carlo program, BNL Report No. BNL38034, 1986 (*unpublished*).

[40] D. Buskulic *et al.*, Phys. Lett. B **313**, 535 (1993), and D. Gerdes, CDF Internal Memo # 2023, "*b* Tagging with Jet Probability."

[41] This method was first used in F. Abe et. al., Phys. Rev. Lett. **64**, 152 (1990).

[42] CDF Collaboration, F. Abe *et. al.*, Phys. Rev. **D44**, 29 (1991).

[43] T. Kamon, for the CDF Collaboration, Blois Conference, Providence, R.I., June 1993.

[44] C. Campagnari, CDF Internal Memo # 1025, "A Fast W and Z^0 Monte Carlo," June, 1989.

[45] CDF Collaboration, F. Abe *et. al.*, Phys. Rev. Lett. **66**, 2951 (1991).

[46] A.D. Martin, R. G. Roberts, and W. J. Stirling, "Parton Distribution Functions Updated," Rutherford Appleton Lab Preprint, RAL-92-078.

[47] CDF Collaboration, F. Abe *et. al.*, Phys. Rev. **D67**, 2937 (1991).

[48] M. H. Reno, University of Iowa report UIOWA-94-01 (1994); H. Baer and M.H. Reno, Forida State report FSU-HEP-901030 (1990); P. Arnold and M.H. Reno, Nucl. Phys. **B319**, 37 (1989).

[49] P. Arnold and R. Kauffman, Nucl. Phys. **B349**, 381 (1991).

[50] F. Abe *et. al.*, Phys. Rev. **D43**, 2070 (1991).

[51] D. Saltzberg, University of Chicago thesis (unpublished), 1994.

[52] R. G. Wagner (unpublished), based on calculations by F. Berends *et al.*, Z. Phys. **C27**, 155 (1985) and F. Berends and R. Kleiss, Z. Phys. **C27**, 365 (1985).

[53] W.Giele, D.Glover, and D. Kosower, Fermilab Pub. 92/230-T.

[54] See, for example P. Arnold and M.H. Reno, Nucl. Phys. **B319**, 37 (1989); P. Arnold and R. Kauffman, Nucl. Phys. **B349**, 381 (1991); and H. Baer and M.H. Reno, Forida State report FSU-HEP-901030 (1990).

[55] A.D. Martin, W. J. Stirling, and R.G. Roberts, Phys. Lett. B **228**, 149 (1989) and W.J. Stirling, private communication. The central value comes from new calculations using the primed PDF's of MRS, and the error comes from the method described in their published article.

[56] R. Tanaka, "Precision Tests of the Electroweak Interaction," Proc. XXVI Int'l. Conf. on High Energy Physics (1992) Dallas, Texas.

[57] We use $\Gamma(W \to e\nu) = (G_F/\sqrt{2})(M_W^3/6\pi)$ for the partial width of W into electrons and $M_W = 80.24 \pm 0.11$ is taken from R. Tanaka, above, and

$sin^2\theta_W = 0.2325 \pm 0.0005$ is taken from M. Schwartz, Proceedings of XVI Lepton-Photon Conference, Ithaca, New York (1993).

[58] We use the method of M. Aguilar *et. al.*, (Particle Data Group), Phys. Lett. **B 204**, 1 (1988), for extracting a limit in the case of a bounded physical region.

[59] Note that, in the transverse plane, $P_T = \gamma M_W \beta$, where β is the W velocity in the transverse plane and $\gamma^{-1} = \sqrt{1 - \beta^2}$. Solving for β when M_W and P_T are known, one obtains $\beta^2 = (1 + \frac{M_W^2}{P_T^2})^{-1}$.

[60] Recall that in $p\overline{p}$ collisions there is a finite probability of obtaining more than one inelastic event within a single crossing of the p and $\overline{p}$ beams. This probability is Poisson distributed, and grows with instantaneous luminosity: the mean event rate is given by $R = \sigma_{Tot} \cdot \mathcal{L}$, where σ_{Tot} is the total $p\overline{p}$ cross section and $\mathcal{L}$ is the instantaneous luminosity. With $\sigma_{Tot} \approx 72$ mb and $\mathcal{L} \approx 5 \cdot 10^{30}$ cm^{-2}s^{-1}, the event rate is on the order of $R \approx 360$ kHz. Since the crossing time of the p and $\overline{p}$ bunches is $\tau = 3.5$ μsec, the mean number of events per crossing is $\langle N \rangle \approx R\tau = 1.3$. Given that the minimum bias cross section is of the order of mb, while the W and Z^0 cross sections are of the order of nb, the second event in a W or Z^0 event is most likely to be a minimum bias event.